sciendo

Theoretical modeling of optical spectra of N(1) and N(10) substituted lumichrome derivatives

Denisa Cagardová[1], Jan Truksa[2], Martin Michalík[1], Jan Richtár[2], Jozef Krajčovič[2], Martin Weiter[2], Vladimír Lukeš[1]

[1]*Institute of Physical Chemistry and Chemical Physics, Slovak University of Technology in Bratislava, Radlinského 9, SK-812 37 Bratislava, Slovakia*
[2]*Faculty of Chemistry, Brno University of Technology, Purkyňova 118, CZ-612 00 Brno, Czech Republic*
denisa.cagardova@stuba.sk

Abstract: A systematic study of (7,8-dimethylated) alloxazine, isoalloxazine, and their derivatives with substituted N(1) and N(10) positions was conducted using the density functional theory. The main aim of this work was the direct investigation of substituent effect on the molecular structure. Furthermore, HOMED aromaticity indices were calculated to describe the scope of the geometry changes. Frontier molecular orbitals of reference alloxazine, isoalloxazine and lumichrome derivatives were discussed by means of changes in their shape and energy levels. Photophysical properties were analyzed by determination of optical transition energies using the TD-DFT method. Obtained results were compared with previously published experimental data.

Keywords: Aromaticity index; vertical excited transitions; excited states; fluorescence; lumichrome; alloxazine

Introduction

Photochemical and photophysical properties of alloxazine and its derivatives have been studied since 1966 (Kozioł, 1966). Methyl-substituted alloxazines, mainly riboflavin and lumichrome are present in many foods and they play a key role in many enzymatic reactions and processes such as phototropism and phototaxis (Ai et al., 2010). Although the parent alloxazine and isoalloxazine are closely related compounds (see Fig. 1), the shift of a hydrogen atom from position N(1) to N(10) causes

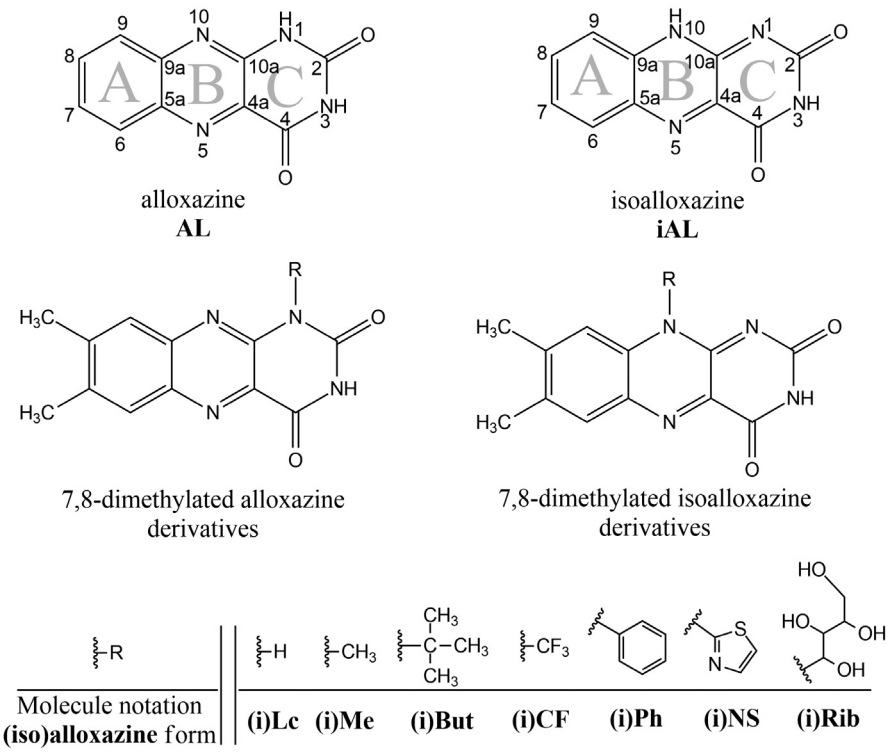

Fig. 1. Schematic structure of studied molecules: ring and atom notation of the benzo[g]pteridine moiety applied for all derivatives.

significant changes in their spectroscopic and photophysical properties.

Alloxazine exhibits absorption spectra differing from those of isoalloxazine by a hypsochromic shift of both long-wavelength maxima from about 440 nm and 340 nm to about 380 nm and 330 nm (Sikorska et al., 2004a). Moreover, isoalloxazine exhibits one order of magnitude larger fluorescence quantum yields and correspondingly longer fluorescence lifetimes than alloxazine. At pH = 10, the presence of isoalloxazine (9 %) is expected while at pH = 4, the solution does not contain the tautomeric isoalloxazine form (Penzkofer, 2016). The fluorescence wavelength maximum of an alloxazine sample in an aqueous solution at pH = 4 for fluorescence excitation wavelength λ_{exc} = 330 nm is 456 nm. At pH = 10, the emission wavelength of 530 nm is observed for the fluorescence excitation wavelength λ_{exc} = 440 nm. The first absorption bands of alloxazine and lumichrome show minimal environmental dependence. A significant effect of polarity and proticity of the solvent was observed for their second absorption band (Salzmann and Marian, 2009). Surprising differences between these two molecules were found in the absorption strength, fluorescence lifetime, fluorescence quantum yield, and thermal ground-state tautomeric content at pH = 10. The absorption spectrum of riboflavin and iso-(6,7)-riboflavin in methanol shows two characteristic bands at longer wavelengths, with the maxima at approximately 360 nm and 444 nm for riboflavin; and at 343 nm and 447 nm for iso-(6,7)-riboflavin, which indicates the effect of the methyl group position on the shorter-wavelength maximum. The effect of methyl group on the positions of absorption maxima was examined by Sikorska et al. using both experiment and theory with a broad range of (iso)alloxazine derivatives (Sikorska et al., 2004b; Sikorska et al., 2004c).

Available information about the chemical and electronic structure of (iso)7,8-dimethyl-alloxazine substituted in position N(1) or N(10) is incomplete. Previous experimental and theoretical studies of these compounds were focused on two substituents — methyl and 2,3,4,5-tetrahydroxypentyl groups (Gross et al., 1996; Sikorska et al., 2005; Zanetti-Polzi et al., 2017). Therefore, theoretical analysis of 14 derivatives based on the modification of the initial benzo[g]pteridine moiety in (iso) alloxazine by 7,8-dimethylation and substitution in N(1) or N(10) positions (Fig. 1) is presented here. In laboratory practice, the selected functional groups can be synthetically added to the benzo[g]pteridine moiety into selected positions. Partial aims of this study are: (1) to calculate optimal geometries of the electroneutral molecules and selected lowest energy excited electronic states; (2) to evaluate the energies of frontier molecular orbitals (MOs) and (3) to calculate optical transitions contributing to the lowest energy in absorption and fluorescence spectra.

Computational details

The Gaussian 09 program package (Frisch et al., 2013) was applied for all quantum chemical calculations by means of the density functional theory. In these calculations, the B3LYP hybrid functional (Lee et al., 1988; Becke, 1988) without any constraints (energy cut-off of 10^{-5} kJ · mol^{-1}, final RMS energy gradient under 0.01 kJ · mol^{-1} · A^{-1}) was used. A sufficiently large basis set of atomic orbitals 6-311++G** was applied (Hariharan and Pople, 1973; Rassolov et al., 1998). In search of optimized B3LYP geometries, the time dependent TD-DFT method was used. As a result, vertical singlet and triplet transition energies and the corresponding oscillator strengths between the initial and final electronic states were determined (Furche and Ahlrichs, 2002). The molecules and their frontier molecular orbitals were visualized using the Molekel (Flukiger et al., 2002) and Avogadro (Hanwell et al., 2012) program packages.

Aromaticity of molecules gives significant information about their chemical structure. One way to describe aromaticity is the structure-based Harmonic Oscillator Model of Electron Delocalization (HOMED) index (Cyrański et al., 2002; Frizzo and Martins, 2012), which describes the bond length changes in molecules of interest with respect to the reference aromatic molecules. The index can be calculated by the equation:

$$\mathrm{HOMED} = 1 - \frac{1}{m}\left\{\alpha_{XY}\sum_{i=1}^{m}\left(R(XY)_{ref} - R(XY)_i\right)^2\right\} \qquad (1)$$

where m stands for the number of bonds considered in the investigated aromatic ring, $R(XY)_{ref}$ is the reference bond length, α_{XY} is a normalization constant (see below) and $R(XY)_i$ is the actual bond length between X and Y atoms.

In case of the studied derivatives, C—C, C—N and C—N(H) aromatic bond lengths were determined. Suitable reference quantities, R_{ref}, used in Eq(1) were obtained from the B3LYP/6-311++G** optimized structures of benzene, 1,3,5-triazine and pyrrole molecules for CC, CN and CN(H) bonds, respectively. The proposed R_{ref} values for the basis set are: 1.3943 Å ($R(CC)_{ref}$), 1.3344 Å ($R(CN)_{ref}$) and 1.3749 Å ($R(CN(H))_{ref}$). Normalization constants α_{XY} were calculated as follows (Ośmiałowski et al., 2006):

$$\alpha(XY) = \qquad (2)$$
$$= 2\left\{\left(R(XY)_{ref} - R(XY)_{sin}\right)^2 + \left(R(XY)_{ref} - R(XY)_{doub}\right)^2\right\}^{-1}$$

where the reference single R_{sin} and double R_{doub} bond lengths were taken from the optimized structures of ethane and ethene (CC bonds), N—$(CH_3)_3$ and H_2C=N—CH_3 (CN bonds), $(H_3C)_2$—NH and H_2C=NH (CN(H) bonds) molecules, respectively (Allen et al., 1987). The calculated B3LYP R_{sin} bond lengths are: 1.5317 Å (C—C), 1.4554 Å (C—N) and 1.4574 Å for the C—N(H) bond. Moreover, the double bond lengths R_{doub} of 1.3289 Å (C=C), 1.2631 Å (C=N) and 1.2672 Å (C=N(H)) were used to determine α_{XY} from Eq(2). The corresponding normalization constants are: α(CC) = 86.40 Å^{-2}, α(CN) = 101.41 Å^{-2} and α(CN(H)) = 108.66 Å^{-2}. The maximal HOMED value of one was assigned to the benzene molecule by convention.

Results and Discussion

Although isobutyl, methyl, trifluoromethyl, thiazole, and 2,3,4,5-tetrahydroxypenthyl substituents show many conformations, chemical structure of the benzo[g]pteridine core is not affected significantly. As seen in Tab. 1, HOMED(A) indices of the isoalloxazine form are consistently by ca. 0.04 higher than those of the alloxazine counterparts. Moreover, dimethylation in C(7) and C(8) positions causes a decrease in the A ring aromaticity (see **Lc/iLc**), while additional substitutions slightly increase the HOMED(A).

With respect to the parent **AL** and **iAL** molecules, the HOMED(C) index is much lower for the isoalloxazine derivatives than for the alloxazine forms, with exception of **(i)NS**, **(i)CF** and **(i)But** tautomer couples. This effect is the most significant for **CF** and **But**, possibly because CF_3 is a strongly electron-withdrawing group and tert-butyl group is relatively bulky and electron-donating group with much higher positive inductive effect than the methyl group in **Me**. They cause the most significant decrease in the aromaticity possibly because of the distortion due to steric repulsion and strong inductive effect. **NS** contains larger atoms than carbon, so some steric distortion is expected, but it is smaller due to the two-dimensional nature of the ring. Moreover, in case of substituted rings, the comparison is complicated by the fact that the substituents in tautomers are present on different rings. Therefore, it makes more sense to compare the substitution effect of the C ring in the alloxazine form to the B ring in isoalloxazine form and vice versa (see Fig. 1). Two methyl groups attached to the A ring in **Lc** and **iLc** cause an increase of HOMED for both B and C rings. Additional substitution to the B (C) ring of **iLc** (**Lc**) significantly decreases the aromaticity of the substituted ring. Relative changes correspond to the differences between HOMED of the studied molecule and the reference alloxazine/isoalloxazine molecule divided by the HOMED of reference. Relevant changes of HOMED indices in comparison to alloxazine and isoalloxazine molecules are shown in Fig. 2. Note that all studied derivatives, apart from two methyl groups at C(7) and C(8) atoms such as lumichrome **Lc,** have also another additional substituent. Thus, the B and/or C ring substitution effect is cumulative with respect to the two methyl groups. These side methyl groups bonded to the A ring increase the aromaticity by up to 2 % for both (un)substituted rings in tautomers.

In case of the HOMED index of substituted rings, i.e. C ring of alloxazine derivative and B ring of iso-form, all studied additional substituents decrease their aromaticity (see Tab. 1 and Fig. 2a). The bond length changes caused by the presence of a double bond in the C ring of the iso-form also affect HOMED(C), which is more likely to be visible in molecules with smaller or linear substituents. A similar case may be argued for the HOMED(B) index of isoalloxazine derivatives where the ring lacks a double bond and is influenced by the substituent which leads to a significant distortion of geometry. The largest decrease of around 30 % has been found for the **CF/iCF** derivatives while butyl group brings the HOMED indices down by 18 %. It occurs mainly by exceptional ring distortion due to CF_3 because of the above-mentioned strong electron-withdrawing

Tab. 1. HOMED indices of A, B and C rings of studied molecules.

Molecule	A	B	C	Molecule	A	B	C
AL	0.942	0.924	0.814	**iAL**	0.983	0.867	0.664
Lc	0.930	0.934	0.821	**iLc**	0.975	0.880	0.678
Me	0.934	0.933	0.724	**iMe**	0.975	0.798	0.690
But	0.938	0.928	0.668	**iBut**	0.975	0.735	0.680
CF	0.932	0.938	0.585	**iCF**	0.982	0.668	0.645
Ph	0.933	0.934	0.696	**iPh**	0.975	0.784	0.683
NS	0.932	0.935	0.671	**iNS**	0.977	0.763	0.677
Rib	0.936	0.933	0.723	**iRib**	0.974	0.794	0.695

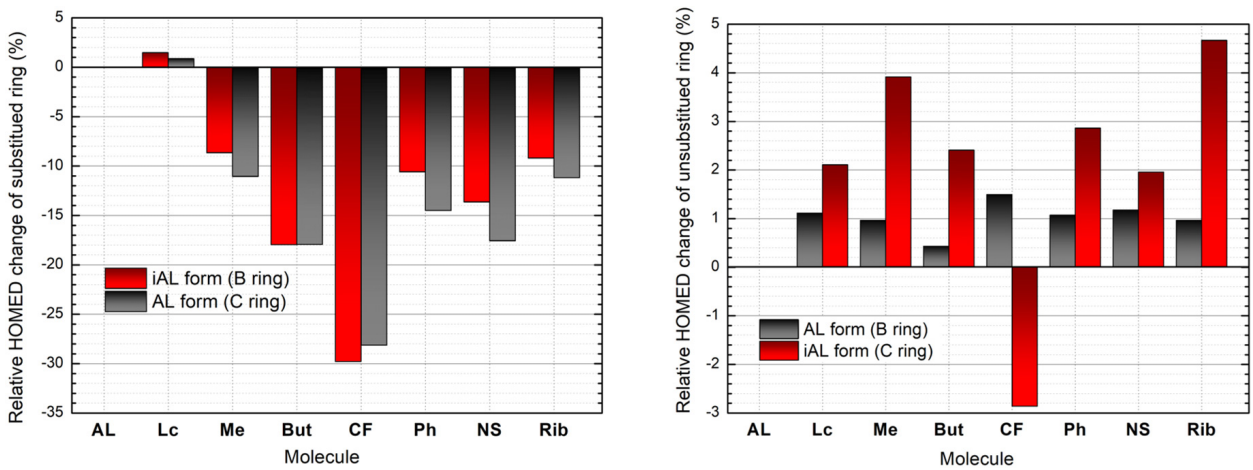

Fig. 2. Relative changes of HOMED indices of a) substituted C/B ring and b) unsubstituted B/C ring of alloxazine/isoalloxazine derivatives.

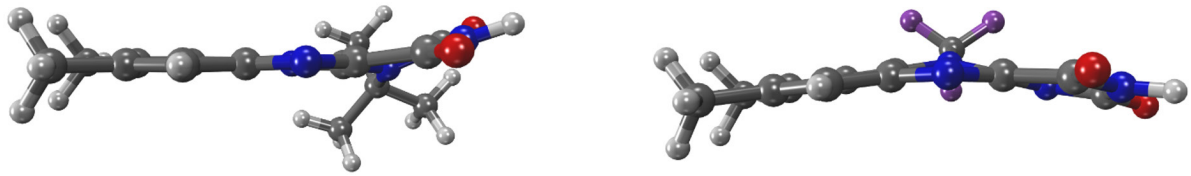

But iCF

Fig. 3. Distortion of rings observable in optimal geometry of **But** and **iCF**.

effect of the group and bulky tert-butyl substituent (e.g. see **But** and **iCF** ring distortion in Fig. 3).

Based on Fig. 2a, the smallest changes of aromaticity in the substituted rings in comparison to their parent (iso)alloxazine molecules are caused by the methyl group in **(i)Me**. Large 2,3,4,5-tetrahydroxypentyl substituent in **(i)Rib** had minimal influence on the HOMED indices. These comparatively small relative changes in HOMED indicate less significant substituent influence (up to 12 %) than the remaining additional substituents, which supports the above-mentioned steric effect hypothesis and small inductive effect.

In heterocyclic rings without a substituent (see Fig. 2b), i.e. B ring of alloxazine and C ring of isoalloxazine, small substituent-induced HOMED increase of up to 5 %, with exception for **iCF,** can be seen. Interestingly, isoalloxazine forms are much more affected; however, it is still considered to be negligible in comparison to HOMED changes of substituted ring. Based on these results, the **iCF** derivative is the least stable within the studied group as the trifluoromethyl group consistently decreases the aromaticity, as evaluated by HOMED indices.

Energy levels of frontier molecular orbitals and their shape allow estimating the electronic structure. Fig. 4 shows energy levels of the highest occupied (HOMOs) and lowest unoccupied (LUMOs) molecular orbitals. The B3LYP HOMO and LUMO energies for alloxazine **AL**/isoalloxazine **iAL** are: –7.18 eV/–7.04 eV and –3.17 eV/–3.53 eV, respectively. In case of two methyl groups addition to C(7) and C(8) in **Lc/iLc**, a slight increase of both HOMO (–6.91 eV/–6.76 eV) and LUMO (–2.97 eV/–3.34 eV) energies can be seen, so the constriction of energy gap occurs. The substitution group variation alters the orbital energies in different ways.

Methyl (**Me/iMe**), butyl (**But/iBut**), phenyl (**Ph/iPh**), and 2,3,4,5-tetrahydroxypentyl (**Rib/iRib**) functional groups have comparable influence on the energies of frontier MOs. Differences are found only between the alloxazine and isoalloxazine forms. Isoalloxazine forms generally have smaller HOMO to LUMO energy difference. Minimal LUMO energy of –3.66 eV was found for the **iCF** derivative. The highest B3LYP HOMO energy is predicted for **iRib** (–6.33 eV) while the **CF** molecule exhibited the lowest one of –7.23 eV.

As it is depicted in Fig. 5, frontier MOs are delocalized over the whole molecule in all cases indicating an effective π-conjugation in the central fused systems. HOMO and LUMO orbitals of the studied molecules have a π-electron character, but the electron clouds are not as uniformly delocalized as in the parent alloxazine and isoalloxa-

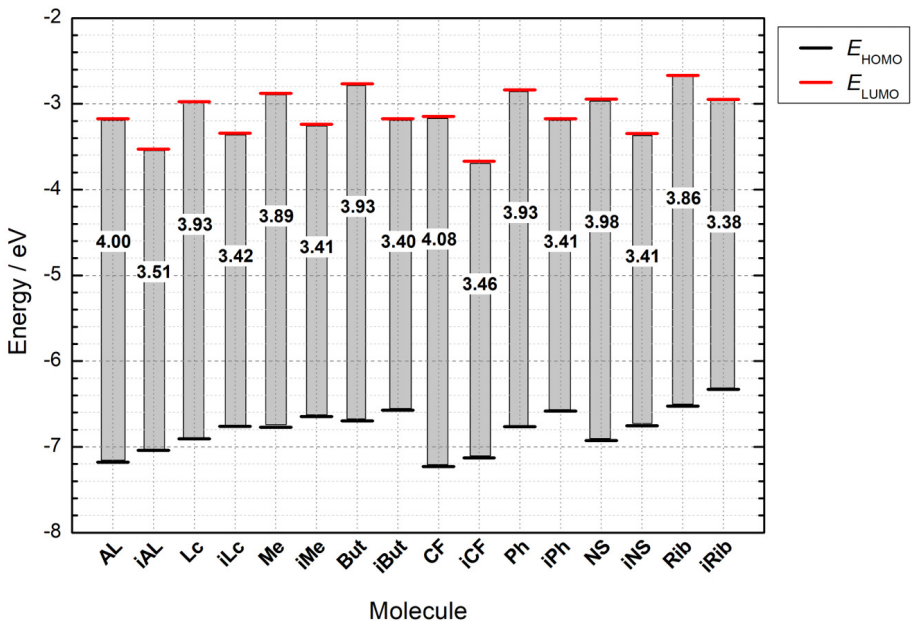

Fig. 4. Energy diagram of B3LYP frontier molecular orbitals for the neutral state of studied molecules. Energy differences between the frontier molecular orbital levels are depicted by grey rectangles and the value corresponds to the energy gap in eV.

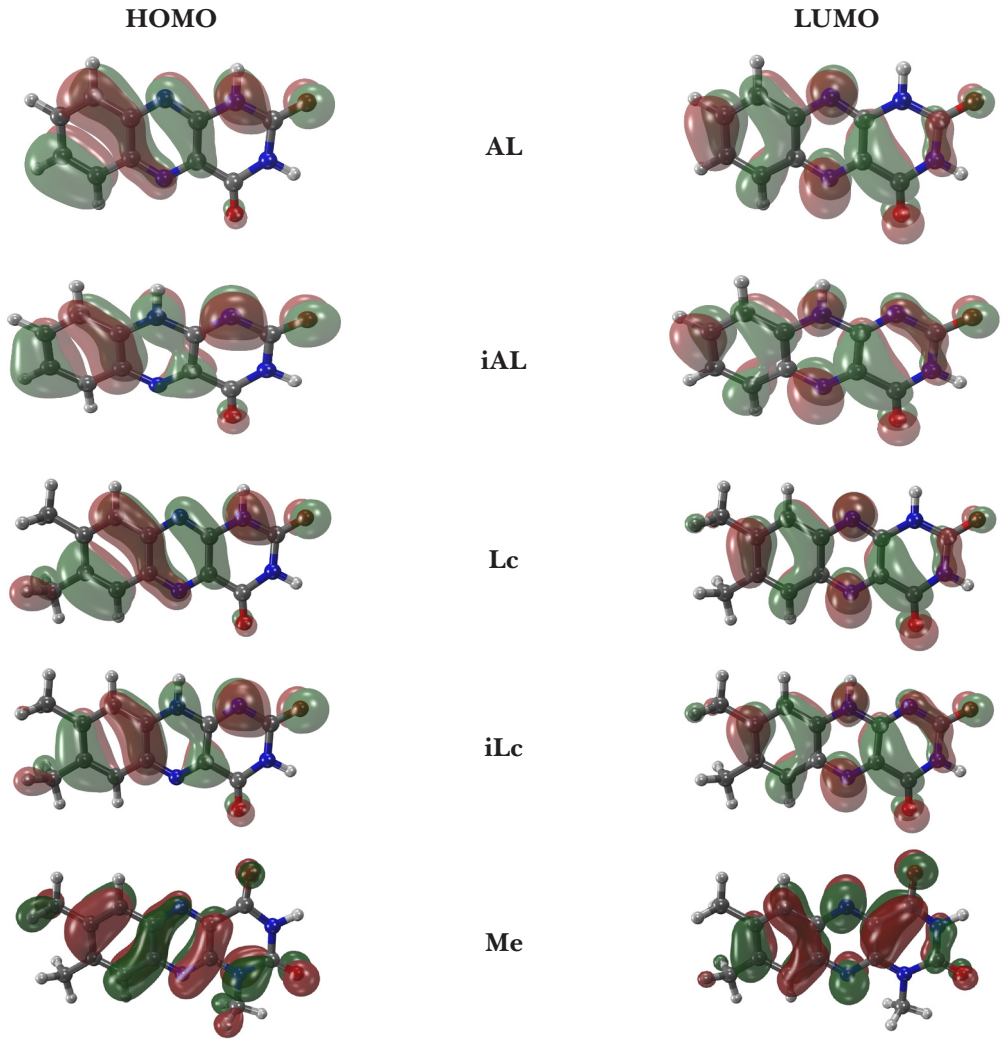

Fig. 5. Shapes of frontier molecular orbitals of studied molecules. Iso-surface value is 0.025.

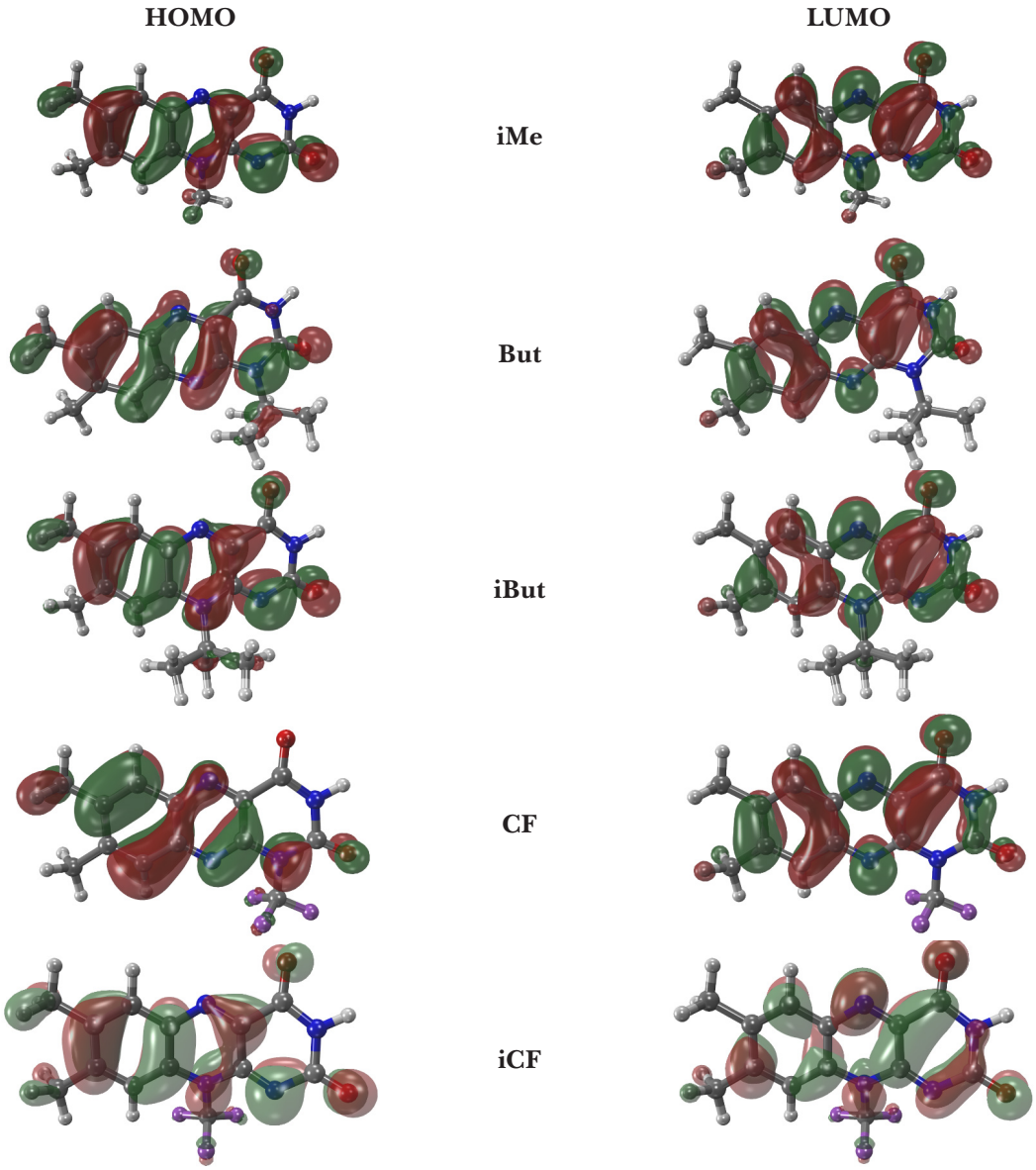

Fig. 5. (continued) Shapes of frontier molecular orbitals of studied molecules. Iso-surface value is 0.025.

zine molecules. Shapes of the orbitals are modulated by the bonding of methyl groups in C(7) and C(8) positions and by the additional studied substitution. Nevertheless, for all studied molecules, the lobes of HOMOs are absent over the C(2) atom and they are present over the methyl group in the vicinity of the C(7) atom. Interestingly, very small electronic clouds were found over the fluorine atoms in **(i)CF** and hydrogen atoms in additional methyl group in **(i)Me** derivatives. The electron withdrawing CF_3 group also causes an electron cloud formation over the hydrogens of the CH_3-C(7) group and another cloud above CH_3-C(8) occurs in its iso-tautomer. In case of LUMO lobes, distribution of isoalloxazine derivatives, clouds are mostly delocalized over the whole benzo[g]pteridine moiety. On the other hand, molecules in the alloxazine form show lower delocalization over the N(1) nitrogen which is attached to the substituted functional group.

Parent (iso)alloxazine molecules and their alkyl substituted derivatives exhibit experimental absorption spectra with several major bands in the ultraviolet-visible region. For example, the first experimental band maxima of **AL** (Sikorska et al., 2004a) and **Lc** (Sikorski et al., 1998) in aqueous solution are found at 3.27 eV (379 nm) and 3.22 eV (385 nm), respectively. The second absorption band is located at 3.87 eV (320 nm) for alloxazine and at 3.71 eV (334 nm) for lumichrome (**Lc**). Comparison of the lowest vertical gas-phase TD-B3LYP energies for the singlet states is provided in Fig. 6. For alloxazine, energy of the first excited vertical singlet state (S_1) over the electronic ground state is 3.38 eV (367 nm). The corresponding oscillator strength is negligible. This forbidden excitation comes from

an n-type molecular orbital to π*-type HOMO–2 to LUMO transition. The second excited singlet state, related to the HOMO to LUMO transition, is merely 0.06 eV above the S_1 state with $^1(\pi\pi^*)$ character. According to the previously published results, the third excited singlet state (S_3) has $^1(n\pi^*)$ character. The vertical excitation energy of this $S_0 \rightarrow S_3$ transition is 3.93 eV (315 nm) and the oscillator strength is negligible. The fourth vertical optical transition has a significant oscillator strength of 0.16 and the corresponding excitation energy is 3.97 eV (313 nm). For lumichrome **Lc**, first absorption band occurs at 3.39 eV (366 nm), which is insignificantly shifted compared to alloxazine **AL**, thus the two methyl groups bonded to the A ring have negligible effect on the absorption band maxima. Interestingly, oscillator strength increases to 0.06 and this first absorption band matches the HOMO→LUMO transition. The same situation can be observed in iso-tautomers **iAL** and **iLc**. $S_0 \rightarrow S_1$ energies of 3.09 eV (400 nm) with $^1(n\pi^*)$ character for **iAL** and 3.02 eV (411 nm) with $^1(\pi\pi^*)$ character for **iLc** show that dimethylation to C(7) and C(8) slightly decreases the transition energy. However, HOMO→LUMO transition occurs in **Lc** with the corresponding oscillator strength of 0.20, while in **iAL,** HOMO–1 to LUMO transition occurs with negligible oscillator strength. The second excitation of **iAL** (transition from HOMO to LUMO) exhibits the $^1(\pi\pi^*)$ character with oscillator strength of 0.17. Changes in electron distribution and aromaticity of the iso-form within tautomer couples lead to the bathochromic shifts of the lowest energy transitions compared to the alloxazine forms. In case of additional substitution of methyl to the B or C ring for (**i**)**Me**, the calculated TD-B3LYP excitation energies are red shifted in comparison to (**i**)**Lc**, i.e. 3.37 eV (368 nm), 3.40 eV (364 nm) for the first two excitation energies for **Me**. Slightly higher vertical excitation energies (3.41 eV, 3.47 eV, 3.86 eV, 4.02 eV for **AL** and 3.44 eV, 3.41 eV, 3.89 eV, 3.91 eV for **Me**) were obtained using a combination of the density functional and multi-reference configuration interaction method (DFT/MRCI) (Grimme and Waletzke, 1999).

TD-B3LYP predicts zero oscillator strengths for vertical triplet excitations. For **AL**, **Lc** and their substituted derivatives, the lowest energy triplet excitation $S_0 \rightarrow T_1$ ranges between 2.50 eV and 2.65 eV while the iso-forms of tautomer couples show the energy slightly above 2 eV. According to the previously published works (Sikorska et al., 2004d), the $S_0 \rightarrow T_1$ transition has $^3(\pi\pi^*)$ character.

Experimental fluorescence emission spectra of the studied molecules show a single band where the exact position of the maximum depends on the environment and tautomeric forms. For example, maxima of the fluorescence emission measured in acetonitrile are 2.79 eV (444 nm) for alloxazine (**AL**) and 2.84 eV (436 nm) for lumichrome (**Lc**). The fluorescence emission spectrum of lumiflavin (**iMe**) and riboflavin (**iRib**) in methanol (Sikorska et al., 2005) show a band with the maxima at 2.37 eV (526 nm) and 2.33 eV (532 nm), respectively. Isoalloxazine exhibits one order of magnitude higher fluorescence quantum yields and cor-

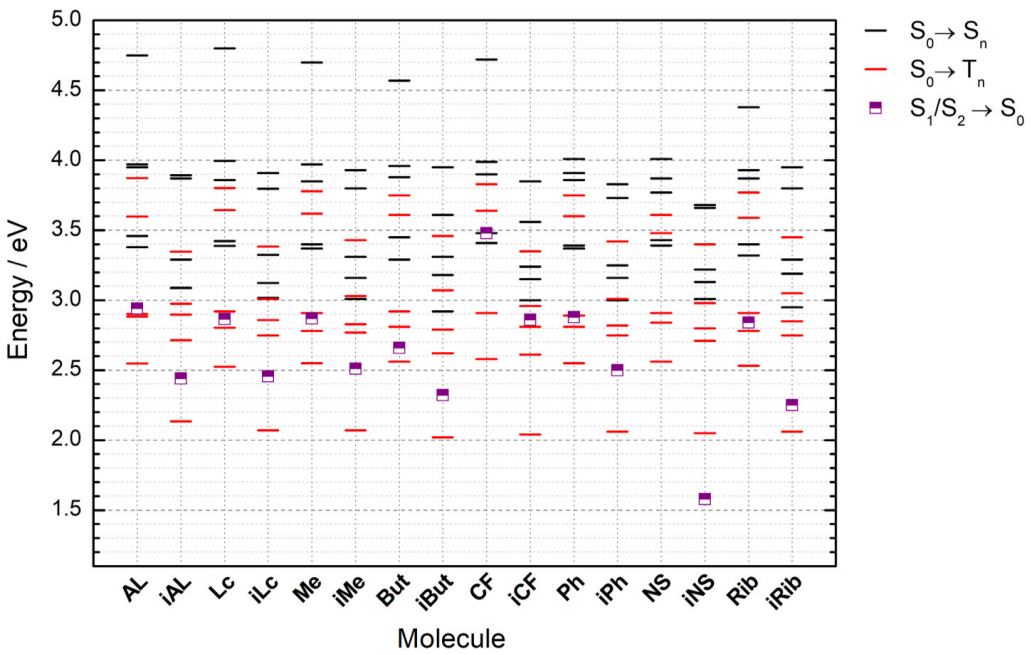

Fig. 6. Energy diagram of selected lowest energy vertical TD-B3LYP singlet ($S_0 \rightarrow S_n$) and triplet ($S_0 \rightarrow T_n$) excitation energies for optimal electronic-ground state geometries and $S_1/S_2 \rightarrow S_0$ deexcitation energies.

respondingly longer fluorescence lifetimes than alloxazine. At the level of time dependent DFT, many optimal geometries of the excited singlet and triplet states of alloxazine derivatives represent a saddle point. As it was reported by Salzmann et al. (2009), one imaginary frequency is obtained for out-of-plane deformation. Nevertheless, TD-DFT deexcitation energies agree with the DFT/MRCI results for the alloxazine and isoalloxazine derivatives.

As it was proved by Sikorska et. al. (2005) for riboflavin (**iRib**), the $^1(\pi\pi^*)$ to $^3(\pi\pi^*)$ intersystem crossing increases the quantum yield of triplet oxygen formation and decreases the quantum yields of singlet oxygen formation with a suitable energy levels difference to influence the $^1O_2$ to $^3O_2$ conversion (Min and Boff, 2006). Since riboflavin (**iRib**) is already in use as a photo-antimicrobial agent with the excitation wavelength of 450 nm (Min and Boff, 2006), a derivative with similar singlet and triplet energy levels has possible future application in medicine. Our theoretical calculations show that the singlet to triplet energy difference of the HOMO→LUMO transition is clearly modulated by tautomerization.

Conclusions

Optimal geometries and electronic structure of (iso)alloxazine, lumichrome, and its model substituted tautomeric derivatives were investigated using the density functional theory. Changes in molecular geometry and local aromaticity of the benzo[g]pteridine core were described using the local HOMED aromaticity indices. The only substituent, which consistently decreases the aromaticity of all rings was —CF_3 bonded to the N(10) atom possibly because of very inductive electron-withdrawing character of the group. The **iCF** derivative is thus the least stable within the studied group. Generally, the smallest changes of the HOMED index were found in the benzene-like A ring mostly due to dimethyl substitution on this ring (0.01). HOMED changes of the heterocyclic B and C rings were larger by one to two tenths depending on the position of the substituent. The substitution using methyl, butyl, phenyl, and 2,3,4,5-tetrahydroxypentyl had minimal effect on the energies of frontier molecular orbitals. Due to the heterocyclic ring substitution, the HOMO–LUMO band gaps were lowered for all cases except for **CF**. TD-B3LYP calculations of optical transitions predicted that the large number of studied derivatives can absorb and emit light in the visible spectral region. Obtained theoretical results can be helpful in the preparation of materials applicable in optoelectronics or medicine in the future.

Acknowledgement

The work has been supported by the Slovak Research and Development Agency (APVV-15-0053) and VEGA 1/0504/20. We are grateful to the HPC center at the Slovak University of Technology in Bratislava, which is a part of the Slovak Infrastructure of High Performance Computing (SIVVP project, ITMS code 26230120002, funded by the European region development funds, ERDF) for the computational time and resources made available.

D.C. would like to thank for the financial support from the STU Grant scheme for Support of Young Researchers (1848).

J.T. thanks the internal grant FCH-S-20-6340 of the Brno University of Technology.

References

Ai Y, Zhang F, Chen S, Luo Y, Fang W (2010) J. Phys. Chem. Lett. 1: 743—747.

Allen FH, Kennard O, Watson DG, Brammer L, Orpen AG, Taylor R (1987) J. Chem. Soc. Perkin Trans. 2.: S1—S19.

Becke AD (1988) Phys. Rev. A 38: 3098—3100.

Cyrański MK, Krygowski TM, Katritzky AR, Schleyer PvR (2002) J. Org. Chem. 67: 1333—1338.

Flukiger P, Luthi HP, Sortmann S, Weber J (2002) Molekel 4.3, Swiss National Supercomputing Centre, Manno, Switzerland.

Frisch MJ, Trucks GW, Schlegel HB, Scuseria GE, Robb MA, Cheeseman JR, Scalmani G, Barone V, Menucci B, Petersson GA, Nakatsuji H, Caricato M, Li X, Hratchian HP, Izmaylov AF, Bloino J, Zheng G, Sonnenberg JL, Hada M, Ehara M, Toyota K, Fukuda R, Hasegawa J, Ishida M, Nakajima T, Honda Y, Kitao O, Nakai H, Vreven T, Montgomerry JA Jr., Peralta JE, Ogliaro F, Bearpark MJ, Heyd JJ, Brothers EN, Kudin KN, Staroverov VN, Keith TA, Kobayashi R, Normand J, Raghavachari K, Rendell AP, Burant JC, Iyengar SS, Tomasi J, Cossi M, Rega N, Millam JM, Klene M, Knox JE, Cross JB, Bakken V, Adamo C, Jaramillo J, Gomperts R, Stratmann RE, Yazyev O, Austin AJ, Cammi R, Pomelli C, Ochterski JW, Martin RL, Morokuma K, Zakrzewski VG, Voth GA, Salvador P, Dannenberg JJ, Dapprich S, Daniels AD, Farkas O, Foresman JB, Ortiz JV, Cioslowski J, Fox DJ (2013) Gaussian 09, Revision D.01, Gaussian, Inc., Wallingford CT.

Frizzo CP, Martins MAP (2012) Struct Chem 23: 375—380.

Furche F, Ahlrichs R (2002) J. Chem. Phys. 117: 7433.

Grimme S, Waletzke M (1999) J. Chem. Phys. 111(13): 5645—5655.

Gross E, Dobson J, Petersilka M (1996) Top. Curr. Chem. 181: 81.

Hanwell MD, Curtis DE, Lonie DC, Vandermeersch T, Zurek E, Hutchison GR (2012) J. Cheminformatics 4: 17.

Hariharan PC, Pople JA (1973) Theor. Chim. Acta 28: 213—222.

Kozioł J (1966) Photochem. Photobiol. 5: 41.

Lee C, Yang W, Parr RG (1988) Phys. Rev. B 37: 785—789.

Min DB, Boff JM (2006) Comp Rev Food Sci Food Saf. 1(2): 58–72.
Ośmiałowski B, Raczyńska ED, Krygowski TM (2006) J Org Chem 71(10): 3727–3736.
Penzkofer A (2016) J. Photochem. Photobiol. A 314: 114–124.
Rassolov V, Pople JA, Ratner M, Windus TL (1998) J. Chem. Phys. 109: 1223–1229.
Salzmann S, Marian CM (2009) Photochem. Photobiol. Sci. 8: 1655–1666.
Sikorska E, Khmelinskii IV, Bourdelande JL, Bednarek A, Williams SL, Patel M, Worrall DR, Koput J, Sikorski M (2004d) Chem Phys. 301(1): 95–103.
Sikorska E, Khmelinskii IV, Komasa A, Koput J, Ferreira LFV, Herance JR, Bourdelande JL, Williams SL, Worrall DR, Insińska-Rakc M, Sikorski M (2005) Chemical Physics 314: 239–247.
Sikorska E, Khmelinskii IV, Koput J, Sikorski M (2004c) J. Mol. Struct. (Theochem) 676: 155.
Sikorska E, Khmelinskii IV, Prukala W, Williams SL, Patel M, Worrall DR, Bourdelande JL, Koput J, Sikorski M (2004b) J. Phys. Chem. A 108: 1501.
Sikorska E, Khmelinskii IV, Worrall DR, Koput J, Sikorski M (2004a) J Fluoresc. 14(1): 57–64.
Sikorski M, Sikorska E, Worrall DR, Wilkinson D (1998) J. Chem. Soc. 94, 2347–2353.
Zanetti-Polzi L, Aschi M, Daidone I, Amadei A (2017) Chem. Phys. Lett. 669: 119–124.

sciendo

Toluene oxidation: UV irradiation vs. ferrates

Lucia Fašková, Daniela Pavúková, Emília Mališová, Ladislav Štibrányi, Ján Híveš

Department of Inorganic Technology, Institute of Inorganic Chemistry, Technology and Materials, Faculty of Chemical and Food Technology, Slovak University of Technology, Radlinského 9, 812 37 Bratislava, Slovakia
lucia.faskova@stuba.sk

Abstract: Novel technologies for organic pollutants degradation have been studied to cope with extensive water pollution. In this work, the use of ultraviolet degradation and potassium ferrate as possible oxidation tools for toluene, a widely used industrial chemical, degradation is proposed. In the experiment with ultraviolet irradiation, a low-pressure mercury lamp was used to generate a single line electromagnetic radiation with the wavelength of 254 nm. Maximal degradation efficiency achieved after 55 minutes of irradiation was 67.1 %. In the experiments with potassium ferrate, the highest degradation efficiency was 71.2 % at the concentration of 10 mg/L of ferrate (VI) anion.

Keywords: degradation, ferrate, toluene, UV irradiation

Introduction

Environmental pollution by organic chemicals represents one of the major concerns of today. Continuous manufacturing of petrochemicals and ongoing increase in mobility result in increased concentrations of substances such as benzene, toluene, chlorobenzene, polyaromatic hydrocarbons and many others in groundwater (Qiu et al., 2016). For instance, the amount of water needed to process crude oil is estimated to be 0.4 to 1.6-fold per unit of crude oil. Considering the amount of crude oil processed worldwide, 5.34 to 21.37 million cubic metres of wastewater are daily generated from the oil industry (Singh and Singh, 2019). Refineries are equipped with wastewater treatment plants, but their efficiency is not absolute and significant amounts of pollutants reach the water systems. In France, daily estimated release of toluene from one particular petrochemical industry site reached up to almost 26 kg in absolute terms. Nonetheless, petrochemical industry is not the sole source of toluene pollution. The occurrence of toluene can also originate from metalworking, paint manufacture and use, plastics and fibres industry, tanning, textile dying, papermills, surface treatment or traffic (European Chemicals Bureau, 2003). Another anthropological source of environmental pollution is through leakages in product pipelines (van der Meijde et al., 2009) or at gas stations (dos Anjos Santos et al., 2013). Toluene is a volatile compound and thus it is found in underground water near industrial sites and rarely in drinking water (Leutsch and Berkow, 2010). However, even evaporated toluene, or other volatile organic compounds, can reenter water sources via raindrops or snowflakes (Lei and Wania, 2004). Possible sources of toluene also imply natural sources, e.g. incomplete combustion during forest burning (Barboni et al., 2009), petroleum seepage or weathering of exposed coal from petroliferous rocks (Barberes et al., 2018). There is no doubt that toluene has an acute and chronic ecotoxicological impact on model organisms in magnitudes of milligrams per litre. However, there is also evidence of sublethal effects on animals, for example on the enzyme activity of fish affecting their metabolism (Dange and Masurekar, 1981), a change in fish haematological parameters (Inyang et al., 2018) or even oxidative stress and DNA damage in earthworms (Liu et al., 2010). Water pollutants are never present as single compounds but as complex mixtures and there is evidence of the synergistic effect of mixtures (Faust et al., 2003) and more authors observed also the additive effect (Li et al., 2013; Singh et al., 2010; Sato and Takajima, 1979). However, these compounds should not be present in water or the environment, which is also asserted by the European Union within Directive 2008/105/EC.

The scientific community is considerably engaged with this topic while searching for efficient means for the degradation of these dangerous substances. Various methods of organic substances degradation, including mainly incorporation of hydroxyl radical, e.g. ozonation (Kuo and Chen, 1996; Sekiguchi et al., 2003), electrooxidation (Farinos et al., 2017; Rabaaoui et al., 2013), catalysed photooxidation (Xu et al., 2020; Kim et al., 2019) or Fenton reactions (Huling et al., 2011; Ramteke and Gogate, 2015), have been investigated. In the presented

work, degradation of toluene using ultraviolet (UV) irradiation and potassium ferrate (K_2FeO_4), which is considered to be an environmentally friendly oxidant, is presented.

Materials and Methods

Used chemicals included toluene p.a. (Centralchem s.r.o, Slovakia), potassium ferrate (70 %, prepared internally according to the procedure published by Kubiňáková et al., 2015) and distilled water (prepared internally by atmospheric distillation).
Instrumental system for the degradation using UV irradiation comprised a reactor equipped with a low-pressure mercury lamp, which provided single line spectra with the wavelength of 254 nm at the power of 10 W.
As suitable analytical methods, high-performance liquid chromatography (HPLC) and gas chromatography coupled with mass spectrometry (GC-MS) were chosen. Prior to the GC-MS analysis, the samples were subjected to solid phase extraction (SPE).
Operating conditions of HPLC: HPLC Thermo Fisher UltiMate 3000 Rapid Separation with UltiMate DAD detector working at 254 nm; column: SUPELCOSIL™ LC-18 with dimensions of 25 cm × 4.6 mm × 5 µm; mobile phase: methanol:water ratio of 85:15 in isocratic mode; mobile phase flow: 1 mL/min.
Operating conditions of GC-MS: GC Agilent Technologies 7890A equipped with mass spectrometer Agilent Technologies 5975C, column: ZB-FAME with dimensions of 30 m × 0.25 mm × 0.20 µm; carrier gas: helium; carrier gas flow: 1.6 mL/min; temperature program: initial temperature of 80 °C held for one minute followed by a gradient of 10 °C/min up to 280 °C held for 10 minutes; injector temperature: 280 °C; electron ionization: at 70 eV.

UV irradiation experiments

Stock solutions of toluene in the amount of 250 mL and the concentration of 0.1, 0.3 and 0.5 mL/L were prepared, quantitatively transferred into the reactor and irradiated at the wavelength of 254 nm for 55 min. Temperature was kept at the value of 20 °C using cooling water, and the system was stirred using a glass stirrer. UV radiation renders photochemical oxidation during which hydroxylated benzenes or other products of photooxidation can occur (Oppenlander, 2003). Samples of the reaction mixture were taken in the time intervals of 10, 20, 30 and 55 min and analysed immediately after sampling using HPLC to prevent further photochemical or following reactions. The irradiated solution was processed using SPE and analysed using GC-MS to determine the photoreaction products.

Experiments using ferrates

A stock solution of toluene with the concentration of 0.1 mL/L was prepared. Five beakers were each filled with 100 mL of this stock solution and potassium ferrate was added to achieve ferrate anion concentration of 1, 3, 5 and 10 mg/L. The last sample contained the equimolar amount of the ferrate anion, which equals to 186 mg/L of pure potassium ferrate to toluene. Typical violet colouring of the ferrate anion appeared in the solution immediately after adding the potassium ferrate powder. The ferrate anion is a strong oxidant agent with the standard redox potential of 2.2 V against the standard hydrogen electrode in the acidic environment. After its reduction from Fe^{VI} to Fe^{III}, the solution changes its colour to slightly yellow, indicating the end of the reaction. The solution was afterwards analysed using HPLC.

Results and Discussion

Toluene degradation using UV irradiation

In the first ten minutes, UV radiation degraded from 35.4 % to almost 40 % of the initial amount of toluene, as shown in Fig. 1. At the end of the UV irradiation, for 55 minutes, the maximal degradation efficiency of 67.1 % in the sample with initial toluene concentration of 0.5 mL/L was achieved. The degradation efficiency was calculated as a relative decrease in the initial toluene concentration; therefore, quantitative toluene conversion to photochemical reaction products is obtained. Visually, the transparent toluene solution changed its colour to slightly yellow, implying the change in the structure of the molecule. Similar results were obtained by another research group who were able to degrade approx. 75 % of toluene in 60 minutes of irradiation using a 500 W high-pressure mercury lamp (Daifullah and Mohamed, 2004). However, the high-pressure mercury lamp provides multi line spectra with seven main peaks (Oppenlander, 2003). The most important peak at the wavelength of 254 nm, which is most suitable for the degradation of toluene, is not pronounced considering the other six peaks. Lower UV light intensity can be compensated by higher power of the lamp, but this is connected with higher costs due to energy consumption. Moreover, high-pressure mercury lamps are operating at the electricity-to-photon (radiant) efficiency below 20 %. In comparison, low-pressure lamps operate at the radiant efficiency of 40 % to 60 %. The epiphenomenon of low radiant efficiency is the enormous production of heat, which means that such a system needs an effective cooling system and even higher costs (Evans et al., 2013).

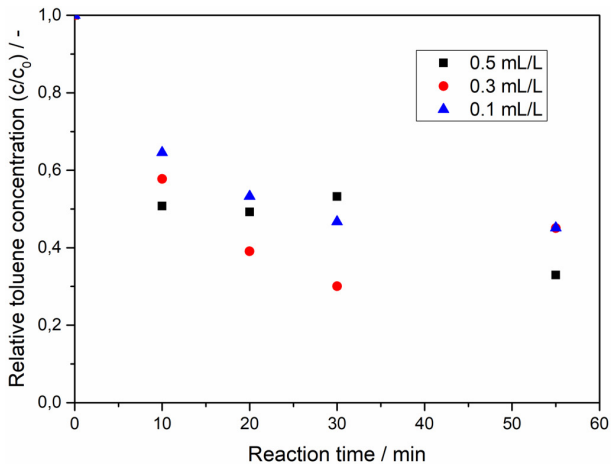

Fig. 1. Decrease in relative toluene concentration during 254 nm UV irradiation of samples with the initial toluene concentration of 0.1 mL/L, 0.3 mL/L and 0.5 mL/L.

HPLC analysis showed four degradation products. All of them eluted on the reverse phase column earlier as toluene, which suggests higher polarity in regard to the former molecule. After processing the sample using SPE, it was analysed using GC-MS. The analysis proved six photooxidation products, namely benzaldehyde, benzyl alcohol and all three isomers of cresol (ortho-, meta-, para-), which is in good accordance with the theory. The theory implies the incorporation of dissolved oxygen from the solution via a radical reaction mechanism (Oppenlander, 2003). Considering ecotoxicological properties, all reaction products are, according to applicable lethal doses data provided by the European Chemicals Agency, less toxic than toluene.

Toluene degradation using potassium ferrate

Oxidation strength of ferrates depends on the solution pH. In acidic media, the ferrate anion has a standard redox potential of 2.20 V in respect to standard hydrogen electrode. In contrast, this value drops to 0.72 V under basic conditions. During the reduction of Fe^{VI} to Fe^{III}, hydroxide anions are created. The corresponding reaction and more information can be found in Híveš et al. (2016). Therefore, finding the appropriate concentration of ferrates is essential to reach the highest degradation efficiency at the lowest cost. The pH value of samples was measured right after potassium ferrate addition (denoted as 0 min) and continuously during the oxidation in the time interval of 10 minutes, up to 30 minutes. The obtained data are graphically summarised in Fig. 2.

After the content analysis on HPLC, only two degradation products appeared in the chromatogram. As presumed, both with higher polarity than the toluene molecule. The highest degradation efficiency was achieved at 10 mg/L of ferrates (71.2 %). Nonetheless, even at ten-fold lower ferrate concentration, the oxidation was successful to a non-negligible extent. Degradation efficiencies were as follows: 52.5 % at 1 mg/L, 58.4 % at 3 mg/L, 64.3 % at 5 mg/L, 71.2 % at 10 mg/L and 56.0 % at equimolar amount of the ferrate anion. It is apparent that the highest (equimolar) concentration of ferrates resulted in almost the lowest degradation efficiency while the pH value increases. This phenomenon is in accordance with the theory and was also observed by Minetti et al. (2017) who achieved maximal degradation efficiency under slightly acidic (54 %) and neutral pH (56 %) conditions. In the basic media, the degradation efficiency decreased to 43 % (Minetti et al., 2017). However, no degradation products were reported and the paper claims that the toluene molecule was completely mineralised after 40 days of ferrate application.

Acknowledgement

This work was financially supported by the Ministry of Education, Science, Research and Sport of the Slovak Republic under the projects OP VaV ITMS 26240120034,

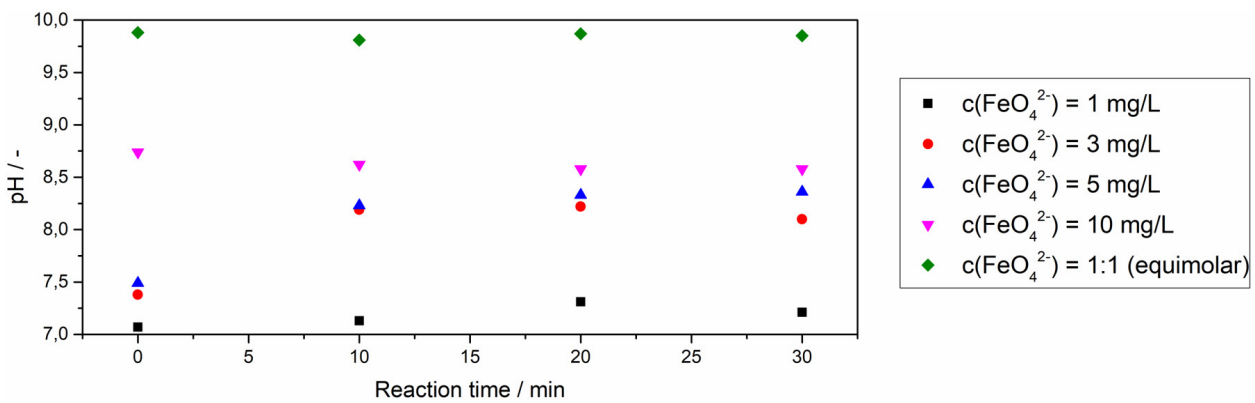

Fig. 2. Effect of potassium ferrate on pH during toluene oxidation.

VEGA 1/0343/19, APVV-17-0183 and the Young Researchers Grant within the Slovak University of Technology (ElCapFe).

References

Barboni T, Cannac M, Pasqualini V, Simeoni A, Leoni E, Chiaramonti N (2009) Int J Wildland Fire 19(5): 606–612.

Barberes GA, dos Reis RP, Spigolon ALD, Fonseca PE, de Mello CB, Barata MT (2018) Geosci. 8(1), 9.

Daifullah AHAM, Mohamed MM (2004) J. Chem. Technol. Biotechnol. 79: 468–474.

Dange AD, Masurekar VB (1981) J. Biosci. 3(2): 129–134.

dos Anjos Santos M, Távora BE, Koide S, Caldas ED (2007) Rev. Saúde Públ 47(2): 335–344.

European Chemicals Bureau (2003) European Union Risk Assessment Report Toluene. Office for Official Publications of the European Communities, Italy.

Evans R, Douglas P, Burrows H (2013) Applied Photochemistry. Springer, United States.

Faust M, Altenburger R, Backhaus T, Blanck H, Boedeker W, Gramatica P, Hamer V, Scholze M, Vighi M, Grimme LH (2003) Aquat Toxicol 63(1): 43–63.

Farinos RM, Ruotolo LAM (2017) Electrochim. Acta 224: 32–39.

Híveš J, Gál M, Kerekeš K, Kubiňáková E, Mackuľak T (2016) Electrochemical Ferrates(VI) Preparation and Wastewater Treatment. Ferrites and Ferrates: Chemistry and Applications in Sustainable Energy and Environmental Remediation. 221–240. American Chemical Society, Washington DC.

Huling SG, Hwang S, Fine D, Ko S (2011) Water Res. 45(16): 5334–5342.

Inyang IR, Puanoni AR, Izah SC (2018) MOJ Toxicol. 4(6): 440–444.

Kim SR, Ali I, Kim JO (2019) Appl. Surf. Sci. 477: 71–78.

Kubiňáková E, Kerekeš K, Gál M (2015) J Appl Electrochem 45: 1035–1042.

Kuo CH, Chen SM (1996) Ind. Eng. Chem. Res. 35: 3973–3983.

Lei YD, Wania F (2004) Atmos. Environ. 38(22): 3557–3571.

Li X, Zhou Q, Luo Y, Yang G, Zhou T (2013) Environ Sci Pollut Res Int 20(2): 957–966.

Liu Y, Zhou Q, Xie X, Lin D, Dong L (2010) Ecotoxicology 19: 1551–1559.

Leutsch F, Bertkow M (2010) A short primer on benzene, toluene, ethylbenzene and xylenes (BTEX) in the environment and in hydraulic fracturing fluids. Available at: https://environment.des.qld.gov.au/__data/assets/pdf_file/0020/87140/btex-report.pdf (Accessed 6 May 2020).

Minetti RCP, Macano HR, Britch J, Allende MC (2017) J. Hazard. Mater. 324: 448–456.

Oppenlander T (2003) Photochemical Purification of Water and Air. Wiley-VCH, Darmstadt.

Qiu L, Dong Z, Sun H, Li H, Chang C (2016) Water Environ Res 88: 1855–1875.

Rabaaoiu N, Moussaoui Y, Allagui MS, Ahmed B, Elaloui E (2013) Sep. Purif. Technol. 107: 318–323.

Ramteke LP, Gogate PR (2015) J Ind Eng Chem 28: 247–260.

Sato A, Takajima T (1979) Toxicol Appl Pharmacol 48(2): 249–256.

Sekiguchi K, Sanada A, Sakamoto K (2003) Catal Commun 4(5): 247–252.

Singh MP, Ravi Ram K, Mishra M, Shrivastava M, Saxena DK, Kar Chowdhuri D (2010) Chemosphere 79(5): 577–587.

Singh RL, Singh RP (2019) Advances in biological treatment of industrial waste water and their recycling for a sustainable future. Springer, Singapore.

van der Meijde M, van der Werff HMA, Jansma PF, van der Meer FD, Groothuis GJ (2009) Int J Appl Earth Obs 11(1): 77–82.

Xu T, Zheng H, Zhang P (2020) J. Hazard. Mater. 388: 121746.

sciendo

Degradation of low-rank coal excavated from coal-mine Záhorie by filamentous fungi

Eva Smoleňová[1], Richard Pokorný[1], Michal Kaliňák[2], Tibor Liptaj[2], Martin Šimkovič[1], Ľudovít Varečka[1]

[1]*Institute of Biochemistry and Microbiology*
[2]*Central Laboratories, Slovak University of Technology, Radlinského 9, 812 37 Bratislava, Slovakia*
ludovit.varecka@stuba.sk

Abstract: The ability of *Trichoderma* strains isolated from lignite and of Earth surface-derived strains to attack (solubilise) lignite, peat and wood was compared using glutamate as a carbon source. The results showed that lignite-derived microorganisms solubilise lignite to similar extent as *Trichoderma* strains isolated from the Earth surface. Solubilisation processes involve the action of enzymes and alkaline pH. The solubilisation of lignite was accompanied by a small increase of conidia-bound laccase, whereas that of peat was accompanied by (secretion) activity of cellulase, laminarinase, laccase, and lignin-peroxidase-like enzyme. In addition, data were obtained which show that bacteria contained in the lignite are able of lignite solubilisation and utilisation.

Key words: *Trichoderma* species, low-rank coal, solubilisation

Introduction

Since the beginning of the 1980's it is known that some micro-organisms are able to attack hard- and low-rank coals (lignite) (Fakoussa, 1981; Cohen et al., 1987; Hölker et al., 1995; Fakoussa and Hofrichter, 1999). Several species of bacteria, basidiomycetes, deuteromycetes, zygomycetes and ascomycetes able to solubilise/depolymerise this heterogenous complex organic material have been described since (Klein et al., 2001). Microorganisms use different mechanisms for an attack on the coal structure. Known strategies of ascomycetes, deuteromycetes and bacteria to solubilise lignite are the extrusion of alkaline substances, secretion of chelators, production of detergents and the action of hydrolases (Hölker et al., 1999, 2002b). Basidiomycetes use also ligninolytic enzymes e.g. lignin-peroxidase, manganese-peroxidase and laccase (Fritsche et al., 1999). More than 750 fungal species were screened to find fungi which are able to modify coal (Hofrichter et al., 1999). Microorganisms were isolated from open cast mining areas, forest fire regions, decaying wood or abandoned mines under conditions in which the probes could have been contaminated by surface microorganisms that have only incidental biological contact with coal. All known isolates from lignite were obtained from the surface and they were exposed to the environment for an undefined time. Results of solubilisation experiments were reviewed by Sekhohola et al. (2013).

Recently, several papers confirmed the capability of fungi to solubilise various types of coal (Yuan et al., 2006, Kliaĭn et al. 2013) or to remove not desired constituents of coal (Etemadzadeh et al., 2016). Supporting effects of bacteria (Liu et al., 2019) or plants (Mukasa-Mugerwa et al., 2011) in the fungal attacks of coal have been observed.

The aim of this study was to determine whether fungi of genus *Trichoderma* residing within lignite have higher lignite-solubilisation potential than their counter-parts collected from the Earth surface. Fungal species were isolated from the underground of a lignite mine (Záhorie, Slovakia) from the depth of about 170 m (Pokorný et al., 2005). Several *Trichoderma sp.* were isolated under sterile conditions from lignite and identified by sequencing of their internal transcribed spacers (ITS). Lignite-depolymerisation activity of these "indigenous" fungi was compared with that of *Trichoderma* strain isolated from the Earth surface. Solubilisation of peat and wood were also investigated.

Materials and Methods

Strains

Strains used in this work were isolated from the underground of lignite mine Záhorie, Slovakia, except for *Trichoderma sp. var. Modra*, which was isolated from the rotten wood bark found near the town Modra, Slovakia. The isolate *Trichoderma sp. var. Čáry*, was isolated from the lignite layer in the drift wall opened to air for several years after cutting off the surface layer by a sterile chisel. The same is true for *Trichoderma, var. Store* which was isolated from a compact piece of coal found at the store of freshly excavated coal. Its ITS1 sequence showed a 98 % similarity to *T. atroviride*. *Trichoderma* isolates, designated as Čelba 1 and Čelba 2 also characterised by their ITS sequences.

The obtained sequences were submitted to GenBank and are available under the accession num-

bers AY220263-AY220269. Their analyses showed that the isolated species from coal are closely related to *Trichoderma viride* and/or *Trichoderma atroviride* whereas *Trichoderma sp. var. Modra* is related to *Trichoderma pseudokoningii*.

Fungal isolates were propagated on Czapek-Dox agar supplemented with 0.5 % (w/v) yeast extract at 26 °C in dark. For experiments, conidia were scrapped from the agar surface and washed once with water and counted. Isolated bacteria were cultivated on Nutrient Broth (HiMedia) plates at 37 °C.

Isolation of microbial strains from lignite

The isolation procedure was extensively described in our previous paper (Pokorný et al., 2005). Using this procedure, both fungi and bacteria were isolated.

DNA isolation from fungi

DNA was isolated from the liquid nitrogen-frozen vegetative mycelia by phenol-chloroform extraction according to the standard procedure (Ausubel et al., 1992) with some modifications described elsewhere (Scheel et al., 1997, 1999, 2000).

Molecular typing of Trichoderma isolates

For the amplification of ITS fragments, primers ITS1 and ITS4 were used (White et al., 1990) resulting in bands at about 600 bp. For the amplification of mitochondrial small subunit rRNA gene fragments, primers MS1 and MS2 (White et al., 1990) were used giving bands at about 650 bp. The bands were purified by QIAquickGel Extraction Kit (QIAGEN) and PCR sequenced using an ABI Prism sequencer. The sequences were analysed by the ClustalX program using available *Trichoderma* ITS and mitochondrial small subunit rRNA gene sequences.

Lignite, peat, and wood solubilisation

Lignite solubilisation was performed and monitored as described elsewhere (Hölker et al., 1995) with lignite sterilisation by autoclaving in some experiments. In experiments with H_2O_2-preoxidation/sterilisation, ampicillin (100 $\mu g \cdot ml^{-1}$) was added to prevent the growth of bacteria. Peat (finely chopped peat was purchased at the local garden centre and used without treatment) solubilisation was measured in the same way but sterilisation was done by autoclaving only. Wood (beech) sawdust (fine powder was obtained from a carpenter workshop and used without treatment) was also sterilised by autoclaving and solubilisation was monitored by measuring A_{280} in the aliquots of cultivation media centrifuged, the cultivation broth was deproteinised with 10 % perchloric acid before the measurement. For inoculation, 100 ml of media inoculated with 1×10^6 conidia/ml were used. Solubilisation was carried out at 25 °C for the time indicated in the figures with 1—3 g of particulate material in 100 ml of medium.

Enzyme assays

Lignin peroxidase-assay: activity was determined spectrophotometrically by oxidation of veratryl alcohol. The reaction mixture (total volume of 3 ml) contained 1 ml of the sample, 1.95 ml of 150 $mmol \cdot l^{-1}$ Na-tartrate buffer, pH 3, and 0.67 $mmol \cdot l^{-1}$ veratryl alcohol. The reaction was started by the addition of H_2O_2 (0.12 $mmol \cdot l^{-1}$) and the change of A_{310} was measured for 1 min at 25 °C. Molar absorption coefficient, $\varepsilon = 9300\ l \cdot mol^{-1} \cdot cm^{-1}$, was used for the calculation of enzyme activity.

Mn-peroxidase-assay: the activity was assayed spectrophotometrically by Mn^{3+}-induced oxidation of phenol red (Kuwahara et al., 1984). The reaction mixture (total volume of 3 ml) contained 1 ml of the sample, 1.95 ml of 75 $mmol \cdot l^{-1}$ Na-tartrate buffer, pH 4.5, containing 0.15 $mg \cdot ml^{-1}$ phenol red, and 0.1 $mmol \cdot l^{-1}$ $MnSO_4$. The reaction was started by the addition of H_2O_2 (0.05 $mmol \cdot l^{-1}$ final) and the change of A_{610} was measured for 5 min at 25 °C.

Laccase was measured using ABTS (2,2´-azino-bis-(3-ethylbenzothiazoline-6-sulfonate)) as the substrate employing the following procedure: 3.5 ml of solubilisation mixture were centrifuged (5 min at 12 000× g) and the resulting pellet was vortexed with 1.35 ml of 100 $mmol \cdot l^{-1}$ citrate-phosphate buffer, pH 5.4. ABTS (0.3 $mmol \cdot l^{-1}$ final) was added, vortexed and incubated for 10 min at 37 °C. The reaction was terminated by centrifugation of the suspension for 2 min as above and A_{420} was measured. Reference sample (t = 0) was centrifuged immediately after substrate addition. The difference of A_{420} at 10 and 0 min and $\varepsilon = 36\ 000\ l \cdot mol^{-1} \cdot cm^{-1}$ was used to calculate enzyme activity.

Activities of amylase (α-1,4-glucanase), cellulase (β-1,4-glucanase), dextranase (β-1,6-glucanase), laminarinase (β-1,3-endoglucanase), lichenase (β-1,3-1,4-endoglucanase) and xylanase (β-1,4-xylanase) were detected using chromolytic substrates according to the following procedure: 0.1 ml aliquots of centrifuged solubilisates were diluted with 0.5 ml of 100 $mmol \cdot l^{-1}$ citrate-phosphate buffer, pH 5.4, one tablet of chromolytic substrate (corresponding polysaccharide covalently modified with blue dye) was added and the mixture was incubated for 24 h at 25 °C. The reaction was terminated by the addition of 3.5 ml of the stopping solution (5 g of Na_2CO_3, 50 ml of acetone and 450 ml of water), the suspension was centrifuged, and A_{620} of the supernatant was measured against water.

Activities of cellulase, dextranase, and laminarinase were determined also by the spectrophotometrical measurement of the release of reducing substances using the 3,5-dinitrosalicylic acid (DNS) method. The assay was performed as follows: 0.1 ml of the centrifuged solubilisate was added to 0.9 ml of 1 % suspension of the corresponding polysaccharide in 50 mmol · l^{-1} citrate-phosphate buffer, pH 7, and incubated for 5 min at 40 °C (cellulase), for 40 min at 40 °C (laminarinase), or up to 60 min at 40 °C (dextranase). In parallel, control samples were incubated for 0 min. Aliquots of 0.15 ml were withdrawn and added to 0.25 ml of 1 % (w/v) 3, 5-dinitrosalicylic acid in 0.4 mol · l^{-1} NaOH containing 30 % (w/v) of Na, K-tartrate. The solutions were boiled for 5 min, diluted with 1 ml of water, and centrifuged for 3 min at 12 000× g. A_{540} was measured against reference with 0.15 ml of water instead of the sample. All values were corrected for A_{540} obtained from zero-time samples. The amounts of reducing compounds were read from the calibration line constructed with glucose as the standard compound.

^{1}H-NMR measurements

^{1}H-NMR spectra were obtained on a Varian VXR-300 spectrometer operating at 299.943 MHz for protons. Neutralised and lyophilised samples were dissolved in D_2O in a 5-mm NMR tube and measurements were performed at ambient temperature. Chemical shifts were referenced to the internal standard – TSP (0.00 ppm). Standard ^{1}H spectra were acquired and processed using standard acquisition and processing parameters. The signal of residual water was suppressed by selective pre-saturation (5 s).

Protein determination

Proteins were determined by the Bradford method after the extraction of biomass with 0.1 mol · l^{-1} NaOH for 1 h at 70 °C followed by 5 min centrifugation at 12 000× g. Supernatant was used for protein determination.

Chemicals

ABTS, laminarine and L-glutamic acid were purchased from Sigma-Aldrich, St. Louis, MO, U.S.A.; veratryl alcohol was from Fluka, Buchs, Switzerland and T 150-dextran from Pharmacia, Uppsala, Sweden. Chromolytic substrates for the determination of amylase, cellulase, dextranase, laminarinase, lichenase and proteinase were synthesised and generously provided by Dr. Ľudovít Kuniak, from the Department of Food Technology, Slovak University of Technology, Bratislava, Slovakia. Other chemicals were purchased from Microchem, Pezinok, Slovakia, or from Lachema, Brno, Czech Republic.

Results

Solubilisation experiments

Solubilisation experiments were performed with *Trichoderma sp. var. Čáry* using 1.2 % L-glutamate as the carbon source (substitution of glutamate by glutamine or α-oxoglutaric acid did not significantly influence the solubilisation process). The amount of solubilisate was dependent on the mass of lignite added (Fig. 1). The presence of glutamate (or glutamine, or α-oxoglutaric acid-not shown) led to the alkalinisation of the medium to pH of about 8 in the course of solubilisation. It should be noted that the capability of this fungus to solubilise lignite gradually decreased within one year to about 30 % of the values obtained using fresh isolate without any changes in the measured enzyme activities or growth rate (not shown). The efficiency of solubilisation of two "indigenous" *Trichoderma* strains (Čelba 1 and Čelba 2) and of (not necessarily "indigenous") *Trichoderma sp. var. Čáry* (or *Trichoderma sp., var. Store*) strains did not differ dramatically from that of the strain used in previous experiments (Hölker et al., 1999), although individual isolates differed from each other (Fig. 1). Lignite dry mass decreased during the solubilisation process after 30 days of cultivation by approximately 10 % for Čelba 1 and 20 % for Čelba 2.

The next experiment was focused on the lignite solubilisation activity of the tested fungi being due to media alkalinisation or activation of specific enzymatic mechanism. Lignite solubilisation was performed with glutamate or sucrose as the carbon source in a heavily buffered medium (100 mmol · l^{-1} Tris/HCl, pH 8). It was found that the buffered alkaline medium leads to stronger solubilisation than the non-buffered one. Moreover, the ability to solubilise lignite was no more restricted to the amino acids or carboxylic acids as carbon source and proceeded with the same intensity, even better, with sucrose as the carbon source (Fig. 2). As sucrose is a metabolically more efficient carbon source than glutamate, this experiment indicates that also other aspects of fungal metabolism beside media alkalinisation contribute to lignite solubilisation.

Solubilisation activity of *Trichoderma* was tested also with less mineralised substrates, i.e. peat and wood sawdust. It was found that *Trichoderma sp. var. Čáry* solubilises autoclave-sterilised peat with the solubilisate yield comparable to that from lignite (Fig. 3). The use of wood (beech) sawdust as particulate material led to the release of soluble compound(s)

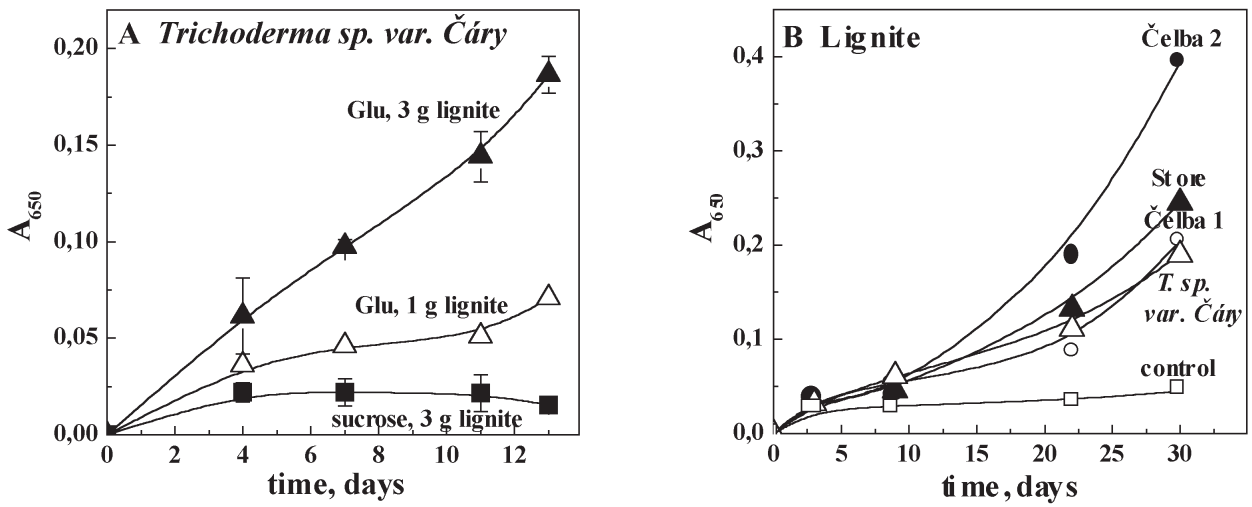

Fig. 1. Solubilisation of lignite by *Trichoderma* isolates.
A: Dependence of solubilisation on the mass of sterilised lignite using glutamate or sucrose as carbon sources. The process was carried out as described in Materials and Methods.
B: Comparison of lignite solubilisation activity of recent and fossile strains of *Trichoderma*. *Trichoderma* isolates: isolate *Trichoderma sp. var. Čáry* (open triangles) was isolated from the surface of the lignite layer in a drift wall (lignite mine Záhorie, Čáry, Slovakia) opened several years ago, isolate named as "Store" (closed triangles) was isolated from the surface lignite store in this mine and isolates named as "Čelba 1" (open circles) and "Čelba 2" (closed circles) were isolated from the underground place called "Čelba" where a tunnel-drilling machine is operated. Solubilisation was carried out with 1 g of sterilised lignite per assay and the procedure described in Materials and Methods was followed. Control (open squares) was represented by non-inoculated sterilised lignite. Glutamate (2 % w/v) was used as carbon source.

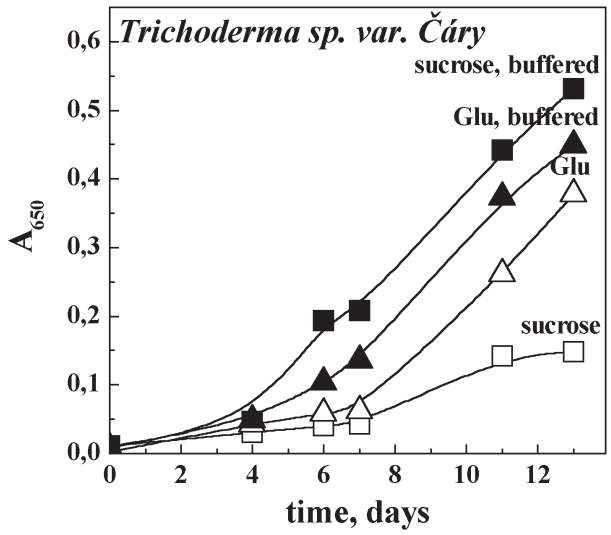

Fig. 2. Effect of buffering on solubilisation activity of *Trichoderma sp. var. Čáry* with sucrose and glutamate as carbon sources in non-buffered or buffered medium.
The experiment was performed as described in Materials and Methods with 3 g of sterilised particular material using glutamate (open triangles) or sucrose (open squares) (2 % w/v) as carbon sources. In case of buffered samples (closed symbols), the medium was prepared in 100 mmol · l^{-1} Tris/HCl buffer, pH 8.0.

absorbing at 280 nm (Fig. 3) not precipitable by boiling. The release of pigmented material was not detectable under the experimental conditions. Microscopic observation of sawdust particles after nine-day-treatment revealed that the particles remained intact and had a fibrillar character.

As the ability to solubilise solid materials does not seem to be restricted to lignite, also microorganisms other than fungi were tested for their lignite solubilisation activity. Therefore, an attempt was made to solubilise coal with microflora present in lignite. In the experiment shown in Fig. 4, non-sterilised lignite powder was used as the substrate. It was found that the microflora on non-sterilised lignite solubilised lignite to a higher extent than *Trichoderma* isolates. It should be noted that airborne microorganisms were present in the culture in addition to those present in lignite. Bacteria were predominant in the culture after 25 days of solubilisation, which caused increased turbidity of the suspension confirmed by microscopic observations (not shown). The bacterial species were not identified. Hence, it is possible that non-sterile lignite is easier to solubilise microbially than the autoclaved one (Fakoussa personal communication, see also Fakoussa and Hofrichter, 1999). Thus, the potential of bacteria in lignite solubilisation should be explored in the future.

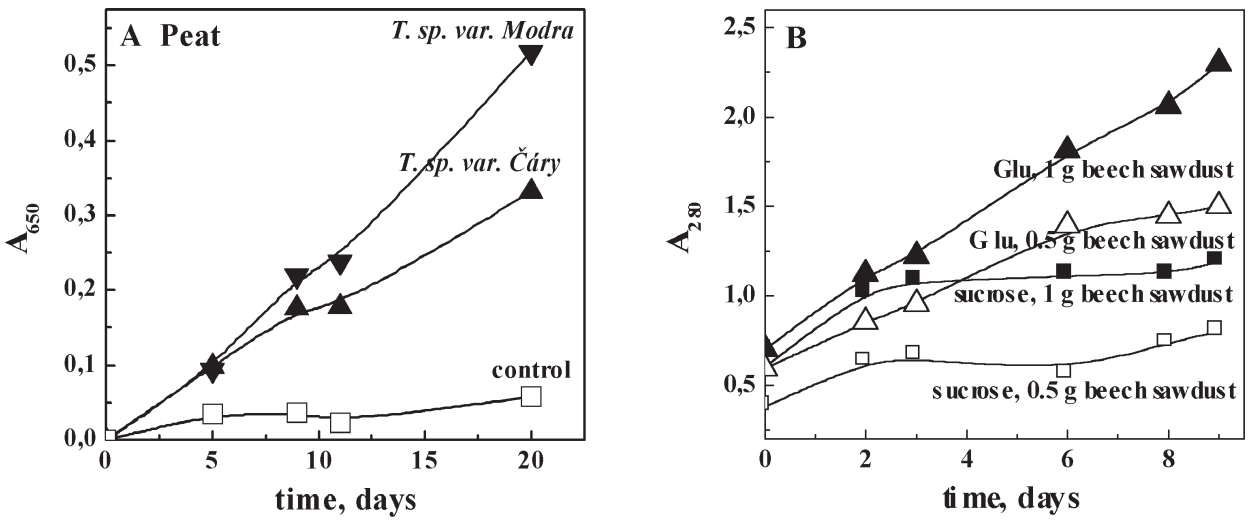

Fig. 3. Solubilisation of peat and wood sawdust by *Trichoderma* species.
A: Experiments were performed with sterilised peat (1.5 g) inoculated with *Trichoderma sp. var. Čáry* (closed upward triangles) or with *Trichoderma sp. var. Modra* (closed downward triangles). Non-inoculated sterilised peat was analysed in parallel as control (squares). Glutamate (2 % w/v) was used as the carbon source.
B: Media with indicated carbon sources and mass of sterilised beech sawdust were treated as described in Materials and Methods. Samples withdrawn at indicated time were centrifuged (20 min, 14000× g) and A_{280} was measured in aliquots against the medium without sawdust and inoculum. A_{280} of non-diluted samples are shown.

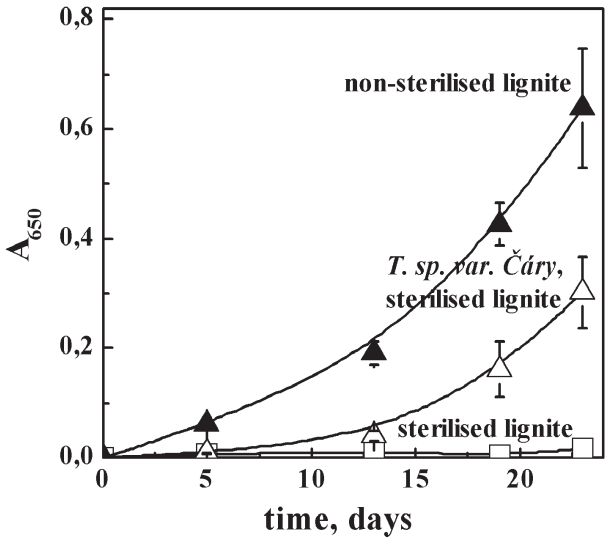

Fig. 4. Comparison of solubilisation activity of added *Trichoderma sp. var. Čáry* and indigenous microorganisms present in non-sterilised lignite. Media were inoculated with identical number of conidia using sterilised (open triangles) or non-sterilised (closed triangles) coal samples (kept in closed sterile containers) and solubilisation was carried out in duplicate assays as described in Materials and Methods with 1.5 g of particular material. Control (open squares) with sterilised lignite and without inoculation was proceeded in parallel.

Growth of Trichoderma in lignite solubilisation experiments

Solubilisation process initiated by inoculation with conidia starts after a delay of 1–7 days in different experiments. The life cycle of filamentous fungi shows that germination of conidia and the beginning of the vegetative growth occur during the solubilisation lag phase. The presence of mycelia was observed in the first days of cultivation together with conidia and mostly conidia were present in the final phase of the experiment (not shown). The mass of protein extracted from the culture increased gradually and remained constant until the end of the experiment. When the medium was inoculated with vegetative mycelium, its mass increased in a similar time interval (Fig. 5). When non-sterilised lignite was used as the inoculum, the protein mass in the culture increased at a lower rate in an almost linear time course over a period of 27 days. This can be explained by the growth of several populations of micro-organisms with different multiplication times.

Enzyme activities of Trichoderma species during lignite and peat solubilisation

Lignite solubilisation medium in the presence or absence of fungus did not display any enzymatic activity mentioned in Materials and Methods except for minute laccase activity when particulate material was taken as the enzyme source (Table 1).

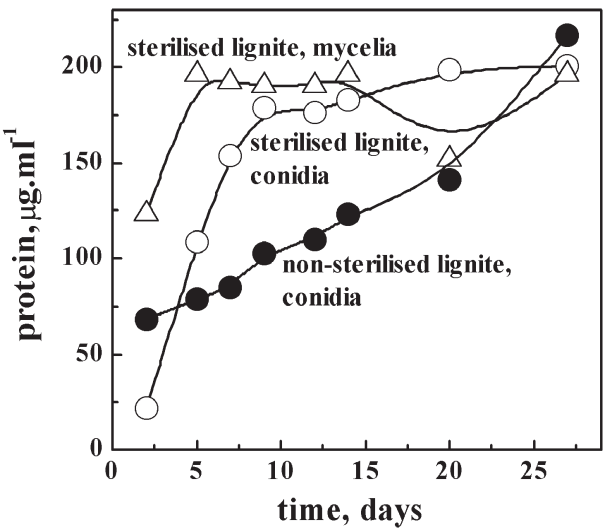

Fig. 5. Changes in protein content in the culture of *Trichoderma sp. var. Čáry* during the solubilisation experiment after inoculation with mycelia or conidia.
Sterilised lignite (1.5 g) was inoculated with conidia (open circles) or 24 h old mycelia corresponding to 80 μg/ml of protein (open triangles). In parallel, non-sterilised lignite was inoculated with conidia as the control (closed circles). At indicated time, aliquots of medium were withdrawn, and the protein content was determined after alkaline extraction of proteins as described in Materials and Methods.

However, peat solubilisation revealed the presence of several enzymes with activities dependent on the age of the culture. Besides the activity of laccase, also that of a veratryl-alocohol oxidising, lignin-peroxidase-like enzyme was found as well as activities of cellulase, xylanase, laminarinase, amylase, lichenase, and proteinase which were detected using chromolytic substrates. These results are not shown as the chromolytic substrates required long-term incubation and are regarded as preliminary. Cellulase and laminarinase activities were measured by the DNS method at various stages of the experiment (Table 1). Activities of these enzymes were differently localised. Whereas the lignin-peroxidase-like activity was present in the supernatant after spinning down the particulate material (i.e., coal particles and microbes), laccase activity was connected to microbial cells (conidia) (Table 1).

Characterisation of solubilisation products

Solubilisate obtained from lignite or peat after spinning down the particulate material (20 min, 12 000× g) was the true solution which could be filtered through a 0.22 μm nitrocellulose membrane filter without retaining A_{650}. However, the material absorbing at A_{650} was not dialysable through the dialysation membrane with the cut-off of about 5 kDa (not shown). This indicates that the solubilisate is water-soluble polymer. UV spectra of the solubilisate showed a broad shoulder at 250–

Tab. 1. Enzyme activities in lignite solubilisate by *Trichoderma sp. var. Čáry*. Results are typical of three similar experiments. Note that laccase was measured in the suspension whereas other enzymes were measured in the medium devoid of particulate material.

Carbon source	Enzyme	Day of 1st measurement / activity [1]	Day of 2nd measurement / activity [1]	Day of 3rd measurement / activity [1]	*Trichoderma* strain
Lignite	Laccase	9 / 0.5 pkat.mg $_p^{-1}$	20 / 3.2 pkat.mg $_p^{-1}$	23 / 4.0 pkat.mg $_p^{-1}$	*T. sp. var. Čáry*
Lignite	Laccase	9 / 2.3 pkat.mg $_p^{-1}$	20 / 4.2 pkat.mg $_p^{-1}$	23 / 5.3 pkat.mg $_p^{-1}$	*T. sp. var. Modra*
Peat	Laccase	9 / 8.8 pkat.mg $_p^{-1}$	20 / 7.1 pkat.mg $_p^{-1}$	23 / 8.0 pkat.mg $_p^{-1}$	*T. sp. var. Čáry*
Peat	Laccase	9 / 10.9 pkat.mg $_p^{-1}$	20 / 12.8 pkat.mg $_p^{-1}$	23 / 15.0 pkat.mg $_p^{-1}$	*T. sp. var. Modra*
Peat	Lignin-peroxidase-like activity	7 / 4.8 nkat.ml^{-1}	11 / 3.1 nkat.ml^{-1}	20 / 0 nkat.ml^{-1}	*T. sp. var. Čáry*
Peat	Lignin-peroxidase-like activity	7 / 2.4 nkat.ml^{-1}	11 / 5.6 nkat.ml^{-1}	20 / 0 nkat.ml^{-1}	*T. sp. var. Modra*
Peat	Cellulase	6 / 23 nkat.ml^{-1}	12 / 43 nkat.ml^{-1}	21 / 0 nkat.ml^{-1}	*T. sp. var. Čáry*
Peat	Cellulase	6 / 17 nkat.ml^{-1}	12 / 28.5 nkat.ml^{-1}	21 / 11 nkat.ml^{-1}	*T. sp. var. Modra*
Peat	Laminarinase	6 / 2.4 nkat.ml^{-1}	12 / 4.6 nkat.ml^{-1}	21 / 0 nkat.ml^{-1}	*T. sp. var. Čáry*
Peat	Laminarinase	6 / 8.2 nkat.ml^{-1}	12 / 5.8 nkat.ml^{-1}	21 /0 nkat.ml^{-1}	*T. sp. var. Modra*

[1] mg $_p$ = mg of proteins

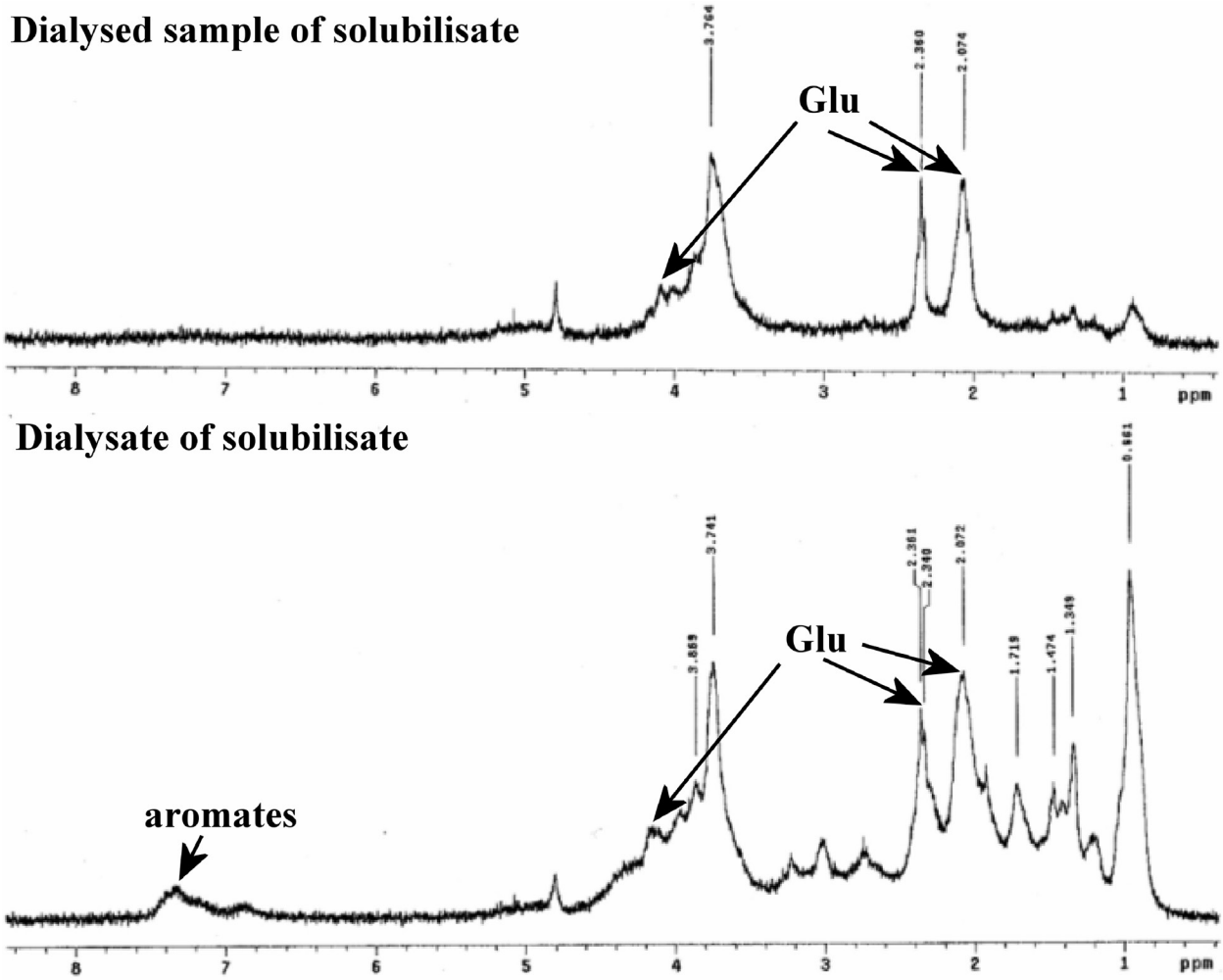

Fig. 6. ^{1}H-NMR spectra of both non-dialysable and dialysable fractions of solubilisate. Solubilisate from 100 ml of medium (produced by *Trichoderma sp. var. Čáry*) was centrifuged 10 min at 14 000× g and dialysed against 1 l of water for three days. Both dialysed sample (upper panel) and dialysate (lower panel) were lyophilised. Lyophilisates were dissolved in deuterated water and ^{1}H-NMR spectra were measured as described in Materials and Methods.

290 nm which was absent in the coal suspension cultivated under identical cultivation conditions without inoculation with fungus (*Trichoderma sp., var. Čáry*) for 30 days (not shown). Dialysed and lyophilised solubilisate was analysed by ^{1}H-NMR (Fig. 6, upper panel). Phenolic moieties typical for lignin are hardly visible in this spectrum (about 7.35 ppm) probably due to the polymeric state of the molecule. In parallel, ^{1}H-NMR spectrum of lyophilised dialysate (i.e. dialysable part of the solubilisate) showed the presence of phenolic compounds (6.9 and 7.35 ppm) as well as of glutamate; however, the complexity of spectra and broadening of bands did not enable identification of other compounds. At present, dialysable solubilisate is fractionated into groups according to charge and polarity with the aim to simplify the mixture enabling thus its ^{1}H-NMR or GC/MS analysis.

Lignite solubilisation product as carbon source for bacteria

A paper by Hölker et al. (1999) and the above experiments (Figs. 1 and 6) indicate that fungi are able to convert a part of the solubilisate to less complex compounds. Other experiments indicate (Figs. 4 and 5) that bacteria are equally capable of lignite solubilisation. Further degradation of the solubilisate by bacteria was tested. For these experiments, bacterial strains isolated from lignite were chosen similarly as fungi (see Materials and Methods). Individual isolates (Ba4, Ba5, Ba8A, Ba8B, Ba9A, Ba9B) were identified as gram-negative bacilli (not shown) and their molecular typisation will be done later. Sterilised solubilisate was inoculated with liquid exponential culture of bacteria grown on the MP medium. The culture growth was monitored by measuring A_{600} against the sterilised solubilisate

(not shown), or by the increase of protein content in the solubilisate (Table 2). After removing bacteria and lignite, the medium was dialysed, lyophilised and analysed as above. In culture Ba5, the lyophilisate did not dissolve completely in water and the presence of polymeric material not soluble either in organic solvents or in detergents was identified. Solubilisates from other cultures were completely soluble in water; however, their ^{1}H-NMR spectra were very similar to those shown in Fig. 6 (not shown).

Tab. 2. Increase in biomass measured as protein content during the cultivation of lignite-borne bacteria with lignite solubilisate obtained from the isolate *Trichoderma sp. var. Čáry*. The solubilisate was dialysed, lyophilised, and dissolved with water to the original volume. After sterilisation, the medium was inoculated with suspensions of bacterial isolates and submerged to be cultivated for 13 days. Protein content was measured immediately after the inoculation and after the end of the cultivation by the Bradford method.

Isolate	Protein content in the medium, $\propto$g·ml^{-1}	
	Day 0 (inoculum)	**Day 13** (end of cultivation)
Ba4	3.76	16.12
Ba5	3.42	15.25
Ba8A	3.01	16.42
Ba8B	3.01	14.65
Ba9A	3.11	17.81
Ba9B	3.11	18.61

Discussion

Since the search for coal degrading microorganisms has started, a number of fungal species from the surface of coal pieces (Kitamura et al., 1993), rotten wood and litter (Hofrichter and Fritsche, 1996) or in 0.5—20 years-old forest fire regions (Bublitz et al., 1994) have been screened.

Fungi used in this paper were isolated from the underground of a lignite mine from the depth of about 170 meters. In fact, *Trichoderma* species are rather rare fungal species, but a number of fungal and bacterial strains were isolated which remain to be characterised. These micro-organisms were tested for their ability to attack the surrounding macromolecular matrix and the results show that *Trichoderma* species derived from underground coal are capable to attack coal similarly to that of *Trichoderma* strains isolated from the Earth surface (Hölker et al., 1999).

Solubilisation of lignite observed above is a complex process. First, it requires an alkaline medium created by the transport and metabolism of carboxylic and/or amino acids (Hölker et al., 1995, 1999; Figs. 1 and 2). This process, however, does not seem to be the final stage of the fungal action on lignite as also dialysable compounds are present in the solubilisate (Fig. 6) and enzyme activities other than hydrolases were induced during the solubilisation process (Table 1).

The experiment shown in Fig. 5 indicates that both conidia and vegetative mycelia are effective in the solubilisation process. When conidia were used as inoculum, they developed to mycelia which, after about 5—7 days, differentiated into the next generation-conidia. The time course of appearance of oxidative enzymes (Conesa et al., 2002) participating in coal solubilisation (Hölker et al., 2002a, 2002b; Laborda et al., 1999; Ralph and Catcheside, 1999; Table 1) indicates that these enzymes appear in the phase of cultivation where no mycelia were observed, thus suggesting their activity during the conidia formation and/or maturation. It is remarkable that these enzymes appear only temporarily in the medium (Table 1). If they were induced by lignite-derived compounds, a different time course of induction would be expected. Therefore, it seems more probable that their activity is primarily involved in processes proceeding simultaneously with the degradation of lignin, e.g. maturation of conidia, although they could be involved in the degradation of the complex substrate. These results also indicate that conidia present in the (submerged) culture are not dormant structures but that they are metabolically active. This is supported by the fact that also less complex substrates, such as peat or wood (Fig. 3), are degraded using the above solubilisation method which is accompanied by the appearance of both oxidoreductases and hydrolases (Table 1).

Although our work has been focused on the solubilisation of coal by fungi, some experiments indicated that bacteria are equally if not more effective in attacking coal (Fig. 4) and the increase of biomass indicates that bacteria can use the solubilisate as a carbon source (Table 2). Metabolic products of both bacterial and fungal attack on coal remain to be identified.

In summary, solubilisation of coal is feasible and can be used for the transformation of at least a part of solid coal to soluble compounds and/or biomasss.

Acknowledgement

This work was supported by the project Creating the Competence Center for Research and Development in the Field of Molecular Medicine (ITMS 26240220071).

References

Ausubel F, Brent R, Kingston RE, Moore DD, Seidman JG, Smith JA, Struhl K (1992) Short protocols in molecular biology. Wiley & Sons, New York.

Bublitz F, Günther T, Fritsche W (1994) Fuel Proceeding Technology 40, 347–354.

Cohen MS, Bowers WC, Aronson H, Gray ET Jr. (1987) Applied and Environmental Microbiology 53: 2840–2843.

Conesa A, Punt PJ, van den Hondel CA (2002) Journal of Biotechnology 93: 143–158.

Etemadzadeh SS, Emtiazi G, Etemadifar Z (2016) Current Microbiology 72: 707–715. doi: 10.1007/s00284-016-1008-x.

Fakoussa RM (1981) PhD Thesis (in German), University of Bonn, Germany.

Fakoussa RM, Hofrichter M (1999) Applied Microbiology and Biotechnology 52: 25–40.

Fritsche W, Hofrichter M, Ziegenhagen D (1999) In: Steinbüchel A. (Ed.), Biochemical Principles and Mechanisms of Biosynthesis and Biodegradation of Polymers (pp 265–272). Wiley-VCH Verlag GmbH, Weinheim.

Hofrichter M, Fritsche W (1996) Applied Microbiology and Biotechnology 47: 419–424.

Hofrichter M, Ziegenhagen D, Sorge S, Ullrich R, Bublitz F, Fritsche W (1999) Applied Microbiology and Biotechnology 52: 78–84.

Hölker U, Fakoussa RM, Höfer M (1995) Applied Microbiology and Biotechnology 44: 351–355.

Hölker U, Ludwig S, Scheel T, Höfer M (1999) Applied Microbiology and Biotechnology 52: 57–59.

Hölker U, Dohse J, Höfer M (2002a) Folia Microbiologica 47: 423–427.

Hölker U, Schmiers H, Grosse S, Winkelhöfer M, Polsakiewicz M, Ludwig S, Dohse J, Höfer M (2002b) Journal of Industrial Microbiology and Biotechnology 28: 207–212.

Kitamura K, Ohmura N, Saiki H (1993) Applied Biochemistry and Biotechnology 38: 1–13.

Klein J, Fakoussa RM, Hölker U, Hofrichter M, Schmiers H, Sinder C, Steinbüchel A (2001) In: Rehm, H. J. (Ed.) Biotechnology, Vol 10 (pp 153–189), Wiley-VCH Verlag GmbH, Weinheim.

Kliaĭn OI, Kulikova NA, Konstantinov AI, Fedorova TV, Landesman EO, Koroleva OV (2013) Priklady Biokhimii i Mikrobiologii 49: 292–300.

Kuwahara M, Glenn JK, Morgan MA, Gold MH (1984) FEBS Letters 169: 247–250.

Laborda F, Monistrol IF, Luna N, Fernandez M (1999) Applied Microbiology and Biotechnology 52: 49–56.

Liu Y, Zhu J, Gao W, Guo Z, Xue C, Pang J, Shu L (2019) Environmental Sciences Pollution Research International 26: 34368–34376. doi: 10.1007/s11356-019-06567-z.

Mukasa-Mugerwa TT, Dames JF, Rose PD (2011) Biodegradation 22: 129–141. doi: 10.1007/s10532-010-9382-8.

Sekhohola LM, Igbinigie EE, Cowan AK (2013) Biodegradation 24: 305–318

Ralph JP, Catcheside DE (1999) Applied Microbiology and Biotechnology 52: 70–77.

Scheel T, Mönkemann H, Hölker U, Ludwig S, Höfer M (1997) In: Ziegler A, van Heek KH, Klein J, Wanzel W (Eds.), Proceedings of ICCS (pp 1677–1679). P&W Druck und Verlag, Essen.

Scheel T, Hölker U, Ludwig S, Höfer M (1999) Applied Microbiology and Biotechnology 52: 66–69.

Scheel T, Höfer M, Ludwig S, Hölker U (2000) Applied Microbiology and Biotechnology 54: 686–691.

White TJ, Bruns T, Lee S, Taylor J (1990) In: Innis MA, Gelfand DH, Sninsky JJ, White TJ (Eds.), PCR Protocols: A guide to methods and applications (pp 315–322), Academic Press, New York.

Yuan HL, Yang JS, Wang FQ, Chen WX (2006) Priklady Biokhimii i Mikrobiologii 42: 59–62.

sciendo

Spectro-chemometric determination of panthenol enantiomeric excess in pharmaceutical products

Roman Poláček[1], Angela Kleinová[2], Pavel Májek[3]

[1]*EUROFINS BEL/NOVAMANN s.r.o., Komjatická 73, 940 02 Nové Zámky, Slovak Republic*
[2]*Polymer institute, Slovak Academy of Sciences, Dúbravská cesta 9, 845 41 Bratislava, Slovak Republic*
[3]*Institute of Analytical Chemistry, Faculty of Chemical and Food Technology, Slovak University of Technology, Radlinského 9, 812 37 Bratislava, Slovak Republic*
pavel.majek@stuba.sk

Abstract: Antibiotic, soothing and healing properties of panthenol are exploited in various pharmaceutical and cosmetic products. Only D-panthenol is biologically active while its L-form might counteract the biological effectiveness of the D-enantiomer. Hydrating and moisturizing effects are exhibited by both enantiomers. Therefore, it is necessary to develop a rapid and cheap method for the determination of panthenol enantiomeric excess in pharmaceutical preparations. In this study, β-cyclodextrin was used as a chiral selector for the recognition of panthenol enantiomers. Inclusion complexes formed by β-cyclodextrin and the analyte showed small differences in NIR and UV/VIS spectra compared by chemometric assessment. Based on the figure of merit and model characteristics, PLS calibration model in the selected range of NIR spectra is preferred. UV/VIS spectrometry has the disadvantage of complicated sample preparation compared to NIR spectrometry. Results reached by both proposed methods were in good agreement. Statistical investigation of the results (by Student *t*-test and Fisher *F*-test) confirmed that the proposed methods are comparable and applicable to chiral analysis of panthenol pharmaceutical preparations.

Keywords: chiral analysis, panthenol, pharmaceutical preparations, molecular spectrometry, multivariate calibration

Introduction

D-panthenol (D-(+)-2,4-dihydroxy-N-(3-hydroxypropyl)-3,3-dimethybutylamide) is an alcoholic analogue of pantothenic acid, a member of the B complex vitamins (vitamin B5). It is also known as pantothenyl alcohol or provitamin B5. It is found in various commercial products, e.g. skin creams, hair preparations, eye drops as well as in tablets or injections for its anti-inflammatory and regenerating properties (Ebner et al., 2002). Dexpanthenol is enzymatically oxidized to pantothenic acid, which is a constituent of coenzyme A. The acid form plays an important role in the Krebs cycle and metabolism of lipids, proteins, and hormones. The lack of pantothenic acid causes many kinds of deficiency disease, irritation of skin, dermatitis, depigmentation of hair and stunted growth (Khater et al., 2015).

Only D-panthenol is biologically active while the L-form is at the best biologically inert and might even partly counteract the biological effectiveness of the D-enantiomer. On the other hand, both D- and L-panthenol appear to have hydrating and moisturizing effects on the skin because both enantiomers chemically attract water (König et al., 1985; Takashi et al., 1989). The above mentioned properties are very important for the enantiomeric excess (EE) determination of panthenol in pharmaceutical preparations. Chiral analysis of panthenol is usually performed by HPLC (Xie et al., 2009; Mao et al., 2010; Hroboňová et al., 2019) or GC methods (Takashi et al., 1989; Jeong et al., 1999; Abe et al., 2000) or by recently developed supercritical fluid chromatography (Khater et al., 2015). Determination of panthenol EE by a spectrometric technique with multivariate calibration (MVC) has not been reported yet. Moreover, this connection offers many advantages compared to traditional chiral methods. The rapidity and simplicity of these methods is appealing and reduces the analytical time and cost of chiral analysis because there is no need of expensive chiral columns and large amount of solvents. Chiral analysis of various drugs by infrared spectrometry with chemometric evaluation of data was performed. Main features of UV/VIS spectrometry with MVC methods can be found in the review by Poláček et al. (2016).

Our research focuses on the feasibility of panthenol EE determination by NIR and UV/VIS spectrometry by MVC methods using β-cyclodextrin (β-CD) as the chiral selector. MVC me-

thods, principal component regression (PCR) and partial least square method (PLS) were compared for the best identification of panthenol enantiomers from NIR and UV/VIS spectral data. The studied methods were applied to the chiral analysis of panthenol in pharmaceutical preparations, e.g. panthenol tablets and eye drops containing panthenol as an adjuvant.

Materials and methods

Reagents and methods

Experiments were performed using chemicals of analytical reagent grade and doubly distilled water. D- and DL-panthenol, native β-CD, p-dimethylaminobenzaldehyde, acetonylacetone and methanol were purchased from Sigma-Aldrich (United States). Ammonia and sodium carbonate were obtained from Centralchem (Slovakia).

Stock solutions of D and DL-panthenol (45 mmol · L^{-1}) for NIR measurements were prepared by dissolving 4.5 g of each enantiomer in β-CD solution (45 mmol · L^{-1}). Pure β-CD solution at the same concentration was used as a blank.

To perform UV/VIS measurements; 100 mg of each panthenol enantiomer was dissolved and made up with water to 250 mL in a volumetric flask. Then, 2 mL of these stock solutions were pipetted into 25 mL volumetric flasks and an appropriate amount of acetonylacetone solution (1 mL/100 mL 0.5 mol · L^{-1} of sodium carbonate) with 10 mL of methanol was added. Subsequently, the flask was put into a water-bath at 95—98 °C for 30 min. Upon cooling, 2 mL of p-dimethylaminobenzaldehyde solution were added into the flask which was shaken properly. The mixed solutions were made up to the final volume with methanol. After 15 min, appropriate volumes of these solutions were transferred into 10 mL flasks (total concentration of panthenol was 0.8 mmol L^{-1}) and filled up with β-CD solution (0.8 mmol · L^{-1}) to the mark. The blank solution was prepared using 2 mL of distilled water instead of the panthenol solution.

All solutions for each measurement were prepared daily.

Samples

Pharmaceutical products were purchased from a local pharmacy. Panthenol tablets contain 100 mg of panthenol per tablet and two eye drops consist of 10 mg · L^{-1} of panthenol in the drops base.

After homogenization of ten tablets, corresponding amounts were weighted and handled according to the above procedures. Aliquot parts of drops' samples were pipetted and processed for both proposed methods as pure substance.

Apparatus

UV/VIS spectrometry

VIS absorption spectra from 400 to 700 nm with 1 nm resolution were recorded by a UV/VIS spectrometer (Thermo Scientific, USA) equipped with a 1.0 cm long quartz cell at the room temperature. Scan speed was 200 nm · min^{-1}. Spectral range between 450 and 650 nm (201 spectral points) was used to create multivariate calibration models.

NIR spectrometry

Near-infrared absorption spectra in the range from 4000 cm^{-1} to 12000 cm^{-1} (2500—833 nm) with 2 cm^{-1} resolution were collected using a spectrophotometer NICOLET 8700TM (Thermo Scientific, USA) equipped with a quartz cell with an optical path of 5 mm. An average of 150 scans was performed to obtain the final spectrum.

Chemometric data analysis

Spectral data were exported to ASCII data files and calculations were performed by MATLAB 2015b (The MathWorks Inc., USA, 2015) and PLS Toolbox version 8.1 (Eigenvector Research Inc., USA, 2015). EE of panthenol was determined from NIR and UV/VIS spectral data by PCR and PLS MVC methods. In molecular spectrometry, MVC methods are extensively used as they allow for a large number of predictor variables and tolerate correlations between these variables within the measured spectral data (Wise et al., 2007). In the calibration process, a mathematical model has been built up to assign the spectral data to the desired concentration. Each calibration model was tested by a cross-validation method (CV) to estimate the prediction error with the basic idea to divide the available data into two parts: training data and testing data, respectively. Training data are used for fitting the model, while testing data are used for validating the prediction performance of the model. Decomposition of original spectral matrix into a new data matrix in PCR and PLS is realized in a different way. PCR only considers spectral data within the transformation process and generates latent variables from the independent ones while PLS actively sets up a model using two sets of latent variables during the transformation, which involves both spectral and concentration data. The new matrix consists of principal components that are all orthogonal to each other. The first principal component has the highest variance in the spectral data, while the remaining variance is used to find the next principal component, etc. To determine the optimal number of components, the root mean square error of cross-validation (RMSECV) is calcu-

lated for each model separately. The first model is constructed only from the first component and the next one is created from the progressively growing number of components. The lowest RMSECV value helps to select an optimal calibration model. The most suitable regression is chosen by assessing the performance of prediction models characteristics based on the root mean square error of the calibration (RMSEC), the root mean square error of cross-validation (RMSECV), the root mean square error of prediction (RMSEP) and scaled RMSEP against actual value, the root mean square relative error of prediction in percent (RMSE %RE) (Wise et al., 2007). The PCR method was described in earlier papers (Wise et al., 2007; Okonkwo et al., 2013) and more information on PLS can be found in Wold et al. (2001) and Wise et al. (2007).

MVC calibration models enable describing even small spectral changes and fluctuations in data, originating in various interactions between inclusion complexes formed by enantiomers of panthenol and β-CD. Data from NIR and UV/VIS spectrometry were used to construct such calibration models.

As for the calibration models samples preparation, 100 samples were prepared by mixing D-panthenol (with the mole fraction from 50.0 % to 100.0 %) and L-panthenol (in the interval of 0–50 %). These samples, which form inclusion complexes with β-CD, have a fixed total panthenol guest concentration and a fixed β-CD host concentration. The PCR and PLS calibration models were built based on the spectral data obtained from the measurements of 70 samples and 30 samples were used for their cross-validation. No interference in the measured ranges of the proposed methods was observed. After choosing the most suitable models, enantiomeric compositions in pharmaceutical preparations were predicted by both MVC methods. Autoscale pre-processing with leave-one-out cross-validation was performed for the calibration, prediction, and sample datasets.

Analytical figure of merit

Net analyte signal (NAS), defined as a part of the measured signal unique for the considered enantiomer, is used for the characterization of MVC model quality. These values are used to estimate the figure of merit in calibration models using equations described in an earlier study (Ferré et al., 2003).

The root mean square percent relative error (RMS %RE) is a useful figure of merit for quantitatively expressing the predictive efficiency of models (Williams et al., 2006).

Results and discussion

NIR spectrometry

Fig. 1 shows the NIR spectra of D-panthenol, panthenol in a racemic mixture, and their inclusion complexes with β-CD measured in a 5 mm pathlength cell.

As shown in the NIR spectra in Fig. 1, spectral changes in panthenol enantiomers and their diastereomeric complexes with β-CD can be observed.

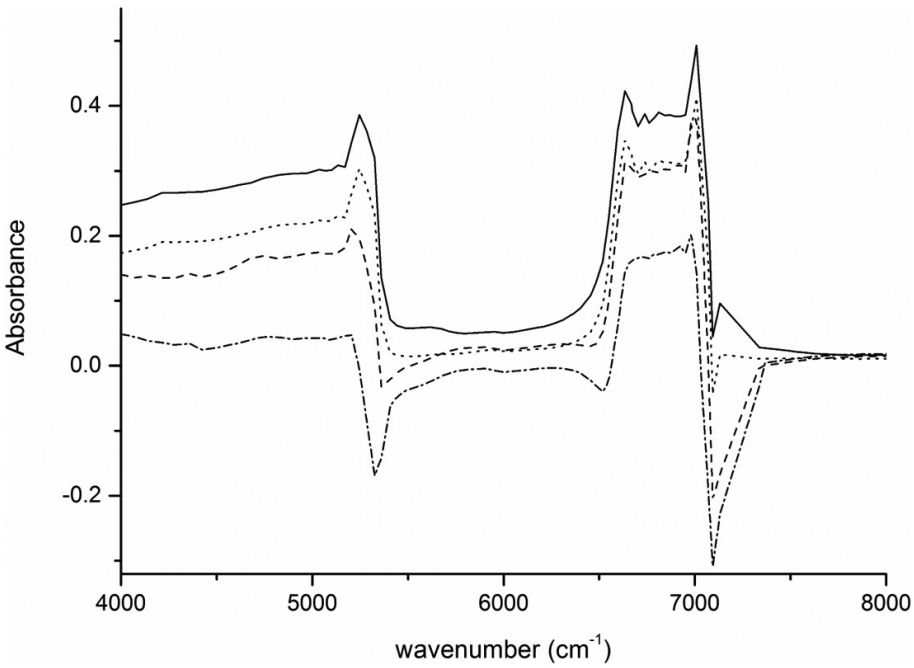

Fig. 1. NIR spectra of panthenol racemic mixture (solid line), D-panthenol (dotted line), complexes of β-CD with DL-panthenol (dashed line) and dexpanthenol (dash-dotted line).

The most remarkable differences are observed in the range from 4000 to 8000 cm^{-1}. It is relatively difficult to assign significant bands in the spectra completely and unambiguously as the overtones of O—H group and N—H group and their combinations may be responsible for several bands at 4500—5000 cm^{-1} and 6200—7200 cm^{-1}. The 4000—4500 cm^{-1} and 7000—7200 cm^{-1} bands can be assigned to combinations of C—H group overtones.
The most suitable calibration models for the determination of panthenol EE were obtained by PCR and PLS multivariate regression methods. The PCR and PLS models were constructed from the full NIR spectra (4000 experimental points) and three selected wavenumber ranges: the first one at 5200—5400 cm^{-1} (100 experimental points), the second at 6400—7200 cm^{-1} (400 experimental points) and the third at 4000—8000 cm^{-1} (2000 experimental points). The RMS %RE value of each model was calculated and used to select the spectral region where the best prediction of EE is reached.
Fig. 2 presents the RMS %RE values obtained for the EE prediction of D- and L-panthenol from PCR and PLS models. Based on these values, the wavenumber range with maximal recognition of enantiomers was selected. The lowest RMS %RE values for the enantiomers were obtained in the range of 6400—7200 cm^{-1} by both regression methods. Also, lower RMS %RE values indicate proper prediction of EE by PLS models compared to PCR regression in all cases.
Important characteristics of PCR and PLS calibration models (lower number of latent variables, higher sensitivity) and the figures of merit (Tab. 1) confirmed their suitability for EE determination in all selected spectral ranges. PCR and PLS models are more suitable for the prediction of the D-panthenol content than for the L-enantiomer in enantiomeric compositions.
Coefficients of determination of the calibration cross-validation and prediction are above 98 %, indicating acceptable prediction of EE by both calibration models. In case of PLS models, lower accuracy (RMSEs) values were obtained. Moreover, PLS models interpret higher % of concentration variance compared to PCR models. Likewise, calculated values of sensitivity and analytical sensitivity are in favor of PLS models.
The best PLS models were chosen from NIR spectral data in the range of 6400—7200 cm^{-1} for the determination of panthenol EE in pharmaceutical products.

UV/VIS spectrometry

The wavelength of maximum absorbance of panthenol derivatives is at λ_{max} = 525 nm. As it can be seen in Fig. 3, D-panthenol and the racemic mixture in water without β-CD show very similar absorbance.
However, after addition of β-CD to the solution, the absorbance of D-panthenol increased. Comparing individual absorbance, formation of inclusion complex of D-panthenol and β-CD is preferred as the absorbance increases proportionally with higher ratio of D-panthenol in the mixture.
The PCR and PLS calibration models were created from UV/VIS data measured in the wavelength range from 430 to 580 nm (150 experimental points). Characteristics of the calibration models and the selected figures of merit are presented in Tab. 2.

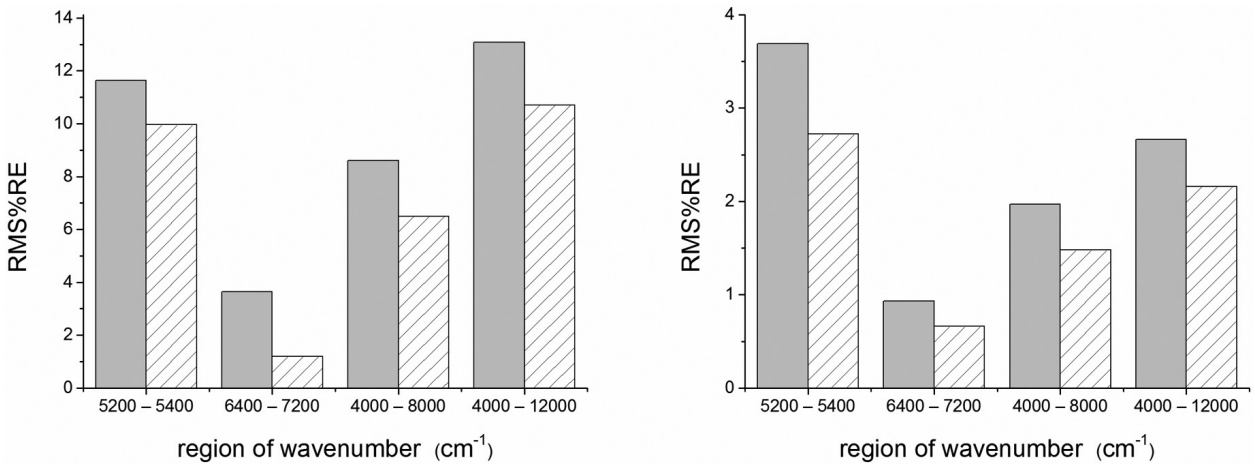

a) b)

Fig. 2. RMS %RE values for β-CD inclusion complexes with panthenol from PCR (A) and PLS (B) calibration models; D-panthenol (light gray), L-panthenol (cross-hatched).

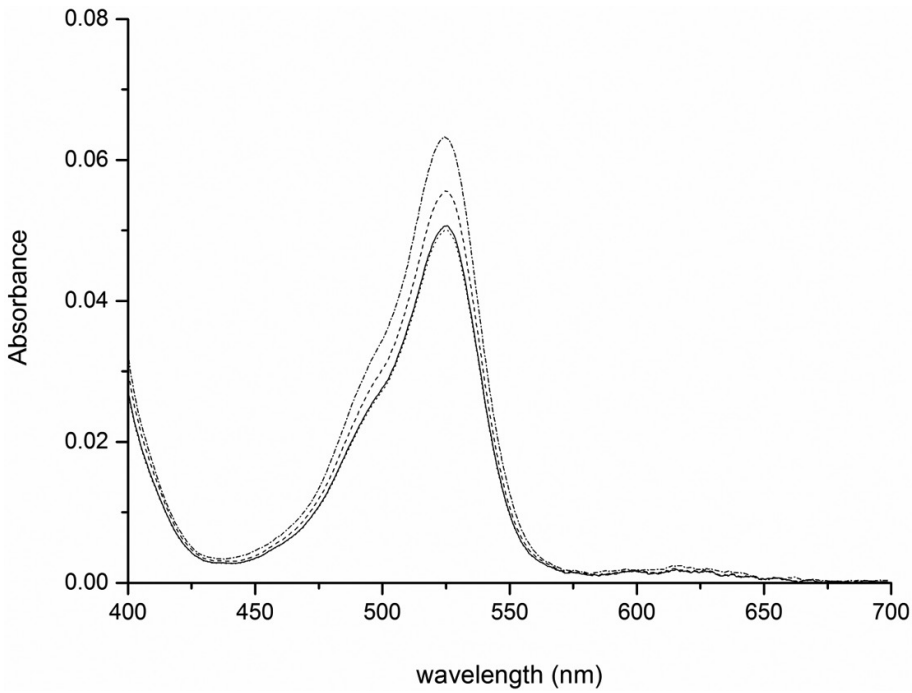

Fig. 3. UV/VIS spectra for panthenol racemic mixture (solid line), D-panthenol (dotted line) in water and inclusion complexes of β-CD with DL-panthenol (dashed line) and dexpanthenol (dash-dotted line).

The calibration models consist of three latent variables and explain more than 99 % of variance in the spectral data and over 93 % of the concentration variance. As for the PLS models, the coefficients of determination of calibration, cross-validation and prediction are closer to one; all these values are better compared to the PCR model. In addition, better values of the figure of merit were achieved by the PLS model, which were thus selected for UV/VIS spectrometry determination of panthenol EE in pharmaceutical products.

Tab. 1. The figure of merit and predicted values of PCR and PLS calibration models from NIR data for the determination of enantiomeric excess of panthenol.

		PCR		PLS	
		L	***D***	***L***	***D***
Number of latent variables		4	2	8	4
% of variance spectral block		99.61	99.17	99.87	99.83
% of variance concentration		88.85	84.85	97.01	98.07
	RMSEC[a]	1.252	1.633	0.463	0.990
Accuracy	RMSECV[b]	1.294	1.648	0.572	1.066
	RMSEP[c]	1.311	1.634	0.429	0.952
	RMS %RE[d]	1.263	2.458	1.178	1.214
Prediction bias		0.587	–1.462	–0.038	–1.214
R^2 Calibration		0.987	0.987	0.999	0.991
R^2 Cross-validation		0.988	0.992	0.988	0.989
R^2 Prediction		0.982	0.991	0.998	0.995
Sensitivity		2.60	6.86	0.38	2.19
Analytical sensitivity		2.81	1.89	0.66	1.21

[a]RMSEC — root mean square error of calibration,
[b]RMSECV — root mean square regression error of cross-validation,
[c]RMSEP — root mean square error of prediction,
[d]RMS %RE — root mean square percent relative error.

Tab. 2. The figure of merit and predicted values of PCR and PLS calibration models from UV/VIS data for the determination of panthenol enantiomeric excess in synthetic mixtures.

		PCR		PLS	
		L	*D*	*L*	*D*
Number of latent variables		3	3	3	3
% of variance spectral block		99.06	99.06	99.06	99.06
% of variance concentration		97.02	93.47	97.18	94.74
	RMSEC[a]	1.663	1.880	1.589	1.401
Accuracy	RMSECV[b]	1.591	1.754	1.584	1.462
	RMSEP[c]	1.784	1.822	1.543	1.406
	RMS %RE[d]	1.781	4.484	1.657	1.882
Prediction bias		–1.064	–1.154	–1.087	–1.485
R^2 Calibration		0.970	0.945	0.982	0.985
R^2 Cross-validation		0.949	0.911	0.977	0.987
R^2 Prediction		0.984	0.921	0.988	0.973
Sensitivity		6.45	1.48	4.27	1.13
Analytical sensitivity		3.65	0.33	2.59	0.61

[a]RMSEC — root mean square error of calibration,
[b]RMSECV — root mean square regression error of cross-validation,
[c]RMSEP — root mean square error of prediction,
[d]RMS %RE — root mean square percent relative error.

Analysis of pharmaceutical products

Tab. 3 presents the results of panthenol EE determination in tablets and eye drops of two producers. EE determination was realized by PLS models constructed from spectra acquired by NIR spectrometry in the wavenumber range of 6400—7200 cm^{-1} and those obtained from UV/VIS data measured in the wavelength range of 430—580 nm. Outcomes calculated by the PLS calibration model from the NIR spectra were in good agreement with those obtained by UV/VIS spectrometry.

Tab. 3. Enantiomeric excess of D-panthenol in pharmaceutical samples.

	EE of D-panthenol (%)	
samples	*NIR-PLS*	*UV/VIS-PLS*
tablets	98.25 ±1.32	97.95 ±1.01
eye drops 1	95.46 ±1.74	96.11 ±1.44
eye drops 2	95.71 ±1.48	95.99 ±1.25

Pharmaceutical samples, measured three times, were statistically evaluated on a 95 % confidence level ($\alpha = 0.05$) of the Fisher (F) test and two-sample t-test; p-values of the two-tailed F-test fall within the range of <0.11; 0.51>, indicating no significant differences between the variance values determined by NIR or UV/VIS spectrometry. Since p-values of the two-tailed t-test are in the interval of <0.25; 0.73>, it can be concluded that there is no significant difference in the results of the determination of EE in tablets and eye drops obtained by these spectrometric methods using multivariate PLS calibration.

Conclusion

In this paper, the possibility of using cheap and rapid methods based on NIR and UV/VIS spectrometry for panthenol EE determination in tablets and eyes drops is outlined. Inclusion complexes of panthenol with β-CD show small spectral differences and MVC methods, PCR and PLS, have to be used for the quantification of the relationship between the spectral data and the panthenol EE. Validation of the proposed methods was performed exploiting the model characteristics and the figure of merit. The PLS calibration models are preferred to the PCR ones for the determination of panthenol EE. Results of the two spectrometric methods were verified by the Student t-test and Fisher F-test. Both methods have been shown as promising in terms of the chiral analysis of pharmaceutical products where it is necessary to determine panthenol EE.

Acknowledgement

This work was supported by the Slovak Research and Development Agency under the contract No. APVV-15-0455. P.M. is grateful to the HPC center at the STU in Bratislava, which is a part of the Slovak Infrastructure of High Performance Computing (SIVVP project, ITMS

code 26230120002, funded by the European region development funds, ERDF), for the computational time and resources made available.

References

Abe I, Terada K, Nakahara T (2000) Biomed. Chromatogr. 14: 125–129.
Ebner F, Heller A, Rippke F, Tausch I (2002) Am. J. Clin. Dermatol. 3: 427–433.
Ferré J, Faber NM (2003) Chemometr Intell Lab Sys 69: 123–136.
Jeong HJ, Lee MH, Ro KW, Hur CW, Kim JW (1999) Int. J. Cosmet. Sci. 21: 41–50.
Hroboňová K, Lomenova A (2019) Chirality 32: 191–199.
Khater S, West C (2015) J. Pharm. Biomed. Anal. 102: 321–325.
König WA, Sturm U (1985) J. Chromatogr. 328: 357–361.
Mao X, Hu X, Pan W (2010) Chin. J. Chromatogr. 28: 1061–1066.
Okonkwo EN, Okeke JU, Nwabueze JC (2013) Bayero J. Pure Appl. Sci. 6: 27–31.
Poláček R, Májek P (2016) Chem. Listy 110: 18–25.
Takashi A, Hiroyasu M, Hiroshi O (1989) J. Chromatogr. A 474: 405–410.
Wise BM, Gallagher NB, Bro R, Shaver JM, Windig W, Koch RS (2007) PLS Toolbox 4.0, Eigenvector Research Inc., Wenatchee, USA.
Wold S, Sjostrom M, Eriksson L (2001) Chemometr Intell Lab Sys 58: 109–130.
Xie YM, Luo J, Tang XH, Yang D, Huo XF, Liu A, Hu X, Song X, Song H (2009) Chromatographia 69: 1025–1029.

sciendo

Impact of packing density on primary drying rate

Anna Matejčíková, Pavol Rajniak

Department of Chemical and Biochemical Engineering, Institute of Chemical and Environmental Engineering, Faculty of Chemical and Food Technology, Slovak University of Technology in Bratislava, Radlinského 9, 812 37 Bratislava, Slovakia
pavol.rajniak@stuba.sk

Abstract: This work aimed to determine the effect of packing density on the sublimation rate in a laboratory freeze dryer. Total amount of sublimed water was determined by gravimetric method while a total of seven experiments were performed under the same conditions (pressure, temperature, and drying time), at different configuration of the vials. The experiments confirmed that the higher the packing density, the lower the drying rate, and vice versa, the lower the packing density, the higher the drying rate. The effect of vials packing density was confirmed by experiments using a plastic rack, while the vials were separated and thus the packing density was lower. In this case, the drying rate was more homogeneous, which contributes to the higher quality of the final product.

Keywords: freeze-drying, gravimetric studies, lyophilization, packing density

Introduction

Freeze-drying, also known as lyophilization, is a commonly used process in the pharmaceutical, biomedical, and biotechnology industries. The main purpose of freeze-drying is preserving products and prolonging shelf-life stability while diminishing damages caused by sample drying. The process includes three main steps: (i) freezing of the solution to a frozen state when up to 95 % of water is frozen, (ii) primary drying, during which frozen water is removed by sublimation, and (iii) secondary drying to remove unfrozen water by desorption (Tang, 2004).

Although lyophilization is a well-known process, some misconceptions still persist, especially with the lyophilization of larger molecules. One of the issues is product heterogeneity throughout the batch, but also among different batches even at the same operating conditions. This problem has become the subject of various studies, and different sources of heterogeneities have been identified such as (i) the stochastic nature of nucleation, (iii) the edge vial effect, (iii) vial geometry heterogeneities, and (iv) the impact of excipients. Due to the concavity of the vials bottom, the vials dimension varies from vials to vials leading to differences in heat and mass transfer. However, this is a production limitation which cannot be affected and therefore it is not discussed. Also, the effect of excipients on batch heterogeneity is not discussed as it is not the subject of this study (Assegehegn et al., 2018; Hibler et al., 2012).

The freezing stage is an important step and plays a critical role in product quality and appearance. Freezing conditions (such as cooling rate, nucleation temperature, annealing, etc.) define the microstructure and affect both, drying rate and appearance of the final product. During the freezing step, nucleation occurs and due to its stochastic nature, nucleation temperature can vary by as much as 10 °C throughout the batch. Different nucleation temperatures lead to different crystal sizes and therefore, the quality of the final product varies (such as porous structure, product temperature and moisture content) (Assegehegn et al., 2018).

Also different position of vials is of importance. Vials situated along the periphery, termed as the edge vials, receive more heat compared to the central ones due to the heating from the walls. This phenomenon is denoted as edge vial effect. Also, it is important to note that edge vials are surrounded by a guard rail which also contributes to the edge vial effect (Rambhatla, 2003). In regard to the position of the vials, a critical factor is the degree of physical contact between the vials which is quantified by packing density and it is also a potential source of heterogeneity. The vial packing density was originally proposed by Placek (Placek, 2001). However, in this study, modified packing density expressed by the following equation is used:

$$\varnothing = \frac{A_{vials}}{A_{total}} \tag{1}$$

Where A_{total} represents the observed circle area with a certain radius from the monitored vial's center [m^2], and A_{vials} is the area occupied by vials in the observed area excluding the area of the monitored vial [m^2].

Vial configuration is closely related to packing density. In case of traditional close triangular pack-

ing, the vials are very close to each other and most vials have very high packing density. But due to the maximum space utilization, productivity is the highest. Daller and co-workers studied the impact of the lack of physical contact between vials as well as with the rack. They confirmed that using a rack system heat transfer can be controlled minimizing the edge vials effect. However, packing density was not evaluated in their work (Daller et al., 2020).

Materials and Methods

Equipment and Materials

A laboratory freeze-dryer Edwards Supermodulyo 12K Freeze Dryer equipped with two shelves was used; while only the first shelf was used for the studies. All vials (20R) with the external diameter of 29 mm were filled with 5 mL of distilled water and stoppered with 18 mm diameter stoppers.

Freeze-drying Procedure

All experiments were performed under the same conditions. First, vials were sequentially numbered and positioned in different arrangements on a stainless-steel tray and surrounded by a stainless-steel frame. During the experiment, the stainless-steel tray was removed so the vials were in direct contact with the shelf. Vials were filled with 5 mL of deionized water. The amount of sublimed water was determined gravimetrically, i.e. as the difference between the weights of the vial filled with deionized water before and after the sublimation. Gravimetric measurements belong to the simplest and, at the same time, the only methods providing detailed representation of the behavior of single vial and variability within the batch. For sublimation studies, sublimation of only 30 % of water is sufficient, otherwise, partial lack of thermal contact between ice and the vial wall may occur (Pikal et al., 1983). Sublimation tests were running as follows:

Holding system

Each experiment was performed using different vials configuration. Four experiments were performed without a holding system and three experiments were performed with a plastic stand as a holding system. For triangular packing, square packing, and packing with inactive vials, a traditional metal frame was used. For separated vials, three commercial plastic racks of 24.2 cm × 12.5 cm, with 6 × 3 bottomless holes of 3 cm diameter were used, while a fully loaded plastic rack held 54 vials (Fig. 1). The following vials configurations were used:

- **Triangular packing.** The first sublimation test was performed with a full packing (total 136 vials), while the vials were arranged in a close triangular configuration which is a traditional configuration in freeze-drying processes as it is the most efficient use of space.
- **Square packing** is an arrangement where the rows of spheres arranged in vertical and horizontal alignments form a square. Compared to triangular packing, the square full packing contains only 126 vials, so the overall process productivity decreases.
- **Inactive rows.** Vials are arranged in a close triangular packing; however, rows 7—10 are inactive.

Tab. 1. Freeze-drying cycle for sublimation studies.

Step	Time		Temperature [°C]		Vacuum [mbar]	
	Duration [min]	Total [hh:mm]	Set	Reach	Condenser	Chamber
Tempering	30	00:30	–5	–5.0	–	–
Loading	5	00:35	–5	–5.0	–	–
Freezing	40	00:40	–30	–5.0	–	–
Freezing	25	01:05	–30	–13.3	–	–
Freezing	22	01:27	–30	–22.7	–	–
Freezing	33	02:00	–30	–30.1	–	–
Freezing	40	02:40	–30	–30.3	–	–
Evacuation	30	03:10	–30	–30.3	0.8	0.8
Primary drying	5	03:15	–5	–30.0	0.8	0.8
Primary drying	25	03:40	–5	–10.9	1.0	1.0
Primary drying	30	04:10	–5	–5.2	1.0	1.0
Primary drying	240	08:10	–5	–4.8	0.9	0.9
Stoppering/Unloading	10	08.20	–	–	–	–

The ramp rate and the maximum allowable vacuum pressure were limited by the lyophilizer.

Vials are filled with water but full-stoppered so the sublimation does not occur.

- **Empty circle.** Another, traditional triangular packing is used with two inactive vials' circles. Vials are filled with water but full-stoppered. Both circles contain one active vial in the middle. Therefore it is possible to observe the behavior of two isolated vials. The first isolated vial is surrounded by a single circle of inactive vials, and the second lonely vial is surrounded by a double-inactive circle of vials.
- **A plastic stand** is a good tool to provide the same distance between the vials; however, productivity is relatively decreased. Using a plastic stand, three different arrangements of vials were used containing 54 vials, 27 vials, and 14 vials, respectively. To eliminate the radiation effect from the walls, the batch was surrounded by a polystyrene wall to ensure insulation.

Packing density

For each vial, two different packing density values were considered with respect to the size of the monitored area (Fig. 2). The first monitored area was a circle with the diameter twice that of a vial and the second monitored area was a circle with the diameter three times that of a vial, represented on Fig. 2 by vial 19 and 23, respectively. Circle segments were calculated using the AutoCAD.

For vial 19, packing density was calculated according to equation (1) as follows: the numerator expressing the area occupied by vials A_{vials} (area of monitored vial number 19 not included) was calculated as the sum of the section marked in blue; the denominator represents the total monitored area, i.e. it is calculated as the area of a circle with the diameter of 5.8 cm.

$$\varnothing_{19} = \frac{A_{vials}}{A_{total}} = \frac{6 \times A_{section}}{\pi \times 2.9^2} \tag{2}$$

Also, for vial 23, packing density was calculated according to equation (1) as follows: the numerator expressing the area occupied by vials A_{vials} (area of monitored vial number 23 not included) was calculated as the sum of section and e full circle marked in blue; the denominator represents the total monitored area, i.e. it is calculated as the area of a circle with the diameter of 8.7 cmr.

$$\varnothing_{23} = \frac{A_{vials}}{A_{total}} = \frac{6 \times A_{section} + 6 \times \frac{\pi \times 2.9^2}{4}}{\frac{\pi \times 9 \times 2.9^2}{4}} \tag{3}$$

a) b)

Fig. 1. Plastic rack used for sublimation studies, a) cross section, b) top side.

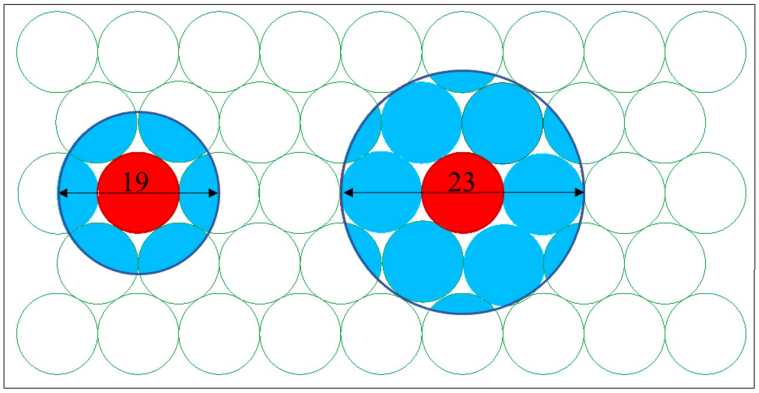

Fig. 2. Example of packing density calculation for vials marked in red, 19 and 23. In case of vial 19, the observed area is a circle with the diameter twice that of a vial. In case of vial 23, the observed area is a circle with the diameter three times larger than that of a vial.

Results and Discussion

Packing density evaluation

Packing density was evaluated according to equation (1) for each experiment. AutoCAD was used to determine the area of the sections. The packing density is not the same for all vials but it depends on the vial position. For triangular packing, vials can be classified into five groups according to their position as follow (Pisano et al., 2011):

a) Edge vials located in the corner of the shelf (also known as hot vials, pink color),
b) Edge vials in contact with the rail (orange and yellow color),
c) Edge vials without contact with the rail (light green color),
d) Central vials (dark green color).

Each group is characterized by different amount of water sublimed due to the different heat transfer coefficient. Vials with the same packing density should show a comparable amount of sublimed water. However, it must be remarked that although the dark green vials are the same color, the amount of sublimed water may vary over a wider range. In dark green vials which are in direct contact with hot vials (periphery vials), the amount of mass sublimed may be higher compared to the central vials. It was experimentally confirmed that the lower the packing density, the higher the amount of sublimed water.

Packing density values together with the amount of water sublimed are listed in Tab. 2. In some measurements, so-called outliers occurred, i.e. either too low or too high values that are outside the expected trend. These deviations can be caused by either excessive or insufficient closure of the stopper. Another reason for too low values can be insufficient contact between the vial and the shelf. To avoid including erroneous measurements, five maxima and five minima were identified and eventual outliers were disregarded. From the results follows that using a square packing arrangement can easily homogenize the batch as there are only three different values of packing density. Using square packing looks like a good compromise for reducing heterogeneity within a batch due to its simplicity (no inactive vials are required) not significantly affecting the productivity. Obviously, the packing density for all vials is zero when using a plastic stand, which has a significant effect on the homogenization of the amount of sublimed water. However, the use of a stand to separate the vials is disadvantageous due to the low amount of the final product.

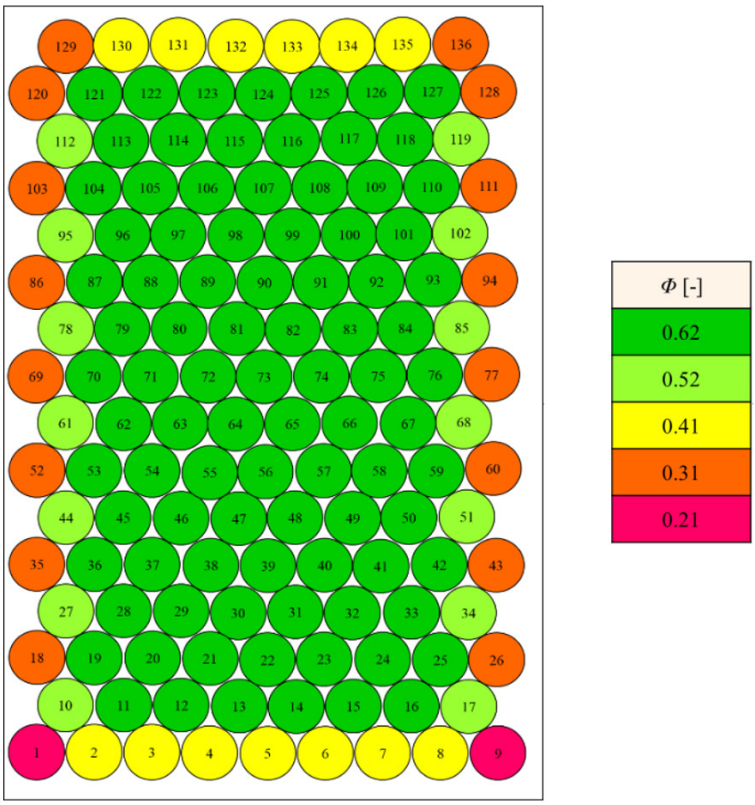

Fig. 3. Scheme of vial packing density classification as a function of their position in triangular packing. Values are different especially for the edge vials and central vials, which leads to different sublimation rates.

Tab. 2. Evaluation of packing density for each vial configuration. The lowest (Δm_{min}) and the highest (Δm_{max}) amount of sublimed water were evaluated for each packing density.

Packing denstiy 2D		
Φ [%]	Δm_{min} [g]	Δm_{max} [g]
Triangular packing		
62.10	0.99	1.79
51.75	1.18	1.78
41.40	1.33	2.14
31.05	1.56	2.05
20.70	1.79	2.21
Square packing		
48.10	1.10	2.37
35.21	1.26	2.11
23.19	1.80	2.25
Triangular packing – empty circle		
62.10	0.98	1.77
51.75	1.15	1.90
41.40	1.17	2.31
31.05	1.58	2.14
20.70	1.70	2.20
0.00	2.22	2.35
Triangular packing – empty rows		
62.10	1.74	2.31
51.75	1.97	2.14
41.40	2.00	2.59
31.05	2.29	2.66
20.70	2.61	2.77
Plastic stand – 54 vials		
0.00	2.06	2.68
Plastic stand – 27 vials		
0.00	2.68	3.13
Plastic stand – 14 vials		
0.00	3.25	3.47

Tab. 3. Comparison of the mass sublimed and homogeneity ratio in different configurations.

	Triangular Packing	Square Packing	Empty		Plastic Stand		
			Circles	Rows	54 vials	27 vials	14 vials
Δm_{min} [g]	0.99	1.10	0.98	1.74	2.06	2.68	3.25
Δm_{max} [g]	2.21	2.37	2.35	2.77	2.68	3.13	3.47
R	2.23	2.15	2.41	1.59	1.30	1.17	1.07

Inhomogeneity ratio

The amount of sublimed water is a good indicator of lyophilization inhomogeneity. To compare the heterogeneity of the batches, so-called inhomogeneity ratio expressed by the following equation is defined:

$$R = \frac{\Delta m_{max}}{\Delta m_{min}} \tag{4}$$

It follows from the above ratio that if the value approaches 1, the batch is homogeneous, and, conversely, the larger the ratio, the greater the difference between the minimum and maximum amount of sublimed water. The following table summarizes the values of the minimum and maximum amount of sublimed water as well as the inhomogeneity ratio for all measurements. The outliers were excluded, otherwise inhomogeneity ratio can be evaluated incorrectly (Tab. 3). The largest inhomogeneity ratio was determined for triangular packing. And vice-versa, the ratio approaches 1 if the packing density decreases, i.e. in experiments with plastic

stands. When using plastic stands with 14 vials, the batch can be considered as homogeneous.

Mapping of mass sublimed

The amount of water sublimed was evaluated by the gravimetric method. In the beginning, vials were filled with 5 mL of pure water, weighted without stoppers (m_1), and loaded into the drying chamber. This is followed by a freezing step and primary drying water sublimation according to the selected cycle. After approximately 30 % of the ice was sublimed, the sublimation was stopped, vials were unloaded and reweighted (m_2). The amount of sublimed water (Δm) was calculated as a difference between m_1 and m_2.

Figs. 4 and 5 show the amount of sublimed water during individual experiments in color. In these experiments, a metal frame was used. The lowest

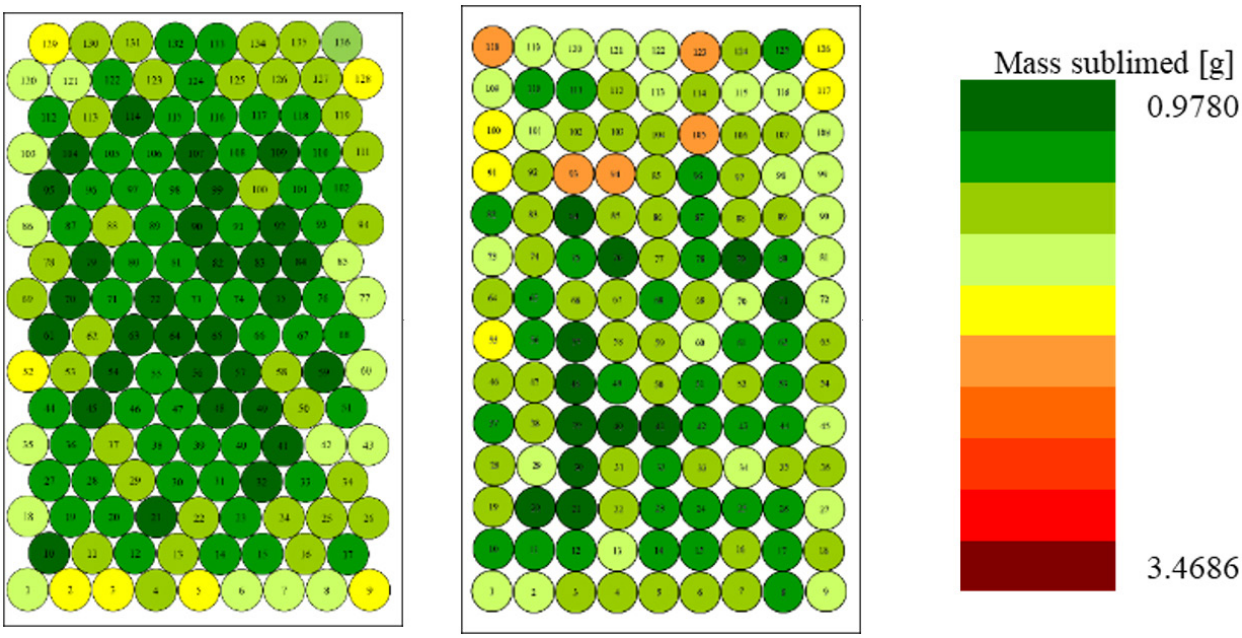

a) b)

Fig. 4. Effect of packing density with respect to vial arrangement. Two different full package configurations were used, (a) triangular packing (traditional approach), (b) square packing.

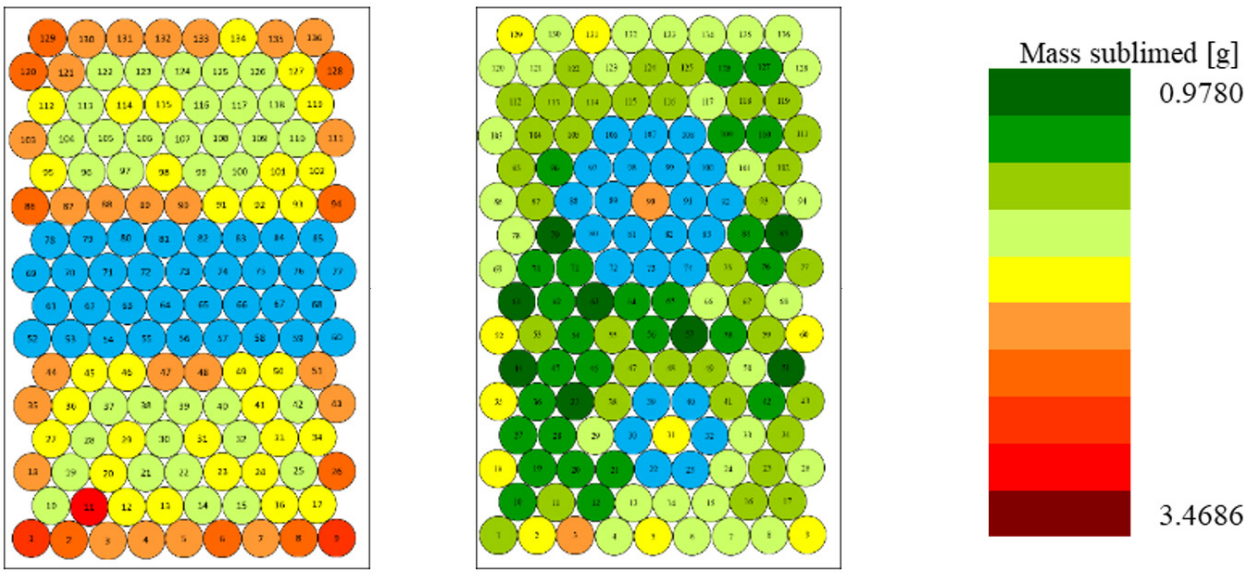

a) b)

Fig. 5. Effect of empty vials in a traditional triangular packing and of packing density with respect to vial arrangement. The effect of empty rows and the effect of empty circles were monitored.

amount of sublimed water was observed in vials marked with dark green color and, conversely, the highest amount of sublimed water was determined in vials marked with burgundy color. The blue vials were inactive and sublimation did not occur. When using a metal frame, the difference between the mass sublimed at periphery vs. central vials is significant. Mass sublimed in corner vial was as much as 2.23-fold higher compared to that in central vials. One possible explanation is that periphery vials are markedly heated from the walls and the primary drying rate is thus higher. Vice versa, the impact of walls is negligible in case of central vials due to the surrounding vials and sufficient distance from the walls.

Another explanation is the impact of packing density. Since the vials at the periphery have lower packing density and therefore lower competition, the primary drying rate is higher. In Figs. 4 and 5 it can be seen that in the vials located at the edge of the shelf, the amount of sublimed water is higher (marked from light green to orange-red) than in the middle of the shelf (dark green). It is also interesting to monitor the effect of inactive vials. In Fig. 5c), there are four rows of inactive vials that formally divide the batch into two parts. Since the vials located close to the inactive vials have no competitor, the packing density is lower and the sublimation is ultimately faster. Empty rows of vials are sometimes used in drugs manufacturing since they separate two different batches; however, these inactive vials cause inhomogeneity. Also, the impact of the empty circle was studied, Fig. 5d). In this case, it has been proved that even if the vial is in the middle of the shelf, it can be forced to behave like an edge vial just by surrounding it with inactive vials. It is obvious that if the vial has no competitors, i.e. low value of packing density, sublimation is faster. However, this arrangement was artificially created and is not practical to use.

To explain the impact of packing density, three experiments with a plastic rack were performed. Using a plastic rack, the vials are not in direct contact which results in higher sublimation rates.

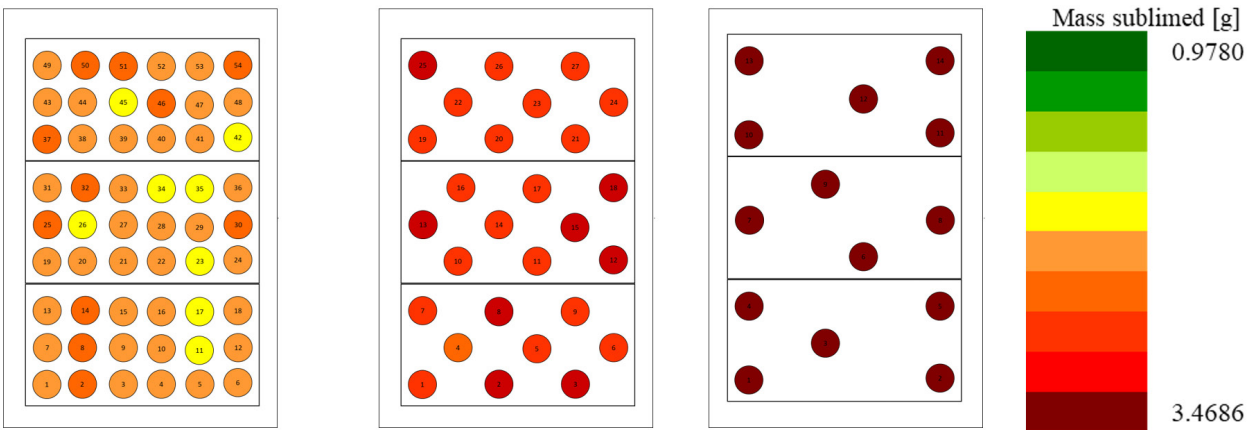

a) b) c)

Fig. 6. Comparison of total mass sublimed using plastic rack in three different configurations containing (a) 54 vials, (b) 27 vials, (c) 14 vials.

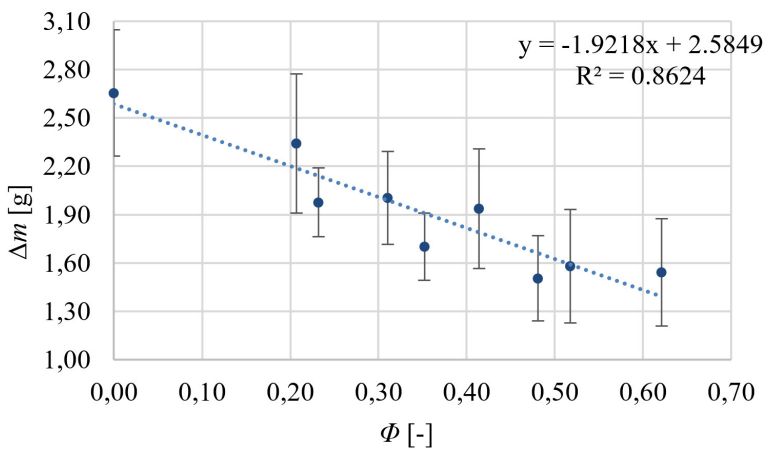

Fig. 7. Mass sublimed as a function of packing density including all measurements.

Where the vials are separated, heat transfer is reduced to the shelf-to-vial transfer without the competition of neighboring vials. If the packing density is low enough, central vials also behave as vials at the edge. In comparison with full packing, mass sublimed in corner vial was only 1.07-fold higher compared to the central vials and this batch can thus be considered homogenous (Fig. 6 c).

Finally, the effect of packing density on the amount of sublimed water is presented (Fig. 7). In this case, all measurements, including outliers, were taken into account. The results show that the highest rate of sublimation is reached at the packing density of 0, i.e. if the vial is not surrounded by other active vials. However, this is disadvantageous in terms of productivity, which would drop sharply. The aim is not to ensure the highest rate of sublimation, but the highest homogeneity of the batch. It is possible to achieve better homogeneity by employing square packing or arranging vials with the packing density value in a narrow range for all vials by adding several empty vials.

Conclusions

Packing density is an important parameter significantly affecting freeze-drying heterogeneity. Batch heterogeneity is important considering product quality or process scale-up. In our study, the impact of packing density on the sublimation rate was evaluated with respect to the vials arrangement and position. The effect of packing density is summarized as follows: (i) the lower the packing density, the higher the sublimation rate. Results confirmed that the amount of sublimed water at the packing density of 0 is up to 2.04-fold higher than at 0.77; (ii) sublimation rate is higher in the edge vials (also termed as "hot" vials) compared to the central vials, the difference can be as much as 1.8-fold; (iii) the vials with the same packing density value (using a plastic rack) show similar values of sublimed water and can be considered homogeneous within the measurement error. Lyophilization is an energy and time-consuming process (i.e. also expensive) and forcibly reducing the packing density is not advantageous due to productivity decline. Therefore, it is reasonable to consider square packing of vials, which ensures an increase in the homogeneity of the batch with only a slight decrease in the productivity. Nowadays, not all causes of freeze-drying heterogeneity are fully known and understood and therefore the research on this issue will continue.

Acknowledgment

This research was supported by the Grant Scheme to support excellent teams of young researchers under the conditions of the Slovak University of Technology in Bratislava.

References

Assegehegn G, Fuente EB, Franco JM, Gallegos C (2018) The importance of understanding the freezing step and its impact on freeze-drying process performance. Journal of Pharmaceutical Science. 108: 1378–1395.

Daller S, Friess W, Schroeder R (2020) Energy transfer in vials nested in a rack system during lyophilization. Pharmaceutics 12.

Hibler S, Wagner Ch, Gieseler F (2012) Vial freeze-drying, Part 1: New insights into heat transfer characteristics of tubing and molded vials. Journal of Pharmaceutical Sciences. 101: 1189–1201.

Pikal MJ, Roy ML, Shah S (1983) Mass and heat transfer in vial freeze-drying of pharmaceuticals: Role of the vial. Journal of Pharmaceutical Sciences. 73: 1224–1237.

Pisano R, Fissore D, Barresi AA (2011) Heat transfer in Freeze-Drying Apparatus. Developments in Heat Transfer.

Placek J (2001) Heat transfer limitations, their reduction and control. Proceed. Freeze-Drying Pharm Biologic, Breckenridge.

Rambhatla S, Pikal MJ (2003) Heat and mass transfer scale-up issues during freeze-drying, I: Atypical radiation and the edge vial effect. AAPS PharmSciTech 4(2).

Tang X, Pikal MJ (2004) Design of freeze-drying processes for pharmaceuticals: practical advice. Pharm. Res. 21: 191–200.

sciendo

Dimethyl sulfoxide as a strongly coordinating solvent: 3´,4´-dihydroxyflavone-Cu(II)-DMSO system case study

Miriama Šimunková, Michal Malček

Institute of Physical Chemistry and Chemical Physics, Faculty of Chemical and Food Technology, Slovak University of Technology in Bratislava, Radlinského 9, SK-812 37 Bratislava, Slovak Republic
miriama.simunkova@stuba.sk

Abstract: Dimethyl sulfoxide (DMSO) is an aprotic organic solvent widely used in laboratory practice due to its ability to dissolve both polar and nonpolar compounds. However, DMSO is also commonly known as a strongly coordinating solvent, especially towards transition metal containing complexes. In this study, estimation of the coordination ability of DMSO towards the Cu(II) ion was attempted, employing a model system composed of 3´,4´-dihydroxyflavone-Cu(II) complex in the presence of explicit DMSO molecules, using the density functional theory (DFT). Nature of the Cu-DMSO chemical interaction (i.e. Cu-O bonding) was studied within the framework of quantum theory of atoms in molecules (QTAIM). Impact of DMSO coordination on the charge and spin distribution at Cu(II) ion was inspected using Mulliken population and QTAIM analysis.

Keywords: coordination chemistry, Density Functional Theory, DMSO, QTAIM analysis, solvent effect

Introduction

Anhydrous dimethyl sulfoxide (DMSO) is an aprotic organic solvent widely used in laboratory practice, including important biochemical and biological experiments (Tashrifi et al., 2020; Psomas and Kessissoglou, 2013; Dorotíková et al., 2015; Simunkova et al., 2019; Misuri et al., 2017). It was first prepared by Alexander Saytzeff in 1867 using oxidation of dimethyl sulfide (Saytzeff, 1867). DMSO, an amphipathic molecule composed of a polar domain characterized by a sulfinyl and two nonpolar methyl groups, is able to solubilize a wide variety of polar and nonpolar compounds at high concentrations (De Abreu Costa et al., 2017; Tunçer et al., 2018). The DMSO-H_2O binary mixture (Sergievskii, Skorobogat'Ko, and Rudakov, 2010; Roy et al., 2011) is a common solvent in experiments involving cell cultures since a small amount of DMSO is well tolerated and does not change the culture viability (Allen et al., 2008; Singh and Ghosh, 2016). In addition, DMSO is well known as a strongly coordinating solvent (Levchenkov et al., 2014; Rancan and Armelao, 2015; Rancan et al., 2019; Patra et al., 2013). Highly polarized S═O double bond has positive and negative charges localized on sulfur and oxygen atoms, respectively (Cioslowski and Surján, 1992). This polarity of the S═O double bond is related to the high dielectric constant. With respect to the properties of the coordinated metal, DMSO can bind *via* either the sulfur or (sterically less hindered) oxygen atom. As reported by Calligaris, the S-bonding is essentially limited to the metal atoms of groups 8—10 (Calligaris, 1999). A decade ago, Díaz-Torres and Alvarez (Dıaz-Torres and Alvarez, 2011) attempted to quantify the coordinating character of a series of various solvents based on the probability to find the particular solvent coordinated in the presence of a transition metal. Their search was conducted in the Cambridge Structural Database (CSD), (Allen, 2002) and DMSO was found to be coordinated in 65 % of the searched cases (2038 structures in total) (Dıaz-Torres and Alvarez, 2011). Moreover, strong coordination of the DMSO solvent towards transition metals can lead to chemical changes in coordination compounds. For example, Patra et al. (Patra et al., 2013) revealed, using ^{1}H NMR spectroscopy, that Ru complexes with *N*-heterocyclic ligands readily undergo a ligand exchange reaction in DMSO. Recently, Rancan et al. (Rancan and Armelao, 2015; Rancan et al., 2019) pointed out that the use of DMSO affects the synthesis of coordination polymers by blocking some coordination sites. Aside the above mentioned coordination ability, the DMSO solvent can also act as a hydrogen bonding acceptor, as it was reported by Protti and coworkers (Protti et al., 2008).

In our previous studies (Jomová et al., 2019; Šimunková et al., 2020), antioxidant activity of flavonoid-Cu(II) complexes in the DMSO solvent was investigated. It is well known that biological activity of flavonoids can be significantly enhanced in the presence of transition metal ions (in this case cupric ion), forming complex compounds (Kumar and Pandey, 2013; Grazul and Budzisz, 2009; Samsonowicz and Regulska, 2017; Jomová et al., 2019). In general, study of antioxidant activity of flavonoids or other transition metal complexes is often limited by their poor solubility in most assays, thus the use of solvents such as DMSO is required (van Acker et al., 1996). However, strong coordination

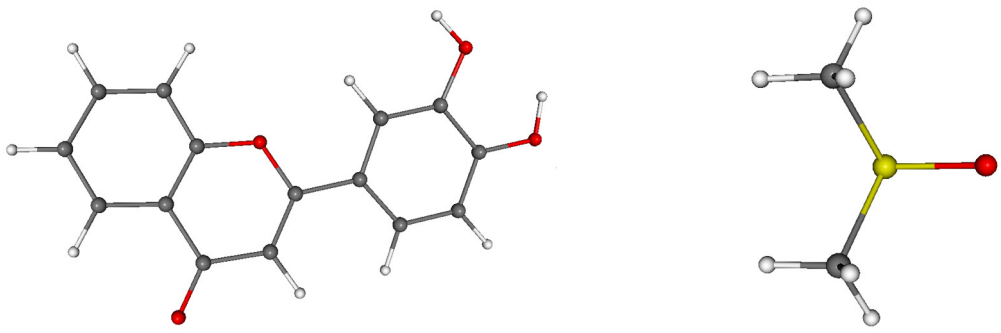

a) b)

Fig. 1. Scheme of B3LYP/6-311G* optimized DHF (a) and DMSO (b).

affinity of DMSO towards the Cu(II) ion (Rancan et al., 2019) is a problem. Gutmann donor number of DMSO, which is a measure of the strength of solvent as Lewis base, is 29.8 (Gutmann, 1978). For comparison, Gutmann donor numbers of methanol (MeOH) and H_2O are 19 and 18, respectively (Gutmann, 1978). To study the DMSO-Cu(II) coordination directly, inclusion of explicit solvent (DMSO) molecules in theoretical calculations is necessary. In this work, 3´,4´-dihydroxyflavone-Cu(II) complex in the DMSO solvent from our previous studies (Jomová et al., 2019) was used as a model system. 3´,4´-Dihydroxyflavone (DHF) is a polyphenolic compound containing a 2-phenyl-benzo-γ-pyrone moiety typical for flavonoids (Kumar and Pandey, 2013; Grazul and Budzisz, 2009; Jomová et al., 2019) (Figure 1a). For completeness, optimized structure of DMSO is shown in Figure 1b.

The paper is organized as follows: computational details are presented at first; then the Results section is subdivided into three parts, where optimized structures, charge density topologies, analysis of bond critical points and impact of coordinated DMSO molecules on the EPR parameters are discussed. At last, the main conclusions of this work are summarized.

Computational details

Model system DHF-Cu(II) was solvated with two and four molecules of DMSO. In all cases, the DHF-Cu(II) system containing protonated as well as deprotonated OH groups was considered. [Note that the deprotonation of OH groups of DHF is denoted with "–2H" superscript throughout the manuscript.] As a reference, Cu(II) ion solvated with two, four, five and six DMSO molecules was used. Additional reference systems, particularly Cu(II)-$n$$H_2O$ and Cu(II)-nMeOH (where n = 5, 6) complexes, were selected for comparison purposes only. Water and methanol act like donor solvents coordinating the Cu(II) ion via oxygen, i.e. in the same way as in case of DMSO. Geometry optimization of all studied systems was performed at the B3LYP (Becke, 1988; Lee, Yang, and Parr, 1988; Becke, 1993; Vosko, Wilk, and Nusair, 1980)/6-311G* (Krishnan et al., 1980; McLean and Chandler, 1980) level of theory in the Gaussian09 program package. (Frisch et al., 2009) The computational protocol used here (B3LYP/6-311G*) was chosen in accordance with our previously published results (Šimunková et al., 2020). In our previous study (Šimunková et al., 2020), the use of DFT functionals accounting for dispersion correction (particularly B3LYP-GD3 and B2PLYP) was reported to have only negligible effect on the geometries and energies of Cu(II)-flavonoid complexes compared to B3LYP. The energy-based criterion of SCF convergence was set to 10^{-8} Hartree. All systems were treated as doublets using the unrestricted Kohn-Sham formalism. Vibrational analysis was employed to confirm that the optimal geometries correspond to energy minima (i.e. absence of imaginary vibrations). Solvent effects of DMSO were treated via Polarizable Continuum solvent Model (PCM) (Miertus, Scrocco, and Tomasi, 1981; Tomasi, Mennucci, and Cammi, 2005) and Solvent Model based on Density (SMD) (Marenich, Cramer, and Truhlar, 2009) as implemented in the Gaussian09 package.

Quantum Theory of Atoms in Molecules (QTAIM) analysis (Bader, 1990), as implemented in the AIMAll package, (Keith, 2014) was applied for every system under study using the Gaussian09 formatted checkpoint files. QTAIM analysis was employed to evaluate charge populations at particular atoms and to estimate the character of interatomic interactions using properties in the bond critical points (BCP) and delocalization indexes (DI). Visualization of the calculated structures was performed using the Molekel software suite (Flükiger et al., 2002).

Results and Discussion

Structure of studied systems

Optimized geometries of all systems under study are shown in Figures 2 [DHF-Cu-*n*DMSO (n = 2, 4) complexes] and 3 [Cu-*n*DMSO (n = 2, 4, 5, 6) reference systems]. In case of DHF-Cu solvated with two DMSO molecules, the Cu(II) ion has a square planar coordination polyhedron with oxygens in the corners (Figures 2c and 2d). In case of DHF-Cu solvated with four DMSO molecules, the coordination polyhedron of Cu(II) is a Jahn-Teller distorted octahedron (Figures 2e and 2f). The main difference between the (protonated) DHF-Cu-4DMSO and the (deprotonated) $DHF^{(-2H)}$-Cu-4DMSO system is that the former has one OH group of DHF and one DMSO molecule in the axial positions while the latter contains two DMSO molecules in the axial positions. This can be clearly seen from the calculated Cu—O bond lengths of the above-mentioned systems. Optimized B3LYP/6-311G* Cu—O bond lengths of all the systems under study are presented in Table 1, including the reference Cu-*n*DMSO systems. As it can be seen from Figure 3 and Table 1, coordination polyhedron of Cu(II) in Cu-2DMSO, Cu-4DMSO, Cu-5DMSO, and Cu-6DMSO is linear, square planar, square pyramid, and Jahn-Teller distorted (elongated) octahedron as reported in Rancan et al. (Rancan and Armelao, 2015), respectively. For comparison, a scheme of the optimized Cu(II)-$n$$H_2O$ and Cu(II)-*n*MeOH (where n = 5, 6) complexes is shown in Figure S1 in Electronic Supplementary Material (ESI).

From the calculated Cu—O bond lengths presented in Table 1 follows that in fully protonated systems, Cu—O bonds between Cu and DMSO molecules are stronger (equatorial bonds being shorter than 2 Å) than those between Cu and DHF (equatorial bonds being longer than 2 Å). On the contrary, in case of deprotonated systems, Cu—O bonds between Cu

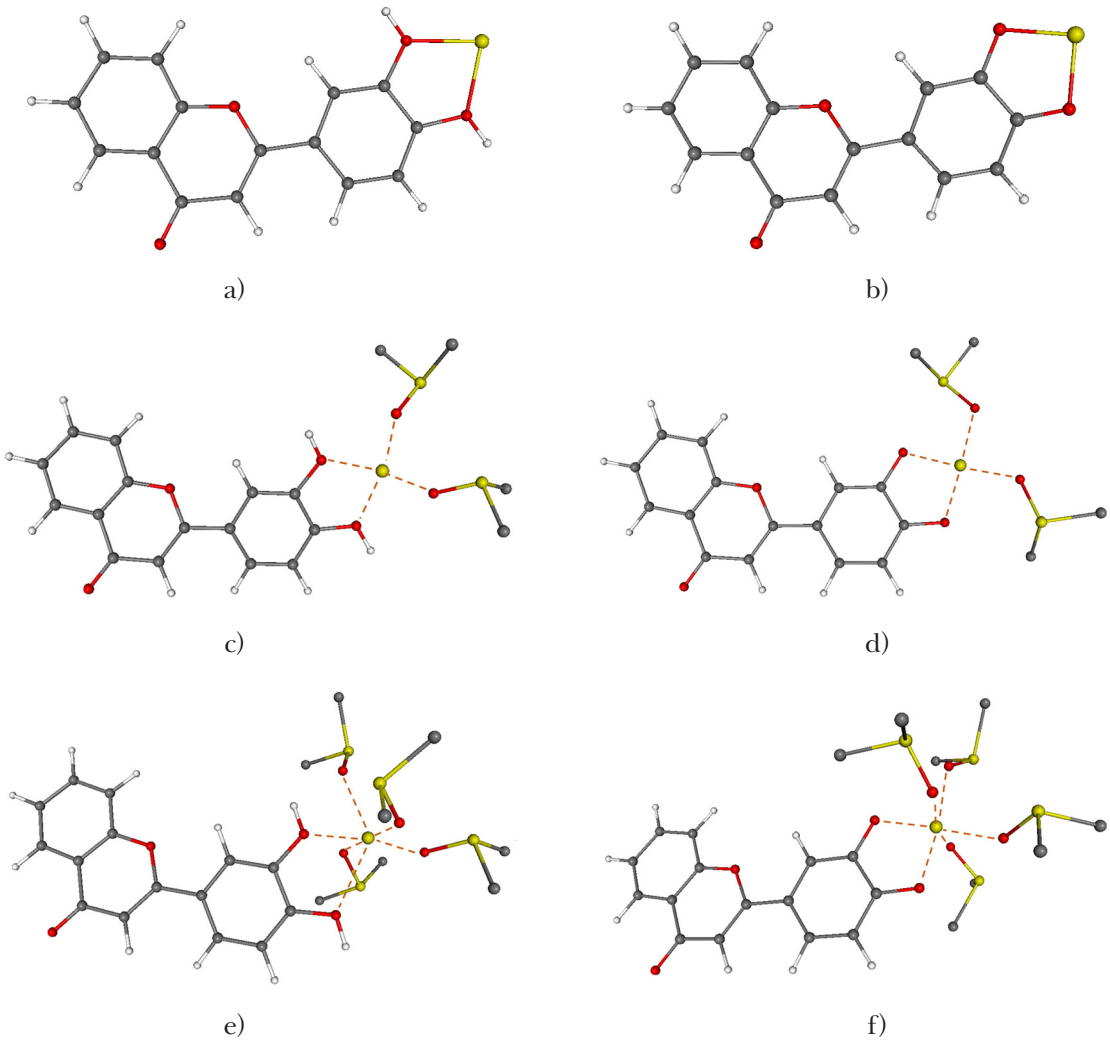

Fig. 2. Scheme of B3LYP/6-311G* optimized DHF-Cu-*n*DMSO systems: DHF-Cu (a), $DHF^{(-2H)}$-Cu (b), DHF-Cu-2DMSO (c), $DHF^{(-2H)}$-Cu-2DMSO (d), DHF-Cu-4DMSO (e), $DHF^{(-2H)}$-Cu-4DMSO (f). For simplicity, hydrogens of DMSO molecules are omitted.

and DHF are the stronger ones compared to the Cu-DMSO interaction. Obviously, the presence of O—H bonds weakens the binding capacity of DHF's oxygens towards the Cu(II) ion, leading to stronger interaction of Cu(II) with DMSO molecules. It is also noteworthy that all equatorial Cu—O bonds (either Cu—O^{DHF} or Cu—O^{DMSO}) in Table 1 have similar lengths in the interval of 1.9–2.1 Å. This finding points out that the coordination of DHF to Cu(II) is of similar strength than the one of DMSO to Cu(II). For comparison, equatorial Cu—O bond lengths in Cu-4DMSO, Cu-5DMSO and Cu-6MDSO are from the interval of 1.9–2.0 Å. [We do not consider the Cu-2DMSO system because it does not represent the DMSO solvation of the Cu(II) ion. These data are presented only for the sake of completeness.] Our calculated data are in agreement with the average Cu—O bond distances in metal sulfoxide complexes (2.03 Å) reported by Calligaris (Calligaris, 1999).

In addition, the two solvent models used (i.e. PCM (Miertus, Scrocco, and Tomasi, 1981; Tomasi, Mennucci, and Cammi, 2005) and SMD (Marenich, Cramer, and Truhlar, 2009)) were compared. Differences in the optimized Cu—O bond lengths using either PCM or SMD solvent model are less than 0.1 Å, hence they can be considered negligible. However, in case of calculating certain properties, such as solvatochromic shifts (Eilmes, 2014), reaction energy barriers (Miguel et al., 2016), or solvation free energies (Guerard and Arey, 2013), the choice of the solvent model can play a non-negligible role.

Charge density topology and QTAIM Cu-O bond characteristics

In the presented work, charge density topology of the studied systems was analyzed using the Mulliken population analysis (Mulliken, 1955) and the Bader's quantum theory of atoms in molecules (QTAIM) (Bader, 1990). Mulliken population analysis (as implemented in Gaussian09) is based on the Roothan's self-consistent field (SCF) LCAO-MO method (Roothaan, 1951), while Bader's QTAIM

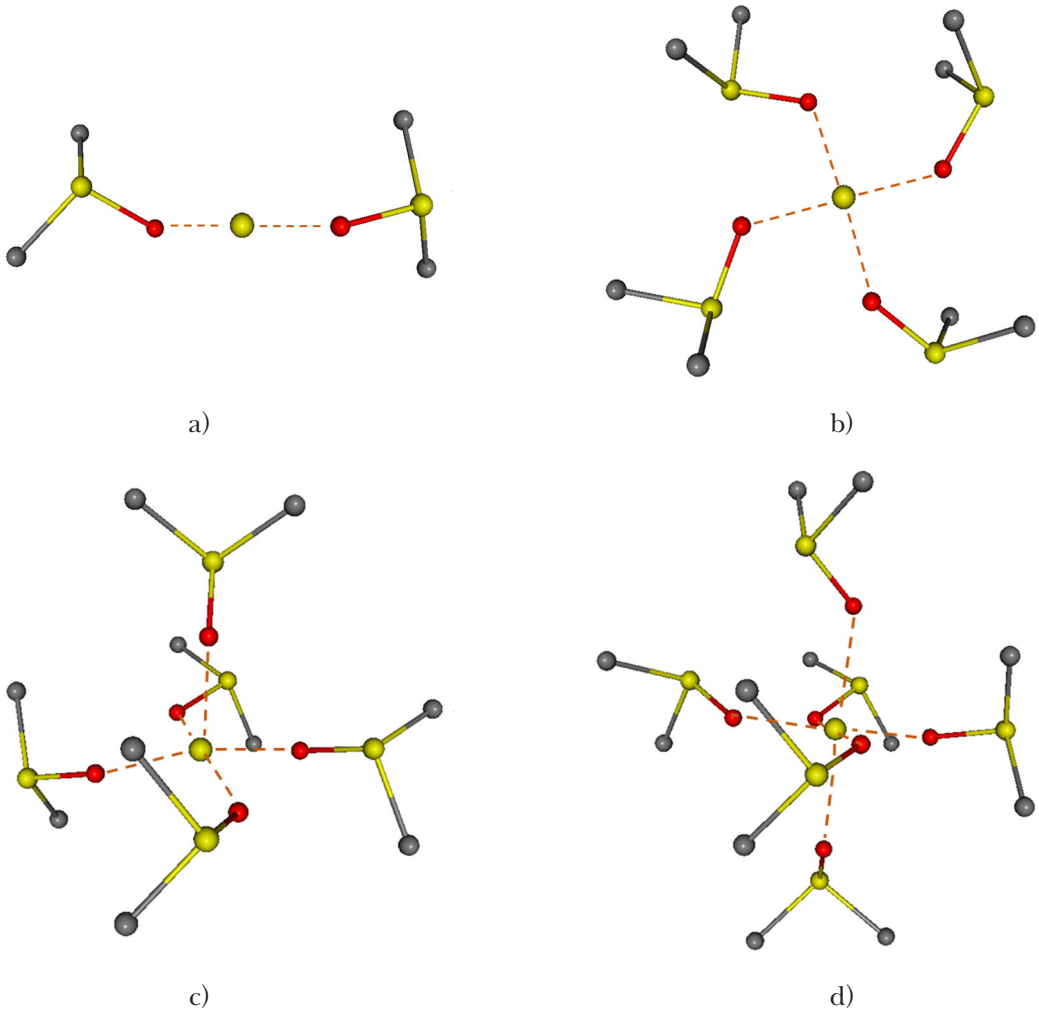

Fig. 3. Scheme of B3LYP/6-311G* optimized Cu-*n*DMSO reference systems; where $n = 2$ (a), $n = 4$ (b), $n = 5$ (c), $n = 6$ (d). For simplicity, hydrogens of DMSO molecules are omitted.

Tab. 1. Calculated B3LYP/6-311G* Cu—O bond lengths of the studied systems using two solvent models (PCM and SMD). Superscripts "E" or "A" stand for equatorial or axial O position, respectively.

System	Solvent model	d(Cu—O^{DHF})/Å	d(Cu—O^{DMSO})/Å
DHF-Cu	PCM	2.03[a], 2.03[a]	
	SMD	2.05, 2.06	
DHF$^{(-2H)}$-Cu	PCM	1.90, 1.89	
	SMD	1.90, 1.89	
DHF-Cu-2DMSO	PCM	2.01, 2.01	1.90, 1.89
	SMD	2.03, 2.03	1.91, 1.91
DHF$^{(-2H)}$-Cu-2DMSO	PCM	1.91, 1.92	1.96, 1.96
	SMD	1.92, 1.93	1.96, 1.97
DHF-Cu-4DMSO	PCM	2.10^{E}, 2.65^{A}	1.94^{E}, 1.95^{E}, 1.97^{E}2.28^{A}
	SMD	2.09^{E}, 2.74^{A}	1.94^{E}, 1.95, 1.96^{E}, 2.30^{A}
DHF$^{(-2H)}$-Cu-4DMSO	PCM	1.94^{E}, 1.96^{E}	2.01^{E}, 2.02^{E}, 2.48^{A}, 2.49^{A}
	SMD	1.95^{E}, 1.97^{E}	2.01^{E}, 2.02^{E}, 2.48^{A}, 2.48^{A}
Reference			
Cu-2DMSO	PCM		1.82, 1.82
	SMD		1.92, 1.93
Cu-4DMSO	PCM		1.94, 1.95, 1.95, 1.95
	SMD		1.95, 1.95, 1.96, 1.96
Cu-5DMSO	PCM		1.98^{E,a}, 1.98^{E,a}, 1.97^{E,a}, 1.98^{E,a}, 2.27^{A,a}
	SMD		1.98^{E}, 1.98^{E}, 1.98^{E}, 1.98^{E}, 2.26^{A}
Cu-6DMSO	PCM		1.98^{E,a}, 1.99^{E,a}, 2.00^{E,a}, 2.01^{E,a}, 2.38^{A,a}, 2.42^{A,a}
	SMD		1.99^{E}, 1.99^{E}, 2.01^{E}, 2.01^{E}, 2.37^{A}, 2.40^{A}

[a]B3LYP/6-311G*/PCM values from Šimunková et al. (Šimunková et al., 2020).

analysis is based on the decomposition of molecule into atomic domains (so-called basins) defined as zero-flux surfaces in the gradient vector field of electron density [$\nabla\rho(r)$]. Calculated Mulliken and QTAIM charges (q) at Cu(II), DHF, and DMSO moieties are presented in Table 2 which shows that both Mulliken and QTAIM partial charges at Cu are from the interval of 1.2—1.4 e. Charge transfer from the Cu(II) ion to the originally electroneutral moieties DHF and DMSO is nearly equivalent in fully protonated systems, i.e. partial charges at DHF and DMSO molecules are similar (around 0.2 e). On the other hand, in case of systems containing deprotonated DHF, charge transfer from Cu to the DHF$^{(-2H)}$ moiety is larger (around 0.5 e) than to the DMSO molecule (around 0.15 e). This result is in agreement with the above reported Cu—O bond lengths (see Table 1), i.e. weaker coordination of DMSO to Cu in the presence of deprotonated DHF than in the presence of protonated DHF.

Partial charges of DMSO molecules in all studied systems (naturally) decrease with respect to their increasing number, from around 0.3 e in Cu-2DMSO up to 0.15 or 0.05 e in Cu-6DMSO (equatorial or axial position, respectively) (Table 2). A similar decrease of charge transfer from DMSO to a metal atom (particularly Li) has been reported for $[Li(DMSO)_n]^+$ clusters (Sládek et al., 2011). Herein, the Mulliken population analysis did not provide correct nearly-equivalent values of the DMSO partial charges, *cf.* e.g. Mulliken q(DMSO) values of 0.26 and 0.17 e and QTAIM q(DMSO) values of 0.23 and 0.23 e for the DHF-Cu-2DMSO system.

Additional information about the character of chemical bonds can be obtained from the analysis of bond critical points (BCPs). Bader has described several types of critical points, among them BCP as a saddle point of electron density between two atoms forming a chemical bond (Bader, 1990). Nature (or strength) of the studied chemical bond can be estimated *via* properties in the BCP, such as charge density in BCP and its Laplacian. Another useful parameter is the delocalization index (DI) (Bader and Stephens, 1975) which provides a quantitative measure of electrons sharing between the two atoms (Fradera, Austen, and Bader, 1999). BCP charge densities (ρ_{BCP}), Laplacians ($\Delta\rho_{BCP}$) and DIs of Cu—O bonds in the studied systems are presented in Table 3.

BCP characteristics presented in Table 3 are in overall agreement with the optimized Cu—O bond lengths reported in the previous section. In case

Tab. 2. Mulliken and QTAIM charges (q) at Cu, DMSO and DHF moieties calculated at the B3LYP/6-311G*/PCM level of theory. Superscripts "E" or "A" indicate position (equatorial or axial, respectively) of the DMSO molecule.

System		q(DHF)/e	q(Cu)/e	q(DMSO)/e
DHF-Cu	Mulliken	0.72	1.28	
	QTAIM	0.74	1.26[a]	
DHF$^{(-2H)}$-Cu	Mulliken	−1.22	1.22	
	QTAIM	−1.19	1.19	
DHF-Cu-2DMSO	Mulliken	0.21	1.36	0.26, 0.17
	QTAIM	0.20	1.34	0.23, 0.23
DHF$^{(-2H)}$-Cu-2DMSO	Mulliken	−1.51	1.23	0.14, 0.14
	QTAIM	−1.52	1.25	0.14, 0.14
DHF-Cu-4DMSO	Mulliken	0.16	1.39	0.16^{E}, 0.16^{E}, 0.07^{E}, 0.06^{A}
	QTAIM	0.08	1.33	0.17^{E}, 0.18^{E}, 0.18^{E}, 0.08^{A}
DHF$^{(-2H)}$-Cu-4DMSO	Mulliken	−1.78	1.39	0.10^{E}, 0.11^{E}, 0.10^{A}, 0.09^{A}
	QTAIM	−1.56	1.29	0.11^{E}, 0.11^{E}, 0.03^{A}, 0.03^{A}
Reference				
Cu-2DMSO	Mulliken		1.36	0.36, 0.28
	QTAIM		1.39	0.30, 0.32
Cu-4DMSO	Mulliken		1.35	0.27, 0.24, 0.08, 0.06
	QTAIM		1.31	0.17, 0.18, 0.17, 0.17
Cu-5DMSO	Mulliken		1.38	0.13^{E}, 0.15^{E}, 0.15^{E}, 0.14^{E}, 0.06^{A}
	QTAIM		1.33	0.15^{E}, 0.16^{E}, 0.15^{E}, 0.16^{E}, 0.06^{A}
Cu-6DMSO	Mulliken		1.38	0.11^{E}, 0.14^{E}, 0.13^{E}, 0.13^{E}, 0.05^{A}, 0.07^{A}
	QTAIM		1.35	0.14^{E}, 0.15^{E}, 0.14^{E}, 0.14^{E}, 0.04^{A}, 0.05^{A}

[a]B3LYP/6-311G*/PCM values from Šimunková et al. (Šimunková et al., 2020).

Tab. 3. Calculated B3LYP/6-311G*/PCM QTAIM BCP characteristics (charge density ρ_{BCP}, Laplacian $\Delta\rho_{BCP}$ and delocalization index DI) of Cu—O bonds in the studied systems. Due to the similar nature (or length) of the particular equatorial or axial Cu—O bonds (Table 1), only average values are presented. Superscripts "E" or "A" stand for equatorial or axial O position, respectively, and superscripts "DHF" and "DMSO" indicate the O containing molecule (moiety).

System	ρ_{BCP}(Cu—O)/bohr^{-3}	$\Delta\rho_{BCP}$(Cu—O)/bohr^{-5}	DI(Cu—O)/–
DHF-Cu[a]	$0.07^{E, DHF}$	$0.37^{E, DHF}$	$0.35^{E, DHF}$
DHF$^{(-2H)}$-Cu	$0.10^{E, DHF}$	$0.54^{E, DHF}$	$0.62^{E, DHF}$
DHF-Cu-2DMSO	$0.07^{E, DHF}$, $0.10^{E, DMSO}$	$0.40^{E, DHF}$, $0.54^{E, DMSO}$	$0.32^{E, DHF}$, $0.52^{E, DMSO}$
DHF$^{(-2H)}$-Cu-2DMSO	$0.10^{E, DHF}$, $0.08^{E, DMSO}$	$0.50^{E, DHF}$, $0.45^{E, DMSO}$	$0.51^{E, DHF}$, $0.40^{E, DMSO}$
DHF-Cu-4DMSO	$0.06^{E, DHF}$, $0.02^{A, DHF}$ $0.08^{E, DMSO}$, $0.04^{A, DMSO}$	$0.29^{E, DHF}$, $0.07^{A, DHF}$ $0.46^{E, DMSO}$, $0.17^{A, DMSO}$	$0.26^{E, DHF}$, $0.07^{A, DHF}$ $0.42^{E, DMSO}$, $0.18^{A, DMSO}$
DHF$^{(-2H)}$-Cu-4DMSO	$0.09^{E, DHF}$ $0.07^{E, DMSO}$, $0.02^{A, DMSO}$	$0.45^{E, DHF}$ $0.38^{E, DMSO}$, $0.07^{A, DMSO}$	$0.46^{E, DHF}$ $0.34^{E, DMSO}$, $0.12^{A, DMSO}$
Reference			
Cu-2DMSO	0.12^{E}	0.68^{E}	0.62^{E}
Cu-4DMSO	0.08^{E}	0.46^{E}	0.42^{E}
Cu-5DMSO	0.08^{E}, 0.04^{A}	0.42^{E}, 0.17^{A}	0.39^{E}, 0.19^{A}
Cu-6DMSO	0.06^{E}, 0.03^{A}	0.33^{E}, 0.12^{A}	0.31^{E}, 0.14^{A}

[a]B3LYP/6-311G*/PCM values from Šimunková et al. (Šimunková et al. 2020).

of fully protonated systems, stronger interaction was found between Cu and DMSO compared to the Cu—DHF bond (ρ_{BCP} and DI values in Table 3). Such strong coordination can play a key role in ligand replacement reaction when studying various transition metal complexes as competitive reaction between a ligand and DMSO (Sudo et al., 2012). On the contrary, in systems containing deprotonated DHF moiety, the Cu—O bond between Cu and $DHF^{(-2H)}$ is stronger than that between Cu and the DMSO molecule/molecules. Coordination bonds formed between Cu and oxygens in the equatorial positions have DI values in the interval of 0.3–0.5 (Table 3), indicating a coordination bond equal in strength to nearly half of a single covalent bond (Fradera, Austen, and Bader, 1999). Bond interactions between Cu and oxygens in the axial positions are, naturally, significantly weaker (DI values below 0.2).

For comparison, BCP parameters and DI values of Cu-*n*DMSO systems are shown in Table 3 as well. These values are comparable to those for Cu-nH$_2$O and Cu-*n*MeOH (n = 5, 6) presented in Table S1. Thus, coordination of the Cu(II) ion with DMSO solvent can be assumed to be of similar nature as that of water or methanol molecules.

Impact of explicitly included DMSO molecules on spectroscopic parameters

As shown in the previous section, coordination of Cu with DMSO molecules affects the localization of charge density in the studied systems. Subsequently, such changes can possibly affect the properties directly derived from charge (or spin) density. For example, Almeida and Ramalho (de Almeida et al., 2011) reported the effect of explicitly included solvent molecules (pyridine, in particular) on the UV-Vis-NIR and EPR parameters of Cu(acac)$_2$ complex. Also, a comparison of EPR and UV-Vis spectra of DHF-Cu (molar ratio 1:2) system measured in DMSO (experiments taken from Jomová et al.[22]) and in MeOH (our results presented in Figure S2) prove the existence of such an effect. Stronger coordination of DHF to Cu(II) in MeOH compared to that in DMSO is documented by the higher absorbance band at 410 nm (see Figure S2a). In case of the EPR spectrum, only small changes were observed for the g-value but there is a non-negligible shift in the A-value of Cu(II) (115 Gauss in DMSO and 102 Gauss in MeOH, see Figure S2b). This is in agreement with the results of Almeida and Ramalho (de Almeida et al., 2011) who reported the hyperfine coupling constant to be more solvent-dependent than the g-tensor.

With respect to the above statement, the impact of explicit inclusion of DMSO molecules on the calculation of EPR parameters, particularly the hyperfine coupling constant, was studied. In the non-relativistic framework, the isotropic hyperfine coupling constant (HFC) is limited to the Fermi contact interaction. (Fermi, 1930). However, it has to be mentioned that, especially in case of heavy elements containing compounds, the inclusion of spin-orbit coupling contribution as well as the relativistic effects are crucial for proper treatment of the HFC constant (Malček et al., 2015; Malkin et al., 2006, 2011; Neese, 2003; Autschbach, 2014; Haase et al., 2018). However, for comparison purposes and

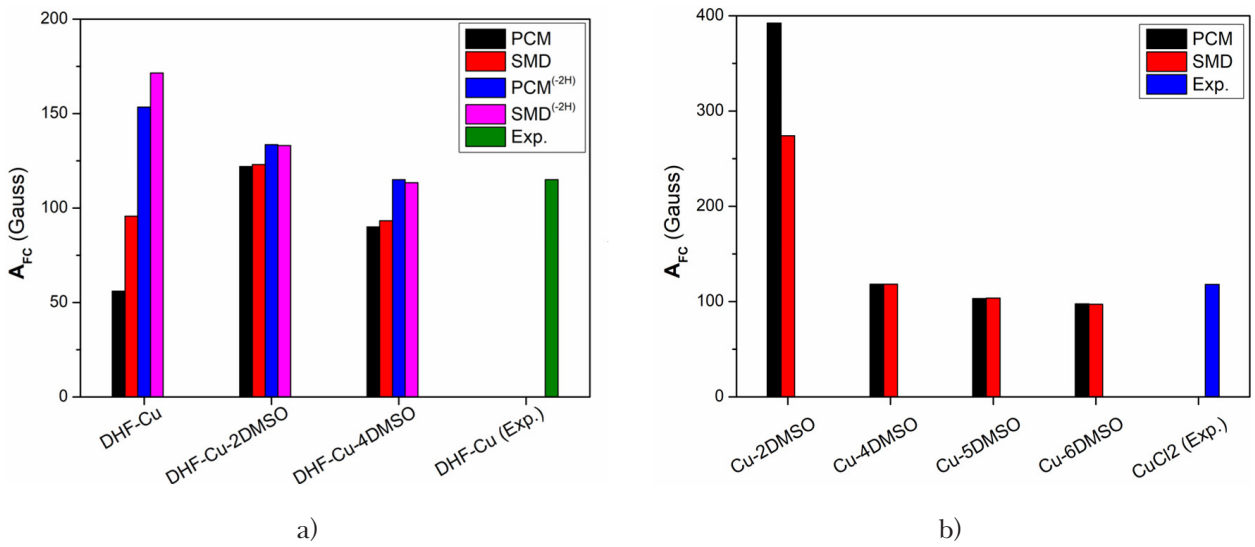

a) b)

Fig. 4. Comparison of calculated (non-relativistic B3LYP/6-311G*) and experimentally obtained isotropic Fermi contact coupling constants (A_{FC}) of Cu in the DHF-Cu-*n*DMSO (a) and Cu-*n*DMSO (b) systems. Superscript "–2H" indicates deprotonated DHF moiety. Experimental values are taken from Jomová et al. (Jomová et al., 2019).

for the sake of simplicity, only the non-relativistic limit of HFC (i.e. Fermi contact interaction) was considered here. A comparison of the calculated B3LYP/6-311G* non-relativistic and experimentally obtained (Jomová et al., 2019) isotropic Fermi contact coupling constants (A_{FC}) of the studied systems is shown in Figure 4. (Note that absolute A_{FC} values are presented even though the calculated A_{FC} values are negative, corresponding to the positive spin density at Cu.). As it can be seen from Figure 4a, inclusion of at least two explicit DMSO molecules into the DHF-Cu system significantly improves the agreement between the EPR experiment and theory. The inclusion of solvent model only (either PCM or SMD) into the DFT calculations is not sufficient to obtain qualitative agreement with the EPR experiment. If there are explicit DMSO molecules included, similar results are provided by the two different solvent models (PCM and SMD).

In case of Cu-*n*DMSO systems, an experimental A_{FC} value of $CuCl_2$ in DMSO (Jomová et al., 2019) was used as a reference because it basically represents the Cu(II) ion solvated with DMSO. As it was already mentioned in the previous sections, the Cu-2DMSO system is not robust enough to properly mimic the DMSO-solvated Cu(II) ion, see the overestimated A_{FC} value in Figure 4b. On the contrary, A_{FC} values of Cu-4DMSO, Cu-5DMSO and Cu-6DMSO are in quantitative agreement with the experimental A_{FC} values of $CuCl_2$ in DMSO (Jomová et al., 2019) (Figure 4b). Overall, the results presented in this section further confirm that the strong coordinating ability of the DMSO solvent plays a non-negligible role in the spectroscopic measurements, such as EPR in a frozen solution.

Conclusions

In the presented work, coordination ability of the DMSO solvent towards the Cu(II) ion was studied using model system DHF-Cu(II)-*n*DMSO (where n = 2, 4). The obtained results (calculated Cu—O bond lengths, BCP characteristics and DIs) have confirmed the strong coordination of the Cu(II) ion with DMSO molecules, similar to the interaction of Cu(II) with the DHF molecule (Jomová et al., 2019) or to the water-Cu coordination in Cu-5H_2O and Cu-6H_2O complexes (Malček et al., 2015). In case of fully protonated model system DHF-Cu(II)-*n*DMSO, interaction between the Cu and DMSO molecules is stronger than that between Cu and DHF, while in case of deprotonated system $DHF^{(-2H)}$-Cu(II)-*n*DMSO it is *vice versa*. Based on these results, a probability of ligand replacement in the DMSO solution of metal complexes can be assumed because DMSO can act as a competitive ligand. Moreover, it was shown that strong coordination of DMSO towards the Cu(II) ion can also affect the EPR spectroscopic parameters such as the Fermi contact coupling. In case of non-relativistic DFT calculations of the Fermi contact coupling constants, an inclusion of explicit DMSO molecules significantly improved the agreement between the EPR experiment and theory.

Supporting Information

Figure S1 Scheme of B3LYP/6-311G*/PCM optimized reference systems; where Cu(II)-5H_2O (a), Cu(II)-6H_2O (b), Cu(II)-5MeOH (c), Cu(II)-6MeOH (d).

Figure S2 **a)** Black line: UV-Vis spectrum of DHF dissolved in methanol, c = 1.10^{-3} M; blue line: UV-Vis spectra of DHF-Cu(II) (molar ratio = 2:1) system measured in methanol **b)** EPR spectrum of DHF-Cu(II) (molar ratio = 2:1) system dissolved in methanol measured at 120 K (experimental parameters: $g_{\perp}$ = 2,10 $g_{\parallel}$ = 2,42 $A_{\parallel}$ = 102 Gauss).

Table S1 Calculated B3LYP/6-311G*/PCM Cu—O bond lengths d, charge densities ρ_{BCP}, Laplacians $\Delta\rho_{BCP}$ and delocalization indexes DI of Cu(II)-*n*H_2O and Cu(II)-*n*MeOH systems (where n = 5, 6). Superscripts "E" or "A" stand for average values of equatorial or axial Cu—O bonds, respectively.

Table S2 Mulliken and QTAIM charges (q) at Cu, H_2O and MeOH moieties calculated at the B3LYP/6-311G*/PCM level of theory. Superscripts "E" or "A" indicate the position (equatorial or axial, respectively) of H_2O or MeOH molecules.

Acknowledgement

This work received financial support from the Slovak Grant Agencies APVV (contracts No. APVV-15-0079 and APVV-19-0087) and VEGA (contracts No. 1/0139/20, 1/0466/18 and 1/0482/20) and the Slovak University of Technology (Young Researcher Grant – FLAVMET, M. Šimunková and Excellent Team of Young Researchers CUSPK). MM is also grateful to the HPC center at the Slovak University of Technology in Bratislava, which is a part of the Slovak Infrastructure of High Performance Computing (SIVVP project, ITMS code 26230120002, funded by European region development funds) for the computational time and resources made available. To all financing sources the authors are greatly indebted.

Conflict of Interest: The authors declare that they have no conflict of interest.

References

Abreu CD, Ottoni MHG, Dos Santos MG et al. (2017) Molecules 22: 1—10.

Acker SABE van, de Groot MJ, van der Berg JD et al. (1996) Chem. Res. Toxicol. 9: 1305—1312.

Allen FH (2002) Acta Crystallographica Section B: Structural Science 58: 380–388.
Allen MJ, Boyce JP, Trentalange TM et al. (2008) Biotechnology and Bioengineering 100: 1193–1204.
Almeida de KJ, Ramalho TC, Rinkevicius R et al. (2011) J. Phys. Chem. A 115: 1331–1339.
Autschbach J (2014) Phil. Trans. R. Soc. A 372: 20120489.
Bader RFW (1990) Atoms in Molecules: A Quantum Theory. Oxford: Oxford University Press.
Bader RFW, Stephens ME (1975) J. Am. Chem. Soc. 97: 7391–7399.
Becke AD (1988) Phys. Rev. A 38: 3098–3100.
Becke AD (1993) The Journal of Chemical Physics 98: 5648–5652.
Calligaris M (1999) Croatica Chemica Acta 72: 147–169.
Cioslowski J, Surján PR (1992) Journal of Molecular Structure: THEOCHEM 255: 9–33.
Dıaz-Torres R, Alvarez S (2011) Dalton Transactions 40: 10742–10750.
Dorotíková S, Kožíšková J, Malček M et al. (2015) Journal of Inorganic Biochemistry 150: 160–73.
Eilmes A (2014) Theoretical Chemistry Accounts 133: 1538.
Fermi E (1930) Z. Phys. 60: 320.
Flükiger P, Lüthi HP, Portmann S, Weber J (2002) "'MOLEKEL 4.3.' Swiss Center for Scientific Computing: Manno, Switzerland.
Fradera X, Austen AM, Bader RFW (1999) J. Phys. Chem. A 103: 304–314.
Frisch MJ, Trucks GW, Schlegel HB, Scuseria GE et al. (2009) "Gaussian 09, Revision D.01." Gaussian, Inc., Wallingford CT.
Grazul M, Budzisz E (2009) Coord. Chem. Rev. 253: 2588–2598.
Guerard JJ, Arey JS (2013) Journal of Chemical Theory and Computation 9: 5046–5058.
Gutmann V (1978) The Donor-Acceptor Approach to Molecular Interactions. New York: Springer US.
Haase PAB, Repisky M, Komorovsky S et al. (2018) Chemistry – A European Journal 24: 5124–5133.
Jomová K, Hudecova L, Lauro P et al. (2019) Molecules 24: 4335.
Keith AT "AIMAll, Version 14.04.17; TK Gristmill Software: Overland Park, KS, 2014 (Aim.Tkgristmill.Com)."
Krishnan R, Binkley JS, Seeger R et al. (1980) J. Chem. Phys. 72: 650–654.
Kumar S, Pandey KA (2013) The Scientific World Journal, 162750.
Lee Ch, Yang W, Parr GR (1988) Phys. Rev. B 37: 785–789.
Levchenkov SI, Hcherbakov IN, Popov LD et al. (2014) Russian Journal of Coordination Chemistry 40: 523–530.
Malček M, Bučinský L, Valko M et al. (2015) Journal of Molecular Modeling 21: 237.
Malkin E, Malkin I, Malkina OL et al. (2006) Phys. Chem. Chem. Phys. 8: 4079–4085.
Malkin E, Repiský M, Komorovský S et al. (2011) Journal of Chemical Physics 134: 044111.
Marenich VA, Cramer ChJ, Truhlar DG (2009) Journal of Physical Chemistry B 113: 6378–6396.
McLean AD, Chandler GS (1980) J. Chem. Phys. 72: 5639–5648.
Miertus S, Scrocco E, Tomasi J (1981) Chem. Phys. 55: 117–129.
Miguel ELM, Santos CIL, Silva CM et al. (2016) Journal of the Brazilian Chemical Society 27: 2055–2061.
Misuri L, Cappiello M, Balestri F et al. (2017) Journal of Enzyme Inhibition and Medicinal Chemistry 32: 1152–1158.
Mulliken RS (1955) The Journal of Chemical Physics 23: 1833.
Neese F (2003) J. Chem. Phys. 118: 3939–3948.
Patra M, Pierroz VA et al. (2013) Chemistry – A European Journal 19: 14768–14772.
Protti S, Mezzetti A, Cornard JP et al. (2008) Chemical Physics Letters 467: 88–93.
Psomas G, Kessissoglou DP (2013) Dalton Transactions 42: 6252–6276.
Rancan M, Armelao L (2015) Chemical Communications 51: 12947–12949.
Rancan M, Carlotto A, Bottaro G et al. (2019) Inorganics 7: 103.
Roothaan CCJ (1951) Reviews of Modern Physics 23: 69–89.
Roy S, Banerjee S, Biyani N (2011) Journal of Physical Chemistry B 115: 685–692.
Samsonowicz M, Regulska E (2017) Spectrochimica Acta Part A : Molecular and Biomolecular Spectroscopy 173: 757–771.
Saytzeff A (1867) Ann Der Chem Und Pharm 144: 148–156.
Sergievskii VV, Skorobogat'Ko DO, Rudakov AM (2010) Russian Journal of Physical Chemistry A 84: 350–355.
Šimunkova M, Lauro P, Jomova K et al. (2019) Journal of Inorganic Biochemistry 194: 97–113.
Šimunková M, Valko M, Bučinský L et al. (2020) J. Mol. Struct. 1222: 128923.
Singh Y, Ghosh T (2016) Talanta 148: 257–263.
Sládek V, Lukeš V, Breza M (2011) Computational and Theoretical Chemistry 963: 503–509.
Sudo R, Yoshioka D, Mikuriya M et al. (2012) X-Ray Structure Analysis Online 28: 71–72.
Tashrifi Z, Khanaposhtani MM, Larijani B et al. (2020) Advanced Synthesis and Catalysis 362: 65–86.
Tomasi J, Mennucci B, Cammi R (2005) Chem. Rev. 105: 2999–3093.
Tunçer S, Gurbanov R, Sheraj I et al. (2018) Scientific Reports 8: 14828.
Vosko SH, Wilk Nusair M (1980) Canadian Journal of Physics 58: 1200–1211.

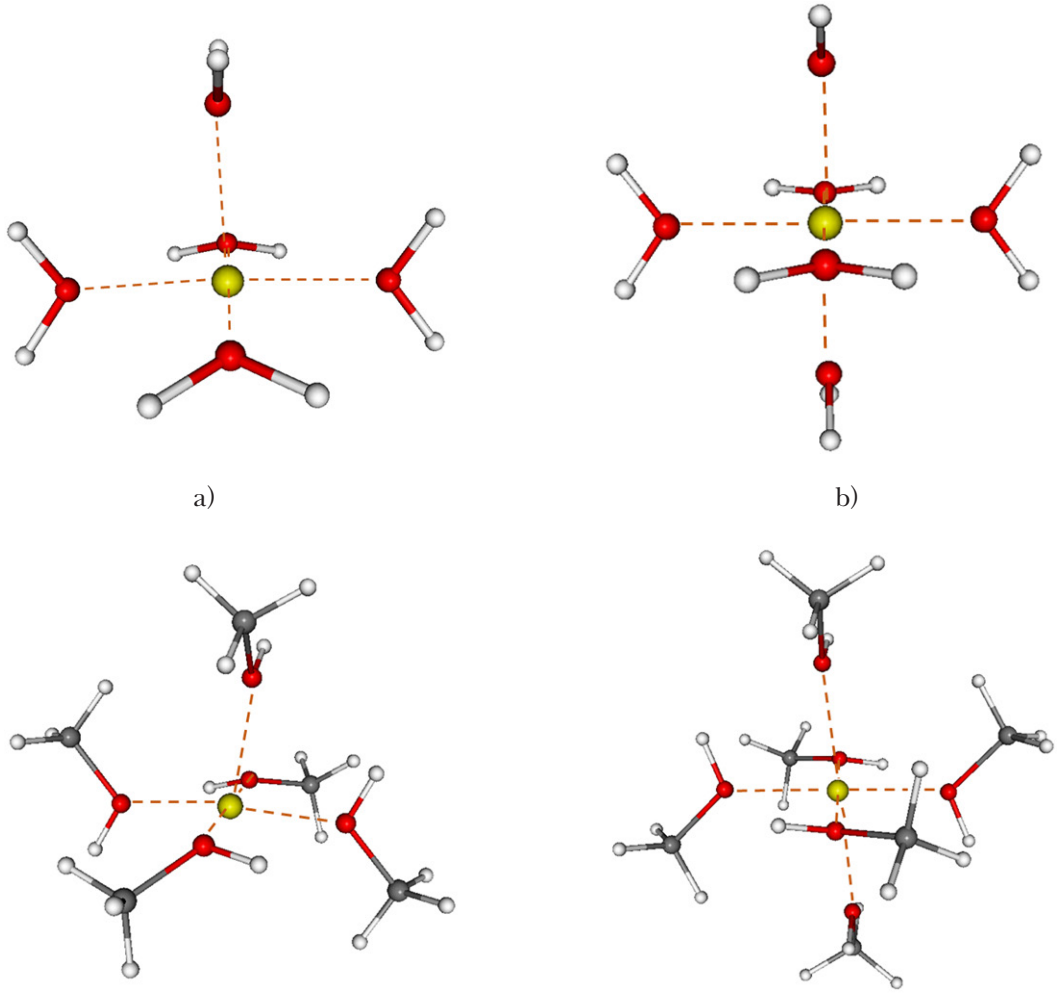

Fig. S1 Scheme of B3LYP/6-311G*/PCM optimized reference systems: Cu(II)-5H_2O (a), Cu(II)-6H_2O (b), Cu(II)-5MeOH (c), Cu(II)-6MeOH (d).

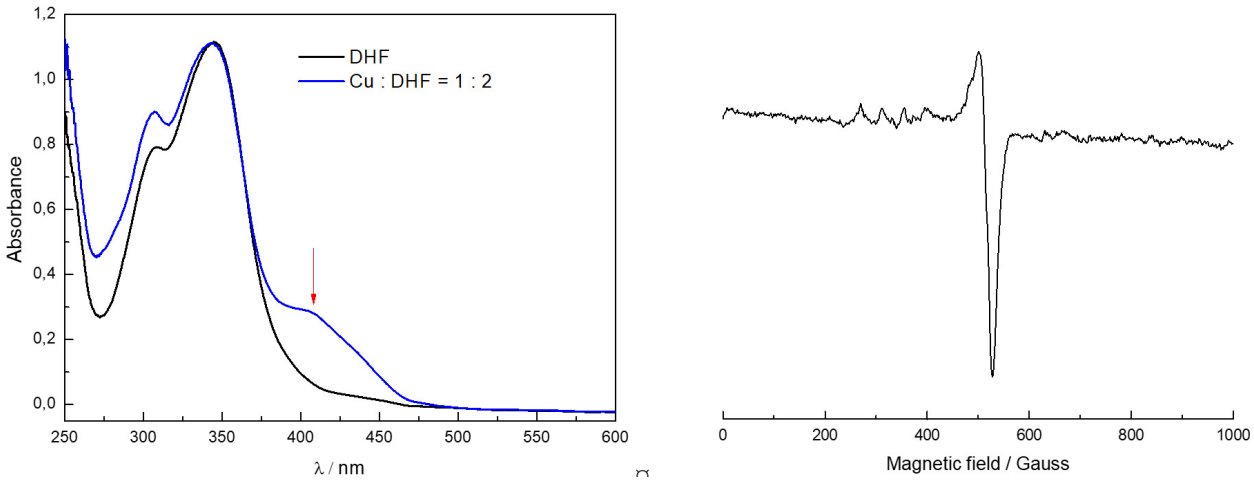

Fig. S2 a) Black line: UV-Vis spectrum of DHF dissolved in methanol, c = 1.10^{-3} M; blue line: UV-Vis spectra of DHF-Cu(II) (molar ratio = 2:1) system measured in methanol **b)** EPR spectrum of DHF-Cu(II) (molar ratio = 2:1) system dissolved in methanol measured at 120 K (experimental parameters: $g_{\perp}$ = 2,10 $g_{\parallel}$ = 2,42 $A_{\parallel}$ = 102 Gauss).

Tab. S1. Calculated B3LYP/6-311G*/PCM Cu—O bond lengths (*d*), charge densities (ρ_{BCP}), Laplacians ($\Delta\rho_{BCP}$) and delocalization indexes (DI) of Cu(II)-$n$$H_2O$ and Cu(II)-nMeOH systems (where n = 5, 6). Superscripts "E" or "A" stand for average values of equatorial or axial Cu—O bonds, respectively.

System	*d*/Å	ρ_{BCP}/bohr^{-3}	$\Delta\rho_{BCP}$/bohr^{-5}	DI/–
Cu-5H_2O	1.97^E	0.08^E	0.46^E	0.37^E
	2.18^A	0.05^A	0.24^A	0.21^A
Cu-6H_2O	1.99^E	0.07^E	0.43^E	0.34^E
	2.22^A	0.05^A	0.21^A	0.19^A
Cu-5MeOH	1.98^E	0.08^E	0.44^E	0.37^E
	2.22^A	0.05^A	0.20^A	0.19^A
Cu-6MeOH	2.00^E	0.07^E	0.41^E	0.35^E
	2.27^A	0.04^A	0.17^A	0.17^A

Tab. S2. Mulliken and QTAIM charges (*q*) at Cu, H_2O and MeOH moieties calculated at the B3LYP/6-311G*/PCM level of theory. Superscripts "E" or "A" indicate the position (equatorial or axial, respectively) of the H_2O or MeOH molecules.

System		*q*(Cu)/*e*	*q*(solvent)^E/*e*	*q*(solvent)^A/*e*
Cu-5H_2O	Mulliken	1.51	0.11	0.06
	QTAIM	1.43	0.12	0.05
Cu-6H_2O	Mulliken	1.56	0.09	0.04
	QTAIM	1.45	0.11	0.05
Cu-5MeOH	Mulliken	1.47	0.12	0.04
	QTAIM	1.40	0.14	0.05
Cu-6MeOH	Mulliken	1.56	0.09	0.04
	QTAIM	1.40	0.12	0.05

sciendo

Inhibition of staphylococci and *S. aureus* in wastewater by ferrates and electrochemical methods

Alžbeta Medveďová[1], Stanislava Kecskesová[2], Anna Krivjanska[2], Marian Vojs[3], Marián Marton[3], Jan Filip[4], Miroslav Fehér[2], Tomáš Mackuľak[2]

[1]*Department of Nutrition and Food Quality Assessment, Faculty of Chemical and Food Technology, Slovak University of Technology, Radlinského 9, 812 37 Bratislava, Slovakia*
[2]*Institute of Chemical and Environmental Engineering, Faculty of Chemical and Food Technology, Slovak University of Technology, Radlinského 9, 812 37 Bratislava, Slovakia*
[3]*Institute of Electronics and Photonics, Faculty of Electrical Engineering and Information Technology, Slovak University of Technology, Ilkovičova 3, 812 19 Bratislava, Slovakia*
[4]*Regional Centre of Advanced Technologies and Materials, Departments of Physical Chemistry and Experimental Physics, Faculty of Science, Palacký University in Olomouc, Šlechtitelů 27, 78371 Olomouc, Czech Republic*
tomas.mackulak@stuba.sk

Abstract: Increasing concentration of antibiotics in environment and their subinhibitory concentrations in wastewater may result in increased antibiotic resistance of present bacteria. Therefore, this study was aimed to analyze the efficiency of coagulase-positive staphylococci and *Staphylococcus aureus* inhibition in wastewater by electrochemical methods and addition of ferrates. Advanced electrochemical oxidation by boron doped diamond electrodes in anode; cathode and anode-cathode connection were used for wastewater disinfection. Results showed that the most effective connection was the anodic one, as complete inhibition of coagulase-positive staphylococci as well as of *S. aureus* was observed after 40 min. Energy consumption was 3.69 kWh/m^3 for effluent wastewater disinfection. The second studied method of wastewater disinfection was the application of powdered ferrates. Addition of 100 mg of ferrates resulted in the inhibition of 84—96 % of coagulase-positive staphylococci and 97—99 % of *S. aureus* in influent water, while the inhibition of coagulase-positive staphylococci and *S. aureus* was 61—83 % and 83—86 %, respectively, in effluent wastewater.

Keywords: BDD electrode, coagulase-positive staphylococci, disinfection, ferrates, municipal wastewater, Staphylococcus aureus

Introduction

The presence of pharmaceuticals, illicit drugs, hormones or other micropollutants and their metabolites can have negative effect on water animals, plants and microorganisms (Brodin et al., 2013; Le at al., 2014; Mackuľak et al., 2015a, 2015b; Nuel et al., 2018; Wilkinson et al., 2018). Besides these micropollutants, the presence of antibiotic resistant bacteria and genes encoding this resistance is monitored in wastewater (Novo et al., 2013; Birošová et al., 2014). Elimination efficiency of bacteria and micropollutants at Wastewater Treatment Plants (WWTPs) is limited and therefore many recent works are focused on the removal of these contaminants (Kümmerer, 2009; Mackuľak et al., 2015b; Michael-Kordatou et al., 2018; Nuel et al., 2018).

The presence of pathogenic and potentially pathogenic bacteria is of particular concern. While some bacteria are mainly nosocomial, some are community-acquired, including coagulase-positive staphylococci and *Staphylococcus aureus*. Staphylococci frequently colonize the nasal vestibule and skin of about 10—50 % of asymptomatic humans (ECDC, 2017). Moreover, pathogenic *S. aureus* is regarded as a "superbug" due to its huge capacity to be resistant to a wide range of antibiotics, e.g. *S. aureus* strains resistant to methicillin (MRSA) or vancomycin (VISA/VRSA) and to many other antibiotics. These strains represent an urgent global problem since the mortality of *S. aureus* bacteremia remains approximately 20—40 % despite the availability of effective antimicrobials (Mylotte et al., 1987; ECDC, 2017). In community, *S. aureus* can be easily transferred from carriers or infected persons via direct contact and specific carriers (Stepanović et al., 2008) as it can survive in different environments, including wastewater.

Nowadays, many scientific studies deal with chemical and biological elimination of micropollutants such as X-ray substances, antibiotics, psychoactive pharmaceuticals, drugs and resistant types of microorganisms in municipal wastewater (Golovko et al., 2014; Mackuľak et al., 2015a; Verlicchi and Zambello, 2015; Iakovides et al., 2019; Kulandaivelu et al., 2019). Wastewater from point sources, e.g. health care institutions, are intensively studied to find biological and chemical methods for wastewater treatment such as membrane bioreactors, Fenton reaction, ozonization, heteroge-

neous catalysis, boron-doped diamond electrodes (BDDE), application of ferrates etc. (Verlicchi and Zambello, 2015; Mackuľak et al., 2015a, 2015b, 2016; Michael-Kordatou et al., 2018; Kulandaivelu et al., 2019). These techniques show significant degradation of various groups of pharmaceuticals and illegal drugs. These processes produce radicals efficiently eliminating multidrug-resistant microorganisms (Michael-Kordatou et al., 2018; Yuan et al., 2013). Furthermore, it is possible to combine these methods with the original ones. A good example is shown in the study by Kajitvichyanukul and Suntronvipart (2006), where the photoFenton reaction was combined with biological treatment. Application of BDDE is one of the most promising techniques; however, the research is still insufficient. Therefore, this study deals with monitoring of coagulase-positive staphylococci and *S. aureus* in wastewater from Slovak WWTPs and the possibility of using ferrates and boron doped diamond electrodes application as disinfection methods.

Material and methods

Wastewater sampling

In this study, wastewater from Petržalka WWTP was used. Samples from influent and effluent of Petržalka WWTP were taken on 14. 9. 2015 and 14. 1. 2016 during 24 hours by an automatic sampler at the entry into the WWTP mechanical stage (Mackuľak et al., 2015a, 2015b). WWTP Petržalka treats wastewater from the largest housing estate in Bratislava as well as wastewater from health care facilities with about 2 000 hospital beds. The WWTP is designed to treat wastewater from 200 000 p.e. (population equivalent) and contains a mechanical pre-treatment stage for raw wastewater and a biological treatment stage, which is designed as RADN (based on the ongoing processes — regeneration, anaerobia, denitrification and nitrification). The produced sludge is digested and produced biogas energy is recovered.

Determination of S. aureus in wastewater

Presumptive counts of coagulase-positive staphylococci and *S. aureus* were determined after cultivation on Baird-Parker agar (Sigma-Aldrich, St. Louis, USA) according to EN ISO 6888-1 (2003) with 48 h incubation at 37 ±0.5 °C under aerobic conditions. The suspected colonies of coagulase-positive staphylococci and *S. aureus* were distinguished based on their typical appearance as it is mentioned in ISO 6888:1 (2003) and were further confirmed by tube coagulase test, microscopic examination, the presence of catalase using a 3 % solution of hydrogen peroxide and by the MALDI-TOF biotyper.

Production and use of BDD electrode for disinfection

The used BDD thin films were grown for 120 min (thickness of about 500 nm) in a HFCVD (Hot filament chemical vapor deposition) reactor on both sides of an Si (10 9 10 mm) substrate. Boron deposition was achieved by adding trimethylboron (TMB) into the 2 % CH_4 in H_2 gas mixture to obtain the B/C ratio of 10 000 ppm. The deposition pressure was 3 kPa and substrate temperature was 650 °C. Gases were activated by five tungsten filaments (0.7 mm diameter) heated up to 2100 °C. Surface of the BDD thin film was observed by SEM JEOL 7500F (Figure 1).

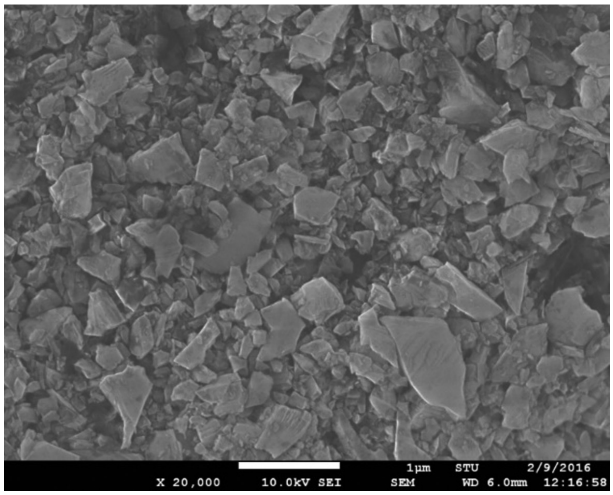

Fig. 1. SEM image of BDD electrode surface.

In Fig. 1, fine polycrystalline diamond surface with sub-micron crystal size can be seen. For testing purposes, a prototype electrode system was prepared consisting of 10 BDD thin film overgrown silicon substrates positioned in two rows by five as the anode (16 cm^2) and a graphite rod cathode (10 mm diameter) located above (10 cm^2) the anode. Stabilized DC power supply GPS 3005 (Goldsun Electronics Co., Ltd., Suzhou City, China) was used for anodic disinfection (Mackuľak et al., 2016). Boron-doped diamond electrode connected in three different ways was inserted into 300 ml sample of wastewater. In the first two cases, the BDD electrode was connected as the anode or cathode while the graphite electrode was used as the second electrode. In the third case, the BDD electrode served concurrently as anode and cathode. The distance between electrodes was 1 cm and DC power supply set to 30 V was used to create the potential difference. Wastewater disinfection time was 60 min while samples for treatment efficiency analysis were taken at 5 and 60 min. In case of BDD electrode connected as anode, the samples were taken after 2, 5, 10, 20, 40 and 60 min of disinfection. Temperature of the samples during the

disinfection was monitored as increased temperature was expected with this type of treatment.

Production and use of Fe (VI) for disinfection

Potassium ferrate was prepared as follows: electrolysis was performed in an oil thermostat with a calibrated sensor, stainless steel box and PTFE open crucible with the sample (KOH). Reference end of the thermocouple was immersed in a Dewar flask with ice water. Anode was composed of steel class 11 (Valsteel, Zubří, Czech Republic) comprising five interconnected rods with the diameter of 8.5 mm and length of 46 mm. The counter electrode was composed of the same material as the anode. The cathodic and the anodic compartments were divided by a diaphragm. Mass fraction of KOH was below 70 % (w/w). Based on the phase diagram, the temperature for this experiment was chosen to be 40 °C. The working anodic current density was optimized to be 20 mA/cm^2. The final concentration of the prepared potassium ferrate was approximately 80 % (w/w) (Czölderová et al., 2018).

Three different amounts of ferrates — 10, 50 and 100 mg (obtained from Palacký University in Olomouc, Czech Republic) were added into 300 ml of wastewater samples from influent and effluent of the WWTP. The solution was subsequently intensively mixed for one hour on a shaker at laboratory temperature. OH^- ions are released into wastewater during this method of disinfection and thus the pH change was monitored for the ferrates samples of 10 and 100 mg.

Results and discussion

Two possible types of wastewater disinfection methods: application of boron doped diamond electrode and addition of ferrates, were compared in this study. Efficiency of these methods in reducing the counts of coagulase-positive staphylococci and *S. aureus* was studied in influent and effluent wastewater of WWTP Petržalka, collecting 24 h wastewater samples on 9. 14. 2015 and 1. 14. 2016. A BDD electrode was used in three different connections, as anode or cathode with a counterpart carbon electrode and concurrently as anode and cathode. Ferrates powder was added in three different doses — 10, 50 and 100 mg, to 300 ml of wastewater samples.

The obtained results, summarized in Table 1 and Table 2, showed that the most effective application of the BDD electrode against coagulase-positive staphylococci and *S. aureus* in wastewater was obtained using the anodic connection as the inhibition up to 100 % (decrease about 2 log CFU/ml) was reached. These results correspond well with those of other studies where the anodic connection was marked as a method with the highest efficiency (Panizza and Cerisalo, 2009; Rajab et al., 2015). The highest efficiency of anodic connection can be explained by the production of hydroxide radicals $HO^{\bullet}$, which belong to the strongest oxidizing agents (Kraft, 2008; Michael-Kordatou et al., 2018). In case of cathodic connection, hydrogen peroxide (H_2O_2) is generated as the reactive agent (Kraft, 2008). However, as staphylococci are catalase-positive (Halpin-Dohnalek and Marth, 1989), they can degrade a certain amount of H_2O_2 to water and free oxygen by enzyme catalase. Therefore, the cathodic connection has lower efficiency compared to the anodic one. Surprisingly, the lowest inhibitory efficiency was observed using the BDD in simultaneous anode-cathode connection.

Tab. 1. Efficiency of coagulase-positive staphylococci and *S. aureus* inhibition in wastewater samples from 9. 14. 2015.

Disinfection method	Disinfection application	Inhibition efficiency [%] INFLUENT water		Inhibition efficiency [%] EFFLUENT water	
		coagulase-positive staphylococci	*S. aureus*	coagulase-positive staphylococci	*S. aureus*
BDD electrode Anode	5 min	83.0	96.8	56.5	100.0
	60 min	100.0	100.0	100.0	100.0
BDD electrode Cathode	5 min	74.8	94.8	21.7	42.9
	60 min	100.0	100.0	69.6	85.7
BDD electrode Anode+cathode	5 min	54.1	90.7	*	*
	60 min	96.1	92.3	30.4	85.7
Ferrates	10 mg	74.0	94.3	*	*
	50 mg	80.6	96.2	*	*
	100 mg	84.3	97.5	82.6	85.7

*increase in bacteria number

Tab. 2. Efficiency of coagulase-positive staphylococci and *S. aureus* inhibition in wastewater samples from 1. 14. 2016.

Disinfection method	Disinfection application	Inhibition efficiency [%] INFLUENT water		Inhibition efficiency [%] EFFLUENT water	
		coagulase-positive staphylococci	*S. aureus*	coagulase-positive staphylococci	*S. aureus*
BDD electrode Anode	5 min	73.2	93.8	17.8	50.0
	60 min	99.9	99.7	100.0	100.0
BDD electrode Cathode	5 min	74.3	93.6	16.8	75.0
	60 min	97.4	99.4	71.0	58.3
BDD electrode Anode+cathode	5 min	65.2	86.7	*	*
	60 min	81.2	92.9	16.8	33.3
Ferrates	10 mg	50.9	95.9	*	*
	50 mg	66.4	95.1	*	*
	100 mg	96.3	98.8	60.8	83.3

*increase in bacteria number

The addition of ferrates led to the inhibition of both coagulase-positive staphylococci and *S. aureus* in influent wastewater in all cases. Moreover, the higher the addition of ferrates, the more intensive staphylococci inhibition, ranging from 74 % to 97.5 % in the September sample and from 50.9 % to 98.8 % in the January sample.

On the other hand, the increase of coagulase-positive staphylococci including *S. aureus* counts in effluent samples was observed in case of 10 and 50 mg ferrates addition. The addition of 10 mg of ferrates led to an average increase of about 1.47 ±0.15 log CFU/ml of studied bacteria, while the addition of 50 mg of ferrates led to the average increase of about 0.61 ±0.21 log CFU/ml. Only the highest ferrates addition caused staphylococci inhibition of about 61–86 %.

It is important to remark that added ferrates do not react only with organic substances but also cause water decomposition (see Eq. 1), and the released OH^- increases wastewater pH (Fig. 2), mainly in case of addition of 100 mg of ferrates. The initial wastewater pH was 7.5 and after ferrates addition it increased to pH 9.27 and 9.55 in influent and effluent water, respectively. Such high pH values may show inhibition effect on staphylococci as they optimal growth is observed in the pH range of 6–7 (Halpin-Dohnalek and Marth, 1989).

$$4FeO_4^{2-} + 10H_2O \rightarrow 4Fe^{3+} + 10OH^- + 3O_2 \qquad (1)$$

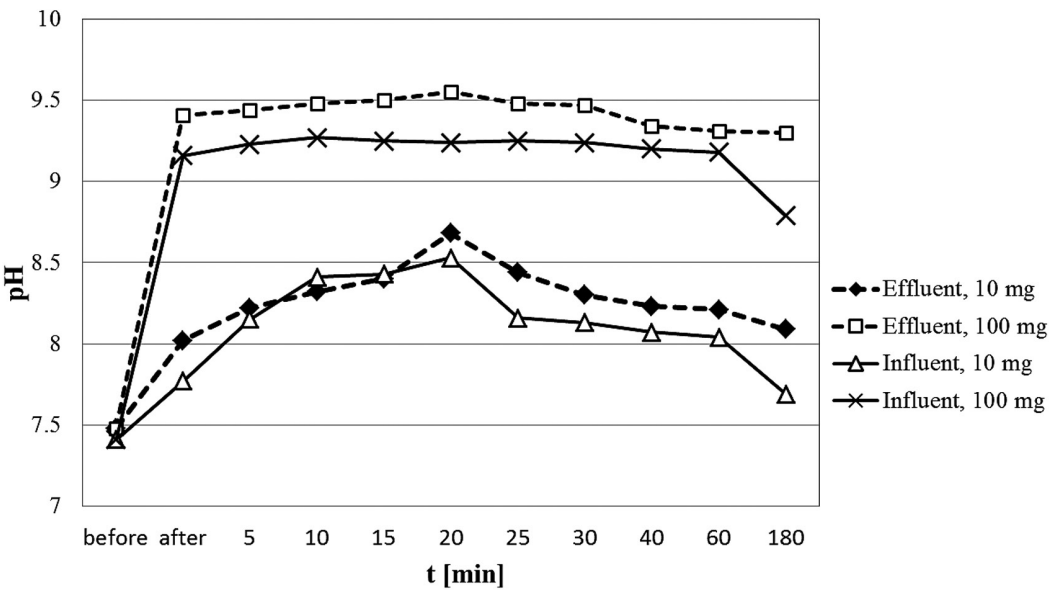

Fig. 2. Changes of pH after adding 10 and 100 mg of powdered ferrates into 300 ml of influent and effluent wastewater.

These results suggest the following question to be further investigated: Is the disinfecting effect of ferrates due to their oxidizing properties or the high pH of the sample?

Considering the obtained results it can be concluded that the most effective disinfection method against coagulase-positive staphylococci is the application of BDD electrode in anode connection. However, it is necessary to determine the WWTP stage where it is useful to place the electrodes. Therefore, disinfection efficiency was monitored in dependence on time as it is shown in Fig. 3. In influent wastewater, the coagulase-positive staphylococci were not eliminated even after 60 min of disinfection (their final count was 2.44 log CFU/ml). However, in effluent wastewater, complete inhibition of staphylococci was observed after 40 min. So, it can be stated that the rate of coagulase-positive staphylococci elimination in early minutes is significantly higher in influent than in effluent water. For example, after 10 min of disinfection, inhibition efficiency of 70.4 % was observed for staphylococci in influent but it was only 16.8 % in effluent wastewater, suggesting that the rate of disinfection depends on the concentration of bacteria in the sample as the initial staphylococci counts were 4.17 log CFU/ml and 1.03 log CFU/ml in influent and effluent wastewater, respectively.

Another important information for practical application of the BDD electrode is the energy consumption estimated using Eq. 2 (Rajab et al., 2015).

$$E\left(\frac{\text{kWh}}{\text{m}^3}\right) = \frac{UIT}{V_{vz}} \qquad (2)$$

where U is the electrical voltage (V), I the electrical current (A), T time (h) and V_{vz} is the sample volume (m^3). The initial concentration of coagulase-positive staphylococci in effluent wastewater sample was 1.03 log CFU/ml. Complete disinfection was reached after 40 min at 29.7 V and 60 mA, i.e. energy consumption was 3.96 kWh for complete disinfection of 1 m^3 of the effluent sample. Usual energy consumption in a WWTP is about 0.4 kWh/m^3; hence, the energy consumption of treatment using the BDD electrode is approximately ten times higher than that of the standard biological method.

Conclusions

Results of staphylococci inhibition by BDD electrode in three different connections showed that the anodic connection with a graphite electrode counterpart is the most effective one. Using this type of connection, the efficiency of coagulase-positive staphylococci and *S. aureus* elimination reached 100 % (decrease of about 2 log CFU/ml). Considering the disinfection process efficiency, the recommended location of the BDD electrode is the tertiary treatment in the WWTP. A disadvantage of this process is the relatively high energy consumption (3.96 kWh/m^3) required to complete coagulase-positive staphylococci elimination. The addition of ferrates as a disinfection method showed the addition of 100 mg of powdered ferrates to be the most efficient. Using lower doses of ferrates (10 and 50 mg) resulted in an increase of contaminants concentration. Further research on ferrates

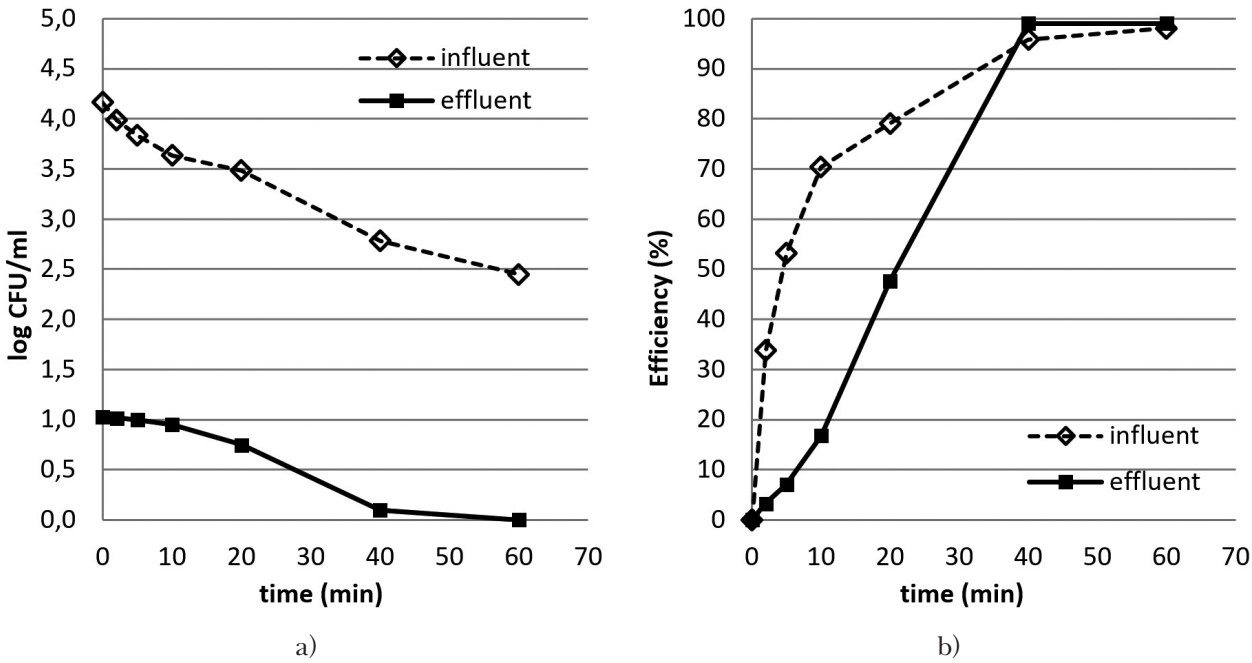

Fig. 3. Time dependence of disinfection efficiency against coagulase-positive staphylococci in influent and effluent wastewater using BDD electrode in anodic connection.

application is necessary because it is not clear whether the disinfecting effect of ferrates is due to their oxidizing properties or their ability to increase pH (up to 9.5). Further research on advanced oxidation processes is also needed for intensification of methods to remove micropollutants and resistant types of bacteria from wastewater because these substances can cause health problems.

Acknowledgement

This work was supported by the Slovak Research and Development Agency under the contract APVV-19-0250, APVV-16-0124, APVV-16-0171, APVV-17-0183. PP-COVID-20-0019 and project VIR-SCAN – Wastewater monitoring data as an early warning tool to alert COVID-19 in the population.

The publication was created as part of a grant scheme project to support young researchers „Domácnosti ako potenciálny zdroj mikrovlákien pre životné prostredie", v podmienkach STU v Bratislave, „Zdravotnícke zariadenia a hudobné festivaly ako bodové zdroje mikropolutantov v povrchových vodách a možnosti ich účinného odstraňovania", as well as within the project of a grant scheme to support excellent teams of young researchers in the conditions of STU in Bratislava „Monitoring a odstraňovanie fragmentov RNA vírusu SARS-CoV-2 v odpadových vodách pomocou železanov",

References

Baird MR, Lee WH (1995) Int J Food Microbiol 26: 15–24.

Birošová L, Mackuľak T, Bodík I, Ryba J, Škubák J, Grabic R (2014) Sci Total Environ 490: 440–444.

Brodin T, Fick J, Jonsson M, Klaminder J (2013) Science 339: 814–815.

Czölderová M, Behúl M, Filip J, Zajíček P, Grabic R, Vojs-Staňová A, Gál M, Kerekeš K, Híveš J, Ryba J, Rybanská M, Brandeburová P, Mackuľak T (2018) Chem Eng J 349: 269–275.

ECDC (2017) Antimicrobial resistance surveillance in Europe 2015, Surveillance report, Available in May 2017: http://ecdc.europa.eu/en/publications/Publications/antimicrobial-resistance-europe-2015.

EN ISO 6888-1 (2003) Microbiology of food and animal feeding stuffs – Horizontal method for the enumeration of coagulase-positive staphylococci (Staphylococcus aureus and other species) – Part 1: Technique using Baird-Parker agar medium, 1–11.

Golovko O, Kumar V, Fedorova G, Randák T, Grabic R (2014) Environ. Sci Pollut Res 21: 7578–7585.

Halpin-Dohnalek MI, Marth EH (1989) J Food Prot 52: 267–282.

Iakovides IC, Michael-Kordatou I, Moreira NFF, Ribeiro AR, Fernandes T, Pereira MFR, Nunes OC, Manaia CM, Silva AMT, Fatta-Kassinos D (2019) Wat Res 159: 333–347.

Kajitvichyanukul P, Suntronvipart N (2006) J Hazard Mater 2: 384–391.

Kraft A (2008) Platinum Met Rev 52: 177–185.

Kulandaivelu J, Gao J, Song Y, Shrestha S, Li X, Li J , Doederer K, Keller J, Yuan Z, Mueller JF, Jiang G (2019) Environ Sci Technol 53: 6245–6254.

Kümmerer K (2009) Chemosphere 75: 435–441.

Li Y, Zhu G, Ng JW, Tan KS (2014) Sci Total Environ 468: 908–932.

Mackuľak T, Mosný M, Grabic R, Golovko O, Koba O, Birošová L (2015a) Environ Toxicol Pharmacol 39: 483–488.

Mackuľak T, Mosný M, Škubák J, Grabic R, Birošová L (2015b) Environ Toxicol Pharmacol 39: 969–973.

Mackuľak T, Vojs M, Grabic R, Golovko O, Vojs Staňová A, Birošová L, Medveďová A, Híveš J, Gál M, Kromka A, Hanusova A (2016) Monatsh Chem 147: 97–103.

Michael-Kordatou I, Karaolia P, Fatta-Kassinos D (2018) Water Res 129: 208–230.

Mylotte JM, McDemott C, Spooner JA (1987) Reviews of Infectious Diseases 9: 891–907.

Novo A, André S, Viana P, Nunes OC, Manaia CM (2013) Water Res 47: 1875–1887.

Nuel M, Laurent J, Bois P, Heintz D, Wanko A (2018) Sci Total Environ 615: 1099–1109.

Panizza M, Cerisola G (2009) Chem Rev 109: 6541–6569.

Rajab M, Heim C, Letyel T, Drewes JE, Helmreich B (2015) Chemosphere 121: 47–53.

Stepanović S, Ćirković I, Djukić S, Vuković D, Švabić-Vlahović M (2008) Letters in Applied Microbiology 47: 339–341.

Verlicchi P, Zambello E (2015) Sci Total Environ 538: 750–757.

Wilkinson LJ, Hooda SP, Swinden J, Barker J, Barton S (2018) Environ Pollut 234: 864–875.

Yuan S, Jiang X, Xia X, Zhang H, Zheng S (2013) Chemosphere 90: 2520–2525.

sciendo

Decrease of cholesterol content in milk by sorption onto β-cyclodextrin crosslinked with tartaric acid; considerations and implications

Martin Kukula, Lukáš Kolarič, Peter Šimko

Slovak University of Technology in Bratislava,
Faculty of Chemical and Food Technology, Institute of Food Science and Nutrition,
Radlinského 9, 812 37 Bratislava, Slovak Republic
qsimko@stuba.sk

Abstract: Elevated cholesterol intake can induce the development of cardiovascular diseases in man, especially with long term animal origin foods consumption. Therefore, this work deals with the possibility of cholesterol content decrease in milk applying β-cyclodextrin crosslinked with tartaric acid (βCDcTA) as a removal agent. Evaluation of statistic data on food consumption in the Slovak Republic in 2018 aimed at total cholesterol daily intake and effects of "milky" cholesterol content decrease on total cholesterol balance. During the experiments, various amounts of βCDcTA addition to milk were studied resulting in optimal 5 % addition resulting in the cholesterol content decrease by 85.4 % in comparison to original cholesterol content. For monitoring purposes, an HPLC method analysing cholesterol content in saponified milk was employed. The food consumption data analysis showed that total per capita daily cholesterol intake was 369.8 mg, from which 86 mg was assigned to the cholesterol contained in milk and dairy products while the application of cholesterol removal procedure could decrease the total per capita daily cholesterol intake to 296.3 mg ("milky" cholesterol amount equal to 12.6 mg), which in below the recommended value of 300 mg daily intake still valid in the Slovak Republic. This approach might prove as a meaningful step to weaken health problems associated with high long term intake of cholesterol contained in foods of animal origin.

Keywords: cholesterol intake, milk, HPLC, health, crosslinked β-cyclodextrin, cholesterol-free foods, annual consumption

Introduction

Cholesterol is a soft, waxy compound found among the lipids or fats in the bloodstream and in all cell membranes. It is a non-saponifiable lipid, essential in maintaining vital functions of organisms, as it participates in the formation of cell membranes, several hormones, vitamin D, and bile acids needed for food fat digestion (Parish et al., 2002). On the other hand, elevated intake of cholesterol contained in foods of animal origin could result in serious cardiovascular diseases (CVD) such as arteriosclerosis and stroke. Larsson et al. (2012) analysed data such as education, weight, height, cigarette smoking, physical activity, family history of myocardial infarction, aspirin use, alcohol consumption, and diet of 34,670 women and stated that dietary cholesterol can be positively associated with the risk of total stroke and cerebral infarction. On the base of such information and real CVD situation in Slovak population, cholesterol daily intake recommended value has been set to 300 mg/adult person in the Slovak Republic by health authorities (Official Report of the Ministry of Health of the Slovak Republic, 2015). To the contrary, contemporary guidelines for CVD risk reduction from the American Heart Association and American College of Cardiology as well as "2015–2020 Dietary Guidelines for Americans" have already not issued explicit guidance for dietary cholesterol intake due to inconsistencies in the evidence base and the inherent difficulty in conducting and interpreting studies to isolate the independent effect of dietary cholesterol on CVD (Carson et al., 2020). Similarly, according to the recent European Society of Cardiology and European Atherosclerosis Society guidelines for the management of dyslipidaemias, the key initiating event in the atherogenesis is the retention of low-density lipoprotein cholesterol (LDL-C) and other cholesterol-rich apolipoprotein containing lipoproteins within the arterial wall (Mach et al., 2020). Indeed, evidence has confirmed that retention of LDL-C and other cholesterol-rich apolipoprotein containing lipoproteins within the arterial wall is the key initiating event in atherogenesis (Ference e al., 2017). One way or another, limitation of cholesterol content in foods could be one of the key issues targeting health problems associated with elevated blood cholesterol content. One of effective procedures limiting the blood cholesterol content is focusing on health dietary patterns such as the Mediterranean-style diet (Fung et al., 2005), or Dietary Approaches to Stop Hypertension (DASH) (Appel et al., 1997) which are inherently associated

with lowered blood cholesterol content due to daily intake of <300 mg of cholesterol (Carson et al., 2020). Another approach to lowering cholesterol content in diet can be based on technological processes during raw materials` treatments resulting in minimised cholesterol content in comparison with the original matrix. Alonso et al. (2009) demonstrated that beta cyclodextrin (β-CD) addition of 0.4 %, 0.6 %, 0.8 % or 1.0 % removes cholesterol from milk in the range between 65.4 % and 95.3 %, when maximum cholesterol removal was seen within 6 h of treatment with β-CD-cholesterol complex removal by centrifugation. Han et al. (2005) removed cholesterol in homogenised milk with β-cyclodextrin crosslinked with adipic acid and in this case, cholesterol removal of above 90 % was observed. Also, Lee et al. (2012) studied the use of crosslinking β-CD for cholesterol removal in milk and cream and concluded that cross-linked β-CD with 15 % adipic acid showed better β-CD recovery and reuse, and higher cholesterol removal rate at repeated recycle than cross-linked β-CD with 2 % adipic acid. Methods for cholesterol content determination in food can be divided into three major categories: classical chemical methods based on the Abell-Kendall protocol, fluorometric and colorimetric enzymatic assays, and analytical instrumental approaches such as gas and liquid chromatography (Li et al., 2019). The most appropriate and frequently applied sample treatment before HPLC include direct saponification followed by the extraction of unsaponifiable residue into a non-polar solvent. Direct saponification is preferred due to simple conversion of non-polar fatty acid esters to polar products with the following effective removal by multiple extraction with n-hexane (Bauer et al., 2014; Albuquerque et al., 2016; Kolarič and Šimko, 2020a). Alternatively, a mixture of polar and non-polar solvents has been proposed to provide more efficient cholesterol extraction from various food matrix where cholesterol is usually bound by many other biological compounds such as lipoproteins, proteins, and phospholipids (Dinh et al., 2011). The first aim of this work was thus to study conditions of cholesterol removal from milk by application of β-CD crosslinked with tartaric acid (βCDcTA) while the second aim was to consider total cholesterol daily intake per capita, its removal from milk and dairy products and effect of the removal on total cholesterol balance in Slovak population.

Materials and methods

Sample

Cow milk (3.5 % fat, Rajo a.s., Bratislava, Slovakia) was bought in a local market.

Chemicals

All solvents and chemicals were of analytical grade. Cholesterol standard was from Sigma-Aldrich with the purity of ≥99 %. Chloroform, n-hexane, ethanol, and sodium sulphate anhydrous were purchased from Centralchem s.r.o. (Bratislava, Slovakia). Methanol and acetonitrile (HPLC grade) were purchased from Fisher Chemical (Loughborough, UK). Tartaric acid was provided by Lachema Brno (Czech Republic).

Sample preparation

The amount of 0.5 g of milk was refluxed with 15 mL of 1 mol/L methanolic solution of KOH for 15 min. Then, cooled matter was extracted twice with a mixture of n-hexane and chloroform (1:1, v/v) to obtain 15 mL of total extract. To increase the polarity of saponifiable residue, 10 mL of deionised water was added. To avoid the formation of emulsion during the extraction, 1 mL of ethanol (96 %) was added to the saponified matter. Then, the extract was filtrated through anhydrous Na_2SO_4, and evaporated using a rotary vacuum evaporator (Heidolph, Germany) until dryness; the residue was dissolved in 5 mL of methanol, filtered using a syringe PTFE filter with a 0.2 µm membrane (Agilent Technologies, Santa Clara, CA, USA), and analysed by HPLC.

HPLC conditions

HPLC was performed using an Agilent Technologies 1260 infinity system (Agilent, Santa Clara, CA, USA) equipped with a vacuum degasser, quarterly pump, autosampler, and a UV-DAD detector operating at 205 nm. Isocratic elution was performed at the flow rate of 0.5 mL/min mobile phase composed of acetonitrile/methanol 60:40 (v/v). The injection volume was 10 µL and the temperature was set at 30 °C. Zorbax Eclipse Plus C18 column (2.1 × 50 mm, 3.5 µm particle size, Agilent, Santa Clara, CA, USA) was used as stationary phase with the guard column Zorbax SB-C18 (4.6 × 12.5 mm, 5 µm particle size, Agilent, Santa Clara, CA, USA). At these conditions, cholesterol was eluted in 2.2 min. Data were recorded and treated using the OpenLab CDS software, ChemStation Edition for LC, and LC/MS systems (product version A.01.08.108).

Preparation of crosslinked βCDcTA

βCDcTA was prepared according to Han et al. (2005) as follows: 10 g of β-CD were mixed with 8 mL of distilled water and the suspension was magnetically stirred at room temperature for 2 hrs. Then, 0.2 g of tartaric acid was added, pH was adjusted to pH = 10 with 1 mol/L NaOH and the

reaction mixture was stirred for 1.5 hrs; the product was then readjusted to pH = 5 with acetic acid. Finally, βCDcTA was recovered by filtering through Whatman paper No. 2, washed three times with 15 mL of distilled water, dried at 60 °C for 20 hrs and passed through a 100 mesh sieve.

Cholesterol removal

Each sample of 10 g of milk was placed in a beaker and different amounts of βCDcTA (1.0, 2.0 or 5.0 %) were added. The mixtures were stirred at 150 rpm using a magnetic blender (MM1, Laboratorní přístroje Praha, Czech Republic) for 15 min at 23 °C and centrifuged at 166 g (5430 R Eppendorf, Hamburg, Germany) for 10 min. After centrifugation, the milk supernatant was analysed for cholesterol content. All procedures were duplicated.

Acquisition of statistical data

Statistical data on annual food consumption in the Slovak Republic were obtained from the latest annual report – Food Consumption in the Slovak Republic in 2018 (Sitárová, 2019).

Results and Discussion

Determination of cholesterol content

For the determination of cholesterol content in milk, an in-house validated HPLC method was applied (Kolarič and Šimko, 2020b). At the given conditions, chromatographic separation of cholesterol was sufficient which was confirmed by UV spectra of the cholesterol standard and cholesterol in milk. As follows from Figure 1, the spectra are practically identical with the peak ratio parameter approaching 1.

For illustration, chromatographic record of cholesterol standard analysis and milk analysis are shown in Figures 2 and 3.

Cholesterol removal degree

Efficiency of cholesterol removal in dependence on βCDcTA addition is shown in Table 1.

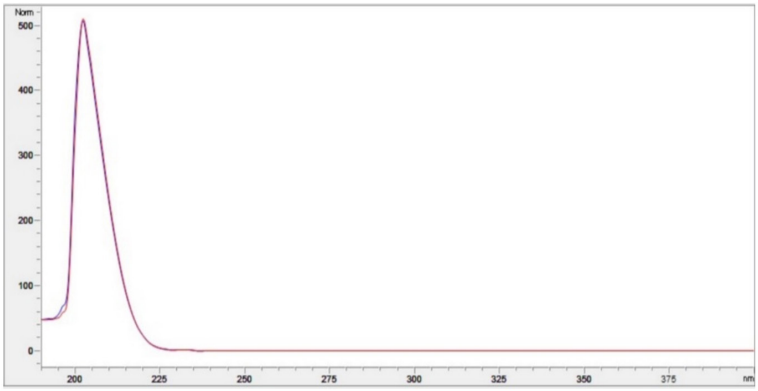

Fig. 1. Comparison of UV spectra of cholesterol standard (red line) and cholesterol in milk (blue line).

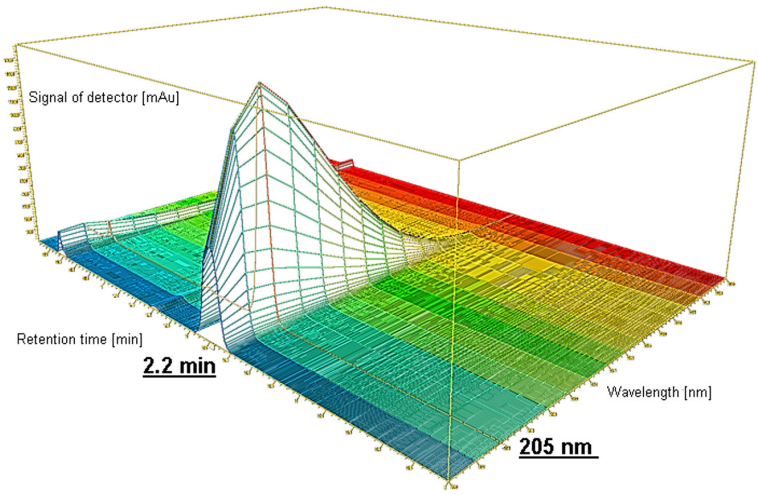

Fig. 2. 3D HPLC record of cholesterol standard analysis.

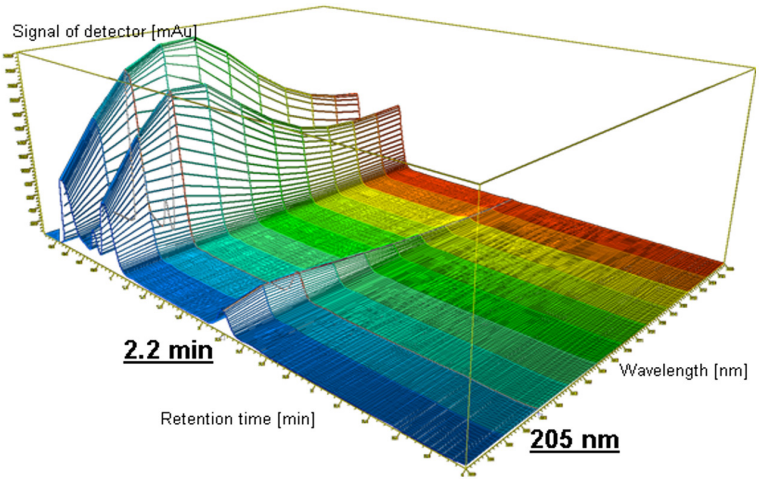

Fig. 3. 3D HPLC record of cholesterol in milk analysis.

Tab. 1. Removal of cholesterol from milk by βCDcTA addition.

βCDcTA addition [%]	Signal [mAU.s]	Cholesterol content [mg/kg]	RSD [%]	Cholesterol removal degree [%]
0	660.02 ±59.60	92.78 ±9.57	10.3	–
1	405.53 ±64.86	31.23 ±4.92	15.8	66.3
2	209.63 ±18.89	15.58 ±1.39	8.9	83.2
5	175.90 ±20.50	13.57 ±1.57	11.6	85.4

Tab. 2. Per capita food consumption in the Slovak Republic in 2018, consumption by commodity and calculated original and reduced cholesterol content.

A	B	C	D	E	F	G
Commodity	Consumption per capita* [kg]	Cholesterol content** [mg/kg]	Cholesterol daily intake by commodity [mg]	Cholesterol daily intake by commodity [%]	Reduced cholesterol daily intake [mg]	Reduced cholesterol daily intake by commodity [%]
Milk (including dairy products without butter)	171.1	130.0	60.9	16.5	8.9	3
Butter	3.4	2 690.0	25.1	6.8	3.7	1.2
Lard	3.3	950.0	8.6	2.3	8.6	2.9
Pork meat	35.4	690.0	66.9	18.1	66.9	22.6
Beef meat	5.2	720.0	10.3	2.8	10.3	3.5
Poultry meat	22.2	730.0	44.4	12.0	44.4	15.0
Fish	5.5	630.0	9.5	2.6	9.5	3.2
Eggs	13.7	3 840.0	144.1	39.0	144.1	48.6
Sum			369.8	100.0	296.3	100.0

*data taken from Sitárová, 2019.
**data taken from Frida, 2020.

As it follows from the measured data, intensity of cholesterol removal depends on the amount of βCDcTA added to treated milk. Thus, while at the 1 % addition of βCDcTA, the cholesterol content decreased by 66.3 %, at the 5 % addition, it decreased by 85.4 %. These results are a little worse in comparison with data published by Han et al. (2005) who were able to decrease cholesterol con-

tent in the range of 92.1 to 93.1 %. On the other hand, cholesterol decrease achieved by Kim et al. (2004) was in the range of 79.4 to 83.3 % when applying β-CD crosslinked with epichlorohydrin.

Evaluation of statistical data

Primary data on to average food consumption in 2018 were obtained from Sitárová (2019). As follows from Table 2 column A, these statistical data show per capita consumption of milk (as milk itself and dairy products) and butter, what is critical for the evaluation of "milky" cholesterol data. However, also other food commodities participate on total cholesterol intake. To estimate the total per capita daily cholesterol intake in Slovak population, data on cholesterol content in individual food commodities were taken from the Danish food database Frida (2020). Cholesterol content in individual commodities is shown in column C while daily per capita cholesterol intake in mg and % are displayed in columns D and E. As it can be seen from these data, per capita daily cholesterol intake in 2018 reached the value of 369.8 mg, which is really high as this includes total Slovak population including suckling infants, vegetarians or even vegans. Therefore, it is reasonable to assume that daily cholesterol intake in some social groups exceeds the recommended value of 300 mg by twice, which is seriously threating health, or even life considering long duration of this situation. Hence, decreasing cholesterol content in milk and its products by 85.4 %, enables decreasing the per capita daily cholesterol intake from 369.8 mg to 296.3 mg (column F), which is below the recommended value and the portion of cholesterol intake from milk and dairy products would decrease from 23.3 % to 4.2 % (column G) in total cholesterol balance. For comparison, mean cholesterol intake of the overall US population had been relatively constant at ~290 mg/day in 2001–2014 (Xu et al. 2018). So, by removal of cholesterol from milk and dairy products, health effects of dairy products can be considerably strengthened while the consumption of full-fat dairy products contributes to higher intakes of significant nutrients such as calcium, vitamins D and K and other bioactive compounds (Loran et al., 2018).

Conclusion

Summarising the results, information, data, and findings obtained in this study, the following conclusions can be postulated:

a) Cholesterol content in milk (and dairy products produced from milk) can be effectively decreased by βCDcTA addition
b) The addition of 5 % of βCDcTA results in cholesterol content decrease by 85.4 % in treated milk
c) Application of such treated milk in food production can decrease the total cholesterol average daily intake per capita in Slovak population from the current value of 369.8 mg to 296.3 mg, weakening health problems associated with long duration of high intake of cholesterol contained in foods of animal origin.

Conflict of interest

Authors declare no conflict of interest. The funders had no role in the design of the study, collection and interpretation of data, writing of the manuscript, or in the decision to publish the results.

Acknowledgements

This publication was supported by the Operational Program Integrated Infrastructure within the project: Demand-driven research for the sustainable and innovative food, Drive4SIFood 313011V336, co-financed by the European Regional Development Fund, and co-funded by project "ACCORD" (ITMS project code: 313021X329) supported by the Operational Programme Research and Development funded by the European Regional Development Fund and the grant APVV-061-2018.

References

Albuquerque TG, Oliveira MBPP, Sanches-Silva A, Costa HS (2016) Food Chemistry 193: 18–25.

Alonso L, Cuesta P, Fontecha J, Juarez M, Gilliland SE (2009) Journal of Dairy Science 92: 863–869.

Appel LJ, Moore TJ, Obarzanek E, Vollmer WM, Svetkey LP, Sacks FM, Bray GA, Vogt TM, Cutler JA, Windhauser MM et al. (1997) New England Journal of Medicine 336: 1117–1124.

Bauer LC, Santana DA, Macedo MS, Torres AG, de Souza NE, Simionato JI (2014) Journal of the Brazilian Chemical Society 25: 161–168.

Carson JAS, Lichtenstein AH, Anderson CA, Appel LJ, Kris-Etherton PM, Meyer KA, Polonsky T, Van Horn L (2020) Circulation 141: 39–53.

Danish food database Frida (2020) Available online: https://frida.fooddata.dk/ (accessed on 3. October 2020).

Dinh TTN, Thompson LD, Galyean ML, Brooks JC, Patterson KY, Boylan LM (2011) Comprehensive Reviews in Food Science and Food Safety 10: 269–289.

Ference BA, Ginsberg HN, Graham I, Ray KK, Packard CJ et al. (2017) European Heart Journal 38: 2459–2472.

Fung TT, McCullough ML, Newby PK, Manson JE, Meigs JB, Rifai N, Willett WC, Hu FB (2005) American Journal of Clinical Nutrition 82:163–173.

Han EM, Kim SH, Ahn J, Kwak HS (2005) Asian-Australasian Journal of Animal Sciences 18: 1794–1799.

Kim SH, Ahn J, Kwak HS (2004) Archives of Pharmacal Research 27: 1183–1187.

Kolarič L, Šimko P (2020a) Potravinárstvo Slovak Journal of Food Sciences 14: 118–124.

Kolarič L, Šimko P (2020b) Foods 9: 1378.
Larsson SC, Virtamo J, Wolk A (2012) Atherosclerosis 221: 282—286.
Lordan R, Tsoupras A, Mitra B, Zabetakis I (2018) Foods, 7, 29—34.
Li LH, Dutkiewicz EP, Huang YC, Zhou HB, Hsu CC (2019) Journal of Food and Drug Analysis 27: 375—386.
Official Report of Ministry of Health of Slovak Republic (2015) 63: 22-27. Available online: https://www.uvzsr.sk/docs/info/hv/Recommended_Nutrition_Doses_for_Population_of_the_Slovak_Republic.pdf; https://www.uvzsr.sk/index.php?option=com_content&view=article&id=1014:odporuane-vyivove-davky-pre-obyvatestvo-vnslovenskej-republike&catid=66:vyiva-a-bezpenos-potravin&Itemid=72
(accessed on 30. September 2020).
Mach F, Baigent C, Catapano AL, Koskinas KC, Casula M, Badimon L et al. (2020) European Heart Journal 41: 111—188.
Parish EJ, Boos TL, Shengrong L (2002) The chemistry of waxes and sterols. In: Akoh CC, Min DB (Eds) Food Lipids, pp. 103—131. Marcel Dekker, New York.
Sitárová T (2019) Food Consumption in the SR in 2018, pp. 10—17. Statistical Office of the Slovak Republic, Bratislava.
Xu Z, McClure ST, Appel LJ (2018) Nutrients 10: E771.